

X-ray Fluorescence (XRF) and Particle-Induced X-ray Emission (PIXE)

1.1 Introduction

X-ray Fluorescence (XRF) and Particle-Induced X-ray Emission (PIXE) are the two well-established nondestructive analytical techniques of X-ray emission spectroscopy. These techniques are powerful tools for rapid multielement nondestructive analyses and enable simultaneous detection of many elements in a solid or liquid with high-detection sensitivities, even in those cases where only small sample amounts are available. The fluoresced X-rays from the sample are collected and displayed with either energy dispersive or wavelength dispersive detector systems. The elements are identified by the wavelengths (qualitative) of the emitted X-rays while the concentrations of the elements present in the sample are determined by the intensity of those X-rays (quantitative). XRF and PIXE have emerged as efficient and powerful analytical tools for major, minor, and trace elemental analysis in a variety of fields like biology, environment, medicine, archaeology, and forensic science. These techniques can be used for analyzing rocks, metals, ceramics, and other materials. Handling of samples is greatly simplified by the open-air nature of the instrument used for XRF studies. However, operation outside a vacuum chamber has the disadvantage of decreased sensitivity to light elements.

XRF and PIXE techniques are similar in their fundamental approach and are based on the common fact that when an electron is ejected from an inner shell of an atom, an electron from a higher shell drops into this lower shell to fill the hole left behind. This results in the emission of an X-ray photon equal in energy to the energy difference between the two shells. However, the difference between the two techniques is the mechanism by which the inner-shell electron is emitted. The major difference between XRF and PIXE lies in the mode of excitation. In the XRF technique, high-energy X-ray photons are directed at the sample and this ejects the inner shell electrons while in the PIXE technique, the inner-shell electrons are ejected when protons or other charged particles, like He-ions, are made to impinge on the sample. The first Born approximation predicts in general that the excitation produced by different

charged particles should depend only on their charge and velocity, provided that the velocity is large compared to that of the electrons of interest in the target atom. If the velocity is high enough, not only should electrons and protons produce the same excitation but it is also the same as that produced by photons. The other differences between XRF and PIXE, such as excitation characteristics (mechanism of inner-shell excitation, effect of heavier projectiles/charge state effect, production of nondiagram lines, etc.), background distribution, analytical volume, lower limits of detection, and types of samples analyzed are also of importance and will also be discussed in this chapter.

The field of XRF is not only active at the international level but the IAEA is interested to extend the applicability range of the XRF technique, is apparent from the latest research paper by Markowicz et al. (2006) who have elaborated the specific philosophy behind the functioning of the IAEA XRF Laboratory at Seibersdorf Austria and its role in the XRF community including the methodological development and construction of XRF instruments in order to extend the applicability range of the XRF technique, particularly in support of applications of the analytical technique in developing IAEA member states.

1.2 Principle of XRF and PIXE Techniques

The principle of both of these techniques is to excite the atoms of the substance to be analyzed by bombarding the sample with sufficiently energetic X-rays/ γ -rays or charged particles. The ionization (photoionization for XRF and ionization caused due to Coulomb-interaction in case of PIXE) of inner-shell electrons is produced by the photons and charged particles, respectively. When this interaction removes an electron from a specimen's atom, frequently an electron from an outer shell (or orbital) occupies the vacancy. The distribution of electrons in the ionized atom is then out of equilibrium and within an extremely short time ($\sim 10^{-15}$ s) returns to the normal state, by transitions of electrons from outer to inner shells. When an outer-shell electron occupies a vacancy, it must lose a specific amount of energy to occupy the closer shell of more binding energy. This amount is readily predicted by the laws of Quantum Mechanics and usually much of the energy is emitted in the form of X-rays. Each of such electron transfer, for example from the L-shell to the K-shell, represents a loss in the potential energy of the atom. When released as an X-ray photon, the process is X-ray emission. This energy appears as a photon (in this case a $K\alpha$ photon) whose energy is the difference between the binding energies of the filled outer shell and the vacant inner-shell. In the normal process of emission, an inner-shell electron is ejected producing the photoelectron. Similarly, in the ion-atom collisions one or more of the atomic electrons can get free (single or multiple ionization), one or several electrons can be transferred from one collision partner to the other, one or both of the collision partners can become excited, and a combination of these

elementary processes can also take place. The excess energy is taken away by either photons (characteristic X-rays) – when an electron from a higher level falls into the inner-shell vacancy or Auger (higher-shell) electrons – when the energy released during the process of hole being filled by the outer shell electron, is transferred to another higher-shell electron. These emissions have characteristic energies determined fundamentally by the binding energy of the levels. The fraction of radiative (X-ray) decays is called the fluorescence yield, and is high for deep inner-shells. The de-excitation process leading to the emission of characteristic X-rays and Auger electrons is shown in Fig. 1.1. The Auger effect is most common with low-Z elements.

We have seen earlier that an electron from the K shell (or higher shell, if the energy of the impinging radiation (X-rays/ γ -rays) or charged particles is less than the binding energy of the K-shell) is ejected from the atom creating a vacancy in that shell as the projectile pass through the target atom. This vacancy is filled by an electron from the L or M shell. In the process, it emits a characteristic K X-ray unique to this element and in turn, produces a vacancy in the L or M shell. For instance, when exciting the K-shell ($1s_{1/2}$), the hole can be filled from $L_{III}(2p_{3/2})$ or $L_{II}(2p_{1/2})$ subshells, leading to $K\alpha_1$

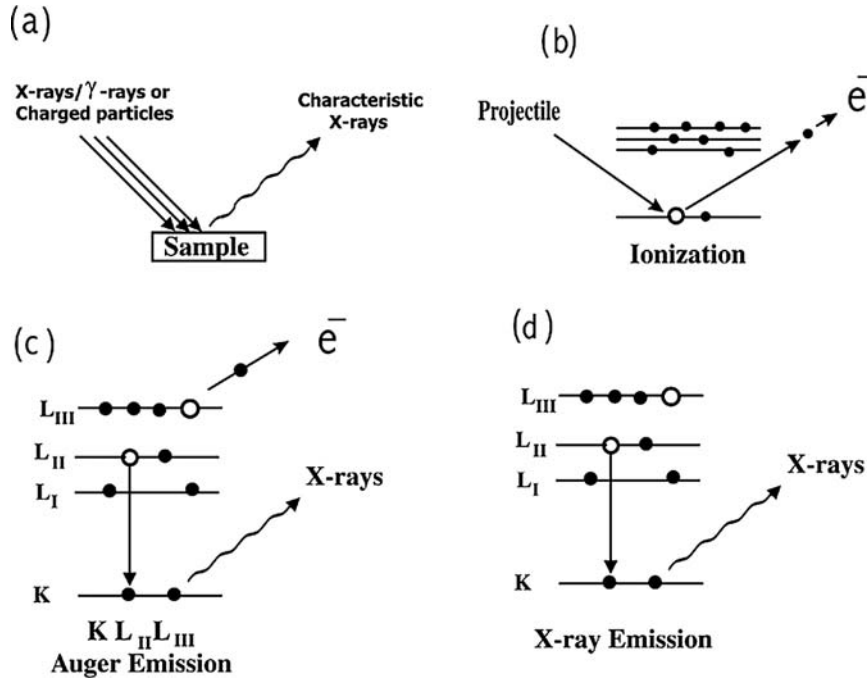


Fig. 1.1. (a) Schematic of the phenomenon of X-ray emission (b) Vacancy creation in the inner shell by X-rays or charged particles (c) process of Auger electron emission comprising of de-excitation and emission of higher-shell electron (d) process of X-ray emission

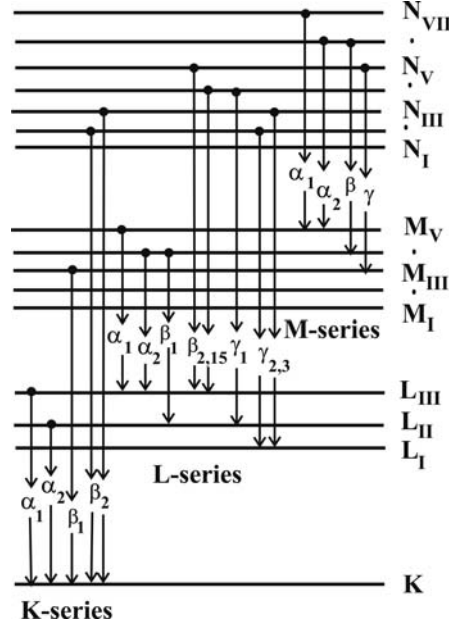


Fig. 1.2. Energy level diagram showing the origin of some of the K, L, and M X-rays

Table 1.1. Designation of various K and L X-ray transitions to denote transitions of electrons

K X-ray Lines	L X-ray Lines	
$K\alpha_1$ (K-L _{III})	$L\gamma_1$ (L _{II} -N _{IV})	$L\gamma_1$ (L _{II} -N _{IV})
$K\alpha_2$ (K-L _{II})	$L\gamma_2$ (L _I -N _{II})	$L\gamma_2$ (L _I -N _{II})
$K\beta_1$ (K-M _{III})	$L\gamma_3$ (L _I -N _{III})	$L\gamma_3$ (L _I -N _{III})
$K\beta_2$ (K-N _{II,III})	$L\gamma_4$ (L _I -O _{III})	$L\gamma_4$ (L _I -O _{III})
$K\beta_3$ (K-M _{II})	$L\gamma_6$ (L _{II} -O _{IV})	$L\gamma_6$ (L _{II} -O _{IV})

and $K\alpha_2$ lines. Electrons cannot come from the L_1 (i.e. $2s_{1/2}$) sub-shell, because a change in angular momentum is required in the quantum transition. The next shell with electrons is the valence band ($n = 3$) that gives rise to the widely separated and weak $K\beta$ lines. The energy level diagram showing the origin of some of the K, L, and M X-rays is presented in Fig. 1.2.

X-Ray Notation (Siegbahn)

The designation of various K and L X-ray transitions to denote transitions of electrons is given in Table 1.1.

As mentioned earlier, the spectroscopic notation for X-rays will be as:

$$\begin{aligned} L\alpha_1 &\rightarrow 2p_{3/2} - 3d_{5/2} \\ L\beta_1 &\rightarrow 2p_{1/2} - 3d_{3/2} \end{aligned}$$

because the spectroscopic notation for L_I , L_{II} , L_{III} , subshells are $2s_{1/2}$, $2p_{1/2}$, $2p_{3/2}$, respectively, and those for M_I , M_{II} , M_{III} , M_{IV} , and M_V are $3s_{1/2}$, $3p_{1/2}$, $3p_{3/2}$, $3d_{3/2}$, and $3d_{5/2}$, respectively, as explained in Sect. 1.3.

Apart from the characteristic X-ray lines called the diagram lines, non-diagram lines (satellite, hypersatellite and RAE) also appear in the complex K X-ray spectrum. The X-ray lines arising out of the multiply ionized atoms are termed K satellite (KL^n) and K-hypersatellite lines (K^2L^n), where K^mL^n denotes the vacancy from the de-excitation of the double K vacancies and were observed in ion-atom collisions for the first time by Richard et al. (1972). The K satellite lines arise from the group of lines corresponding to the transitions from initial states having one hole in the K-shell and n -holes in the L-shell i.e., $(1s)^{-1}(2p)^{-n} \rightarrow (2p)^{-n-1}$ and represented by $K\alpha L^n$. On the other hand, the hypersatellite X-ray will be due to the $(1s)^{-2} \rightarrow (1s)^{-1}(2p)^{-1}$. The double K vacancies are usually filled by the independent transitions of two electrons accompanied by the emission of two photons or Auger electrons. The $K\alpha$ satellite lines will be represented as $K\alpha(2p)^5$, $K\alpha(2p)^4$, $K\alpha(2p)^3$, ... meaning that 5, 4, 3, ... electrons remain intact in the 2p shell while $K\alpha(2p)^6$ will represent the $K\alpha$ principle line with all the six 2p electrons intact. Similar terminology is also used for $K\beta$ satellite lines. Another category in which electron and photon are simultaneously emitted (known as the Radiative Auger effect RAE lines), comprises of single-photon two electron rearrangement transitions (Verma 2000). In the RAE process, the decay of a K-shell vacancy proceeds as a normal K Auger process except that there is emission of a photon along with an electron in addition to an electron filling the K-shell vacancy. Instead of the initial hole being filled with emission of either a full energy $K\alpha$ photon or a full energy Auger electron, there is simultaneous emission of a lower-energy photon $h\nu$ and excitation of an L-shell/M-shell electron, i.e., $h\nu + E_{\text{kin}}(Y_j) = E(KY_iY_j)$, where Y denotes an L- or M-shell and i and j denote the concerned subshells. Thus $E_{\text{kin}}(Y_j)$ is the kinetic energy of the ejected L_j/M_j -electron and $E(KY_iY_j)$ is the full Auger electron energy. The RAE process competes with the characteristic $K\alpha$ or $K\beta$ X-ray emission processes and produces a broad structure in the X-ray spectra, with energy less than $K\alpha_{1,2}/K\beta_{1,3}$ diagram line.

If the de-excitation takes place during the collision i.e., while the projectile and target electron clouds overlap, “noncharacteristic” molecular orbital (MO) X-ray can be emitted. However, the “characteristic” or separated atom X-rays will be seen if the vacancy de-excites after the collision.

1.3 Theory and Concept

According to the quantum theory, every electron in a given atom moves on in an orbital that is characterized by four quantum numbers:

- *Principal (shell) quantum number (n)* is associated with successive orbitals. The binding energy between the electron and the nucleus is

proportional to $1/n^2$; where n is a positive integer 1, 2, 3, 4, ... that designates the K, L, M, N, ... shells, respectively.

- *Azimuthal (subshell) quantum number (l)* is a measure of the orbital angular momentum which, according to Sommerfeld, accounts for the existence of elliptic and circular electron orbitals; l can take all integral values between 0 and $(n - 1)$; $l = 0$ corresponds to a spherical orbital while $l = 1$ corresponds to a polar orbital. A value of $l = 0$ corresponds to s , $l = 1$ is p , $l = 2$ is d , and so forth.
- *Magnetic quantum number (m)* is responsible for determining the shape of an electron's probability cloud (but does not effect the electron's energy) and can take all the integer values between $-l$ to $+l$, including zero. The magnetic quantum number describes the orbitals within a sublevel. Thus for a given value of l , " m " has $(2l + 1)$ different values.
- *Spin quantum number (s)* can only take two possible values $+1/2$ and $-1/2$. The spin quantum number, allows two electrons of opposite spin (or symmetry) into each orbital.

The number of orbitals in a shell is the square of the principal quantum number (n) i.e., $1^2 = 1$, $2^2 = 4$, and $3^2 = 9$. Furthermore, there is one orbital in an s subshell ($l = 0$), three orbitals in a p subshell ($l = 1$), and five orbitals in a d subshell ($l = 2$). The number of orbitals in a subshell is given by $(2l + 1)$. Since each orbital can accommodate two electrons (one with spin up ($s = +1/2$) and one with spin down ($s = -1/2$) and thus each electron is existing in one of those strange probability clouds, which have widely varying shapes and sizes). The number of electrons in a subshell is given by $2(2l + 1)$. Electronic configuration in an energy state is usually designated by symbols containing a number and a letter containing an index, for example $3d^6$. The number "3" represents the principal quantum number while the letters s, p, d, f, g represent the l values 0, 1, 2, 3, 4, respectively. The index number indicates that there are six electrons in this quantum state. This is because of the reason that there are five different shapes for " d " and hence there is room for ten electrons i.e., $2(2l + 1)$. The numbers of electrons in any given state are controlled by Pauli's exclusion principle according to which no two electrons can have the identical combination of all the four quantum numbers. The electron configuration (say) for ^{17}Cl is $1s^2 2s^2 2p^6 3s^2 3p^5$. The first number represent the energy level, the letters represent the sublevel while the superscripts indicate the number of electrons in the sublevel. The total of the superscripts in an electron configuration equals the atomic number of the element.

The energy levels of different subshells are represented by notation such as $1s_{1/2}$, $2p_{1/2}$, $2p_{3/2}$, ... as shown in Fig. 1.3. States such as $1s_{1/2}$ means $n = 1$, $l = 0$, $j = 1/2$, $2p_{1/2}$ means $n = 2$, $l = 1$ and $j = 1/2$ and $2p_{3/2}$ means $n = 2$, $l = 1$, and $j = 3/2$, where $j = (l \pm s)$. Since the maximum number of electrons in any subshell is given by $(2j + 1)$, therefore the number of electrons in $2p_{1/2}$, $2p_{3/2}$ will be 2 and 4, respectively, making a total of 6 electrons in $2p$ state.

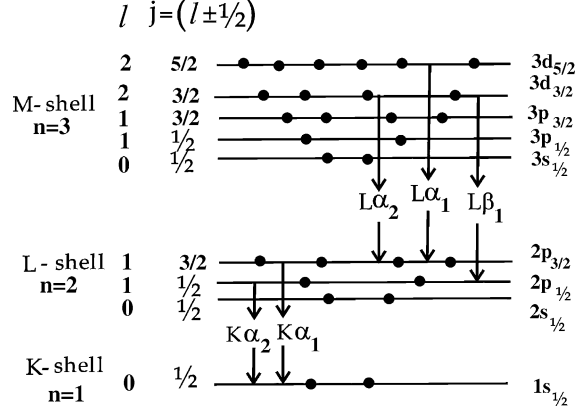


Fig. 1.3. Energy levels of different subshells of an atom along with their quantum numbers and occupancy of electrons

The XRF and PIXE spectra are primarily from transitions that occur after the loss of a $1s$ or $2s$ electron. Transitions that fill in the “ $1s$ ” i.e., K level are of the highest energy, and are called K-lines. $K\alpha_1$ and $K\alpha_2$ lines are from the $n = 2$ level to $n = 1$ level i.e., $K\alpha_1$ originate from $2p_{1/2}$ and $K\alpha_2$ from $2p_{3/2}$ and leave a hole in $2p$ -subshells while $K\beta$ lines leave a hole in the $3p$ shell. In spectroscopic notation:

$$K\alpha_1 \rightarrow 1s_{1/2} - 2p_{3/2}$$

$$K\alpha_2 \rightarrow 1s_{1/2} - 2p_{1/2}$$

The emission of X-rays is governed by the following selection rules for allowed electric dipole (E1) transitions:

$$\Delta n \geq 1, \Delta l = \pm 1, \Delta j = 0, \pm 1 \quad (1.1)$$

Since the spectroscopic notation for L_I, L_{II} , and L_{III} are $2s_{1/2}$, $2p_{1/2}$, and $2p_{3/2}$, respectively, while those for M_I, M_{II} , M_{III} , M_{IV} , and M_V are $3s_{1/2}$, $3p_{1/2}$, $3p_{3/2}$, $3d_{3/2}$, and $3d_{5/2}$, respectively; the spectroscopic notation for some L X-rays lines is given by

$$L\alpha_1 \rightarrow 2p_{3/2} - 3d_{5/2}$$

$$L\beta_1 \rightarrow 2p_{1/2} - 3d_{3/2}$$

The most important of the forbidden transitions are the magnetic dipole (M1) transitions for which $\Delta l = 0$; $\Delta j = 0$ or ± 1 and the electric quadrupole (E2) transitions for which $\Delta l = 0, \pm 2$; $\Delta j = 0, \pm 1$, or ± 2 .

1.3.1 Spectral Series, The Moseley Law

By definition, a spectral series is a group of homologous lines, e.g., the $K\alpha_1$ lines or $L\alpha_1$ lines, etc. of all the elements. In 1913, Moseley established an

experimental relation between the frequency (ν) of X-rays for each spectral series and the atomic number Z of the element from which it was emitted and expressed it as:

$$\nu = Q(Z - \sigma)^2$$

where Q is the proportionality constant and σ is so-called screening constant. The value of Q is $(3R/4) \times c$ for $K\alpha$ and $(5R/36) \times c$ for $L\alpha$ transition. Here c is the velocity of light ($= 3 \times 10^8 \text{ ms}^{-1}$) and R is the Rydberg constant ($= 2\pi^2 me^4/h^3$) which is numerically equal to $1.09737316 \times 10^7 \text{ m}^{-1}$. The energy of different classical circular orbitals is calculated using $E_n = RZ^2h/n^2$ (since $E_n = 2\pi^2 me^4 Z^2/n^2 h^2$), where h ($= 4.136 \times 10^{-15} \text{ eVs}^{-1}$) is the Planck's constant. The energies of $K\alpha$ and $L\alpha$ X-ray lines can be derived from Bohr's theory will thus be given by:

$$E_{K\alpha} = (3/4)(Z - \sigma)^2 E_f; \quad E_{L\alpha} = (5/36)(Z - \sigma)^2 E_f \quad (1.2)$$

where E_f is the ionization energy of hydrogen atom i.e., 13.6 eV.

The X-ray energies of various $K\alpha$ and $L\alpha$ lines increase as a smooth function of the atomic number Z according to the Moseley law $E_x = Z_{\text{eff}}^2 \left(\frac{1}{n^2} - \frac{1}{m^2} \right)$. Here n indicates the lower energy level e.g., 1 for K X-rays, 2 for L X-rays, and so on, while m is the energy level of the higher state e.g., $m = 2, 3, \dots$. These transitions are energetic enough not to get varied much with oxidation state or chemical bonding of the element. These are therefore used as the fingerprints of various elements to which they belong.

1.3.2 Line Intensities and Fluorescence Yield

The intensity of emission of a particular line (say $L\alpha_1$ which is $L_{\text{III}}-M_{\text{V}}$ transition) will depend upon various factors, e.g., (a) the probability that the incident radiation will ionize an atom on the L_{III} level; (b) the probability that the vacant site created on L_{III} will be filled by an M_{V} electron; and (c) the probability that the $L\alpha_1$ photon will leave the atom without being absorbed within the atom itself (Auger effect).

To calculate the relative intensities of allowed and emitted X-ray lines, we make use of the "sum rule" which states that the total intensity of all lines proceeding from a common initial level or to common final level is proportional to the statistical weight $(2j + 1)$ of that level. For example, the $K\alpha_2 : K\alpha_1 = 1 : 2$ (if these are the only electronic transitions proceeding from the L_{II} i.e., $2p_{1/2}$ and L_{III} i.e., $2p_{3/2}$ subshells) because these transitions are $K \rightarrow L_{\text{II}}$ and $K \rightarrow L_{\text{III}}$, respectively, and the ratio of the line intensities will be the statistical weights of the levels from which the electrons originate i.e., $L_{\text{II}} : L_{\text{III}}$ for which $(2j + 1) = 2 : 4$ i.e., $1 : 2$. The intensity ratio $I(K\alpha_2)/I(K\alpha_1)$ varies from 0.503 to 0.533 for elements from $_{20}\text{Ca}$ to $_{50}\text{Sn}$ while $I(K\beta)/I(K\alpha)$ increases from 0.128 to 0.220 for the above range of elements. The variation in the relative intensities within the L-spectra is more noticeable as given in Table 1.2.

Table 1.2. The variation in the relative intensities of L X-ray transitions

Line →	L α_1	L α_2	L β_1	L β_2	L γ_1	L l
Relative Intensity	100	10	50–100	10–20	5–10	3–6

Fluorescence yield is one of the major factors that determine the intensities of X-ray spectra. For each excited state of an isolated atom, the fluorescence yield is defined as $\omega_x = \Gamma_x / \Gamma_{\text{tot}}$ in terms of the radiative and total transition probabilities “ Γ ” for the particular state (the transition probabilities further depend on the angular momentum quantum number, the number of electrons available for transition as well as the excitation energy). The average fluorescence yield is also determined from $\omega_x^{\text{av}} = \frac{\sigma_x}{\sigma_x + \sigma_A}$ where σ_x and σ_A represent the X-ray and Auger electron cross-sections, respectively.

Thus the fluorescence yield (ω_K) is related to the number of photons emitted in unit time divided by the number of vacancies formed at that time i.e.,

$$\omega_K = \frac{n K\alpha_1 + n K\alpha_2 + n K\beta + \dots}{N_K} \quad (1.3)$$

For L- and M-shells comprising of three and five subshells, respectively, if N excited states are produced with population distribution n_i each having fluorescence yield ω_x^i , then the average fluorescence yield for the distribution is given by $\omega_x^{\text{av}} = N^{-1} \sum_i n_i \omega_x^i$.

Fluorescence yield values increase with atomic number and also differ significantly from one electron shell to another: ω_K is much larger than ω_L and ω_L is much larger than ω_M . The values of ω_K are known with a higher degree of accuracy than the ω_L values (Bambynek et al. 1972) because the former relate to a one-level shell while the latter are weighted averages for the L_I, L_{II}, and L_{III} shells. Experimental results indicate that ω_K increases from 0.0025 to 0.901 for elements ${}_6\text{C}$ to ${}_{56}\text{Ba}$.

1.3.3 Critical Excitation Energies of the Exciting Radiation/Particles

For analysis by XRF technique, the energy of the exciting radiation should be more than the binding energy of the particular shell/subshell (from which the electron has to be knocked out) so that the electron ejection takes place. For example the energy of the incident photon ($h\nu$) should be greater than the binding energy of the K-shell (E_K), called K absorption edge for K α and K β X-ray emission and should be greater than L_I, L_{II}, or L_{III} for L β_3 (L_I-M_{III}), L β_1 (L_{II}-M_{IV}), and L $\alpha_{1,2}$ (L_{III}-M_V, M_{IV}) X-ray emission, respectively.

For analysis by PIXE technique, if the incident projectile of charge “ Z_1 ” and mass “ M_1 ” is moving with velocity “ V_1 ” (and hence energy $E_0 = M_1 V_1^2 / 2$) to eject an inner-shell electron from the target having mass M_2 , the energy transferred in a head-on collision is

$$T_m = \frac{4M_1M_2E_0}{(M_1 + M_2)^2} \approx \frac{4M_1E_0}{M_2} \quad (1.4)$$

Considering that the ejection of the inner-shell electron occurs because of the energy transfer in the collision, the threshold for causing the vacancy due to electron ejection will occur when $T_m = E_K$ (K-shell B.E). Hence $E_0 = (M_2/4M_1) \times E_K = U \times E_K$ where $U = M_2/4M_1$. The experimental results indicate that X-rays are produced at values of U considerably less than this, which indicates that the ionization occurs not by collision with a free electron but by collision with the atom as a whole. Under these circumstances, considerably greater amount of energy can be transferred since the projectile energy is required to be more than the energy of the emitted X-ray for reasons of energy conservation. Since the beam energy is always higher than the limiting value of ~ 100 keV, one can safely say that there is no threshold for X-ray production exists in PIXE analysis. There is a threshold of course, which is related to the molecular overlap of orbitals between the individual atoms (target and incident particle) and the compound atom (target plus incident particle). Merzbacher and Lewis (1958) have set a lower limit of 100 keV for incident particle energy, which allows the inequality $\frac{1}{4\pi\epsilon_0} \times \frac{ze^2}{\hbar v} \ll 1$ to apply.

In the process of X-ray production by electron bombardment however, the electron energy (product of electron charge e and accelerating potential V) must be greater than the binding energy of the shell (i.e., E_K for K X-rays).

The basic concepts regarding ion-energy, ion-current, relative ion velocity, atomic sizes and orbital electron velocities, energy transferred to electrons is discussed in the subsequent sections.

Ion-Energy and Ion-Current

The ion energy depends on the type of accelerator, whether it is single ended or tandem-type. For a single-ended accelerator, $E = qV$ i.e., for 3 MV acceleration voltage, protons will have energy of 3 MeV while Cl^{10+} ions will have energy of 30 MeV. For the Tandem accelerator with accelerating potential of “ V ” MV where we start with the singly charged negative ions from the source, the energy of the ion beam $E = (q + 1)V$.

Since the ion current $I = qe/t$, therefore the ion currents (number of ions/s) $N/t = I/qe$ will be 6×10^6 for 1 pA and 6×10^4 for 100 pA of proton and deuteron beam having $q = 1$. For still heavier ions, the q value will be equal to the charge state of the ions produced in the ion-source due to stripping in the C-foil or Ar-gas. For example for ${}^4\text{He}^{1+}$ and α -particle (${}^4\text{He}^{2+}$), the charge state (q) values are 1 and 2, respectively. Similarly for ${}^{12}\text{C}^{q+}$, the charge state can have any value between 1 and 6 depending on the number of electrons present on the C-ion. In this case, since the atomic number (Z) of carbon atom is equal to 6, the q -value will be equal to 1, 2, 3, ..., 6 if number of intact electrons on the C-ion are 5, 4, 3, ..., 0 and so on.

Relative Ion Velocities

Since the ion velocity $V_1 = 1.384 \times 10^9 \sqrt{(E_0/M_1)} \text{ cm s}^{-1}$

Therefore $(V_1/c) = 0.046 \times \sqrt{(E_0/M_1)}$, where E_0 is in MeV and M_1 is in amu

Thus Relative velocity of 1 MeV protons = 4.6% of velocity of light

Relative velocity of 4 MeV protons = 9.2% of velocity of light

Similarly

Relative velocity of 2 MeV deuterons = 4.6% of velocity of light

Relative velocity of 8 MeV deuterons = 9.2% of velocity of light and

Relative velocity of 4 MeV α -particles = 4.6% of velocity of light

Relative velocity of 16 MeV α -particles = 9.2% of velocity of light

Atomic Sizes and Orbital Electron Velocities

Shell radius $(a_n) = 0.53(n^2/Z)$

Relative velocities of atomic electrons $(v_e/c) = Z/(137n)$, where n is the principal quantum number.

For $_{13}\text{Al}$ K shell $(v_e/c) = 9.5\%$, for $_{20}\text{Ca}$ K shell $(v_e/c) = 14.6\%$

and for $_{30}\text{Zn}$ K-shell electrons $(v_e/c) = 21.9\%$

For $_{82}\text{Pb}$ K shell $(v_e/c) = 59.8\%$, Pb L shell $(v_e/c) = 29.9\%$ and

Pb M shell $(v_e/c) = 20\%$

Maximum cross-sections corresponding to velocity matching demands that the ion velocities from accelerators be comparable with bound electron velocities.

Energy Transferred to Electrons

Since the proton energy $E_p = 0.5 m_p v_p^2$, therefore for protons energy of 1 MeV, energy transferred to electrons $T = 0.5 m_e v_e^2$ comes out to be just 11 keV due to ratios of masses of electrons and the velocities of electrons and protons.

Why Particle Energy in the Range of 1–4 MeV u^{-1} ?

For Protons

We know that E_p should be less than the Coulomb barrier (E_C) is given by:

$$E_C = \frac{Z_1 Z_2}{\left(M_1^{1/3} + M_2^{1/3}\right)} \text{ MeV} \quad (1.5)$$

The velocity matching consideration demand that the maximum ionization cross-sections occur around ion energy (MeV u^{-1}) given by:

$$E_p = 134 U^2 n^4 / Z_2^2 \quad (1.6)$$

For K-shell ionization of $_{15}\text{P}$ ($U = 2.1 \text{ keV}$) $\Rightarrow E_p = 2.4 \text{ MeV u}^{-1}$

For K-shell ionization of $_{20}\text{Ca}$ ($U = 3.7 \text{ keV}$) $\Rightarrow E_p = 4.6 \text{ MeV u}^{-1}$

For Deuterons and α -Particles

With heavy ions, the value of ionization cross-section σ_K , σ_{Li} can be calculated from the corresponding proton values using the Z_1^2 scaling law, e.g.,

$$\sigma_{Li}^{ion}(E) = Z_1^2 R \sigma_{Li}^{ion}(E_1/M_1)$$

Thus

$$\begin{aligned}\sigma_D(E) &= \sigma_p(E/2) \text{ i.e. } 2 \text{ MeV protons} \Rightarrow 4 \text{ MeV deuterons} \\ \sigma_{He}(E) &= 4\sigma_p(E/4) \text{ i.e. } 2 \text{ MeV protons} \Rightarrow 8 \text{ MeV } \alpha\text{-particles}\end{aligned}$$

1.4 Instrumentation/Experimentation

1.4.1 Modes of Excitation for XRF Analysis

X-ray fluorescence spectroscopy can be accomplished using (a) radioactive sources as exciters or (b) X-ray tube as exciter.

Radioactive Sources as Exciters

A radioactive source (preferably monochromatic) can be used as an exciter. The sources of ^{55}Fe , ^{109}Cd and ^{241}Am of a few milliCurie (mCi) activity are used as primary sources. The half-life, X-ray/ γ -ray energies and analysis range of elements are listed in Table 1.3. For more energies however, the secondary exciters using Cu (8.14 keV), Se (11.37 keV), Y (15.2 keV), Mo (17.8 keV), Sn (25.8 keV), Sm (41.0 keV), and Dy (46.9 keV) can be used with Am^{241} as a primary source. X-rays from the primary source are directed at a selectable secondary exciter target, usually Tin (Sn). The

Table 1.3. Various radioisotopes used as excitation sources

Isotope	Half-life	Energy (keV)	Analysis Range
$^{55}\text{Fe}^a$	2.7 yr.	5.9, 6.4	Al to Cr for K X-rays
$^{109}\text{Cd}^b$	470 days	22.16, 24.94 88.03 (γ)	Ti to Ru K X-rays Ta to U for L X-rays
^{241}Am	433 yr.	59.6	Fe to Tm for K X-rays Ta to U for L X-rays

^a ^{55}Fe decays through EC (100%) to the ground state of ^{55}Mn . The excitation X-rays are the lines from ^{55}Mn .

^b ^{109}Cd decays to the 88 keV excited state of ^{109}Ag through EC(100%) which further decays to the ground state of ^{109}Ag through γ -ray emission. Thus, the excitation line is the 88.03 keV γ -transition from ^{109}Ag . Using 88 keV γ -transition of ^{109}Cd , one can excite K X-rays of elements from Ru to Pb. (The 22.16 and 24.94 keV are the $K\alpha$ and $K\beta$ lines from ^{109}Ag .)

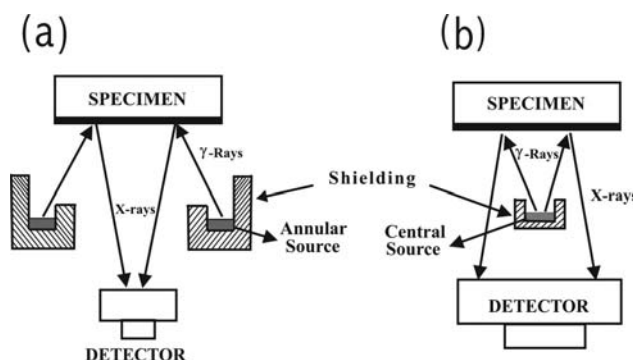


Fig. 1.4. Geometries applied in radioisotope-induced XRF analysis using (a) annular source and (b) central source

characteristic X-rays from that exciter target are aimed at the unknown sample. This causes emission (fluorescence) of characteristic X-rays from the sample. These X-rays from the sample are captured in a Si(Li) detector and analyzed by computer. The energy spectrum of these X-rays can be used to identify the elements found in the sample.

Typical geometries applied in radioisotope-induced XRF analysis (Lal 1998, Bandhu et al. 2000) using annular and central source are shown in Fig. 1.4a, b. A graded shield of copper and aluminum suppresses low-energy photons in the source. Tungsten alloy collimator with Al lining collimates the photon beam from the secondary X-ray exciters of different metals. A tungsten shield covers the source to avoid direct radiation exposure of the detector. There is a tungsten spacer, which defines the secondary fluorescence target cavity when used in secondary excitation mode and acts as a spacer in the direct excitation mode.

Table 1.3 lists various radioisotopes used as excitation sources for XRF analysis. To perform the qualitative and quantitative XRF analysis based on a radioisotope excitation, one should know the relative intensities and the precise energies of the X- or γ -rays emitted by the source. Verma and Pal (1987) have calculated the K and L X-ray emission intensities for some radio nuclides (^{141}Ce , ^{143}Ce , ^{152}Eu , ^{159}Dy , ^{160}Tb , ^{169}Yb , ^{237}U , and ^{239}Np) using the latest data for γ -ray intensities, electron capture, and internal conversion coefficients for the parent nuclides, fluorescence yield values and Coster-Kronig transition probabilities.

The influence of the photons emitted by a ^{241}Am XRF excitation source below 59.6 keV on sample fluorescence production has been analyzed and general method for evaluating the contribution of the various lines from the source in specific equipment configurations is presented by Delgado et al. (1987). A typical L X-ray spectrum of Pb by ^{241}Am source (Kumar et al. 1999) is presented in Fig. 1.5, which also shows the peaks due to elastically- and inelastically-scattered photons from the ^{241}Am source.

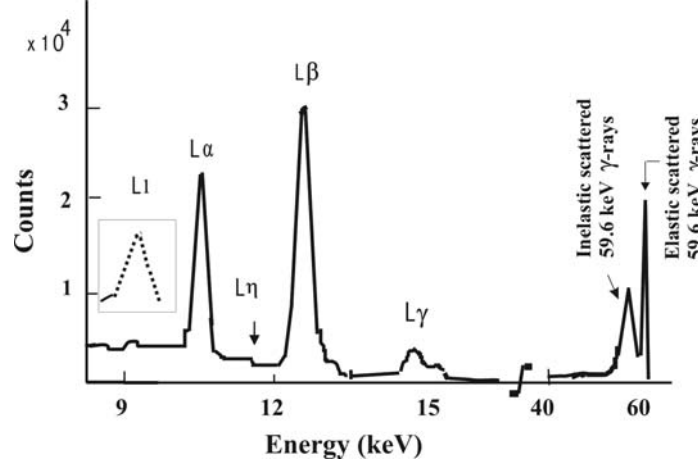


Fig. 1.5. Typical L X-ray spectrum and scattered photons from Pb target by ^{241}Am source

The excitation by X-ray sources requires the knowledge about the values of critical excitation energies of different sources to enable the excitation of inner-shell electrons of various elements present/expected to be present in the sample. Two basic processes i.e., the attenuation and the scattering of X-rays are involved when the intensity is reduced to I_x after the photon beam of intensity I_o passes through the material of thickness x . The reduced intensity is given by Lambert law $I_x = I_o \exp(-\mu x)$, where μ is called the linear attenuation coefficient. The mass attenuation coefficient is further related to the linear attenuation coefficient by $\mu_m = \mu/\rho$ and is the sum of mass photoelectric absorption coefficient (τ) and mass scattering coefficient (σ) expressed in $\text{cm}^2 \text{g}^{-1}$. It means that the fraction of intensity ($I_o - I_x$) that is not transmitted in the same direction as the incident photons is lost mainly as a result of absorption due to photoelectric effect (giving rise to ionization of the atom and emission of X-rays) and the scattering (incoherent/inelastic scattering increasing the wavelength of the incident radiation called Compton scattering or coherent/elastic scattering of unmodified wavelength called Rayleigh scattering). In the low-energy range of photons ($<100 \text{ keV}$), the photoelectric absorption coefficient is almost 95% of the attenuation coefficient μ_m . The significant property of the photoelectric absorption coefficient, for any element, is that it increases rapidly with decreases in energy of the photon, falls off vertically at particular value (called the absorption edge) and then again starts increasing again as shown in Fig. 1.6.

The sharp discontinuities in the absorption curve are related to the critical excitation energies (and their corresponding wavelengths) of the element for the K-shell/ L_I , L_{II} , and L_{III} subshells of the L-shell/ M_I , M_{II} , M_{III} , M_{IV} , and M_V subshells of the M-shell, etc. The K- and L-shell absorption edges for a few elements given in wavelength (\AA) by Bearden (1967), converted in keV,

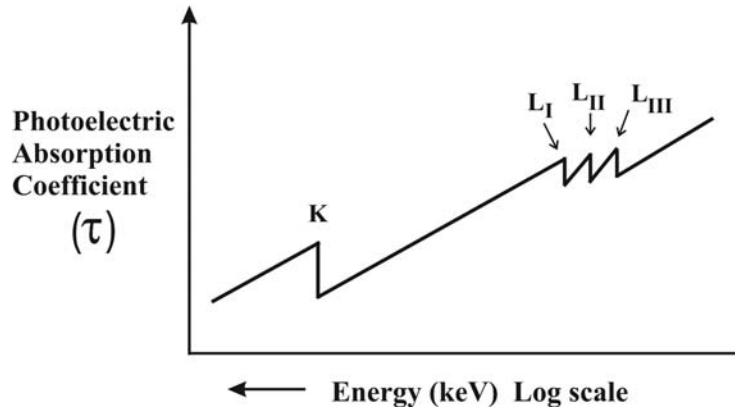


Fig. 1.6. Schematic diagram showing the variation of the photoelectric absorption coefficient as a function of energy for a typical target element

Table 1.4. The K- and L-shell absorption edges for a few elements

Element	Absorption Edge (in keV)			
	K	L _I	L _{II}	L _{III}
¹¹ Na	1.072			
¹³ Al	1.560			
²⁰ Ca	4.040			
²⁹ Cu	8.980		0.953	0.933
³⁴ Se	12.653	1.653	1.475	1.434
³⁹ Y	17.033	2.377	2.154	2.080
⁴⁹ In	27.928	4.238	3.940	3.730
⁶³ Eu	48.627	8.062	7.621	6.982
⁷³ Ta	67.391	11.687	11.131	9.880
⁷⁹ Au	80.519	14.352	13.732	11.923

are presented in Table 1.4. For example, for ⁷³Ta, the K absorption edge is at 67.391 keV while the L_{III}, L_{II}, and L_I absorption edges are at 9.880, 11.131, and 11.687 keV, respectively, which means that at 9.880 keV, the critical value for excitation of the L_{III} energy level is reached and ionization at this level is now possible, the sharp increase in absorption that results is called the L_{III} absorption edge. The K absorption edge at 67.391 keV indicates that at energies higher than this, the absorption decreases to very low values.

To detect the X-rays emerging from the sample, a solid state Si(Li) detector, cooled to liquid nitrogen temperature, is used to detect the characteristic X-rays. The detector has a resolution of about 160 eV at 5.9 keV. The pulses from the detector are processed by a shaping amplifier and converted into pulse height by the analog-to-digital converter (ADC) of the multichannel analyzer (MCA).

X-ray Tube as Exciter

X-ray tubes offer greater analytical flexibility at a cost of more complexity. Main features of X-ray tube are as given in Table 1.5.

The considerations for the applied Voltage are as follows:

1. At 50 kV, all K-lines up to $Z = 63$ (Eu) are excited.
2. At 100 kV, all K-lines up to $Z = 87$ (Fr) are excited.
3. 100 kV will excite all K-lines more efficiently than 50 kV, but there are no dispersive crystals available to diffract the lines at a reasonable angle and the background increases so that the line/background remains essentially the same.
4. The intensity of the characteristic X-ray lines of the target of the X-ray tube (overriding the background continuum) are given by $I = A C(V - V_K)^n$, where A is constant, C is the current, V is the applied voltage which must be equal to the critical voltage V_K (in the case of K-lines) and the exponent is a constant that has a value between 1.5 and 2 depending on the emission line. The rapid increase in intensity predicted by the earlier equation does not materialize when V exceeds three or four times the critical voltage V_K or V_L .
5. The short wavelength limit is given by λ_0 i.e., the spectrum starts abruptly at a wavelength that does not depend on the target material but follows the relation.

$$\lambda_0(\text{in } \text{\AA}) = \frac{12.39813}{V(\text{in kV})} \quad (1.7)$$

Further, the shorter wavelength limit λ_0 varies as the reciprocal of the applied voltage.

Excitation by the characteristic tube lines may be accomplished by having several different target tubes (^{24}Cr , ^{29}Cu , ^{42}Mo , ^{45}Rh , ^{74}W , ^{78}Pt or the dual target W/Cr) in any of the desired energy ranges. Mo has advantage for K-lines of ^{32}Ge to ^{41}Nb and L-lines from ^{76}Os and up while Cr is best target for K-lines from ^{23}V down and L-lines from ^{58}Ce down. By anode selection, the operator is able to enhance the K lines of Molybdenum (~ 17 keV), the L lines of tungsten (~ 8 and 10 keV) or the L lines of Molybdenum (~ 2.3 keV). By using these lines, especially with a proper filter in between tube and sample, the operator is able to excite fluorescence. Characteristic tube excitation can be used in conjunction with a filter of the target material to reduce the

Table 1.5. Main features of an X-ray Tube

Tube voltage	10–100 kV in steps of 5 kV
Tube current	0–100 mA in steps of 1 mA
Vacuum Pump	Diffusion-Rotary pump
Operating pressure	$\approx 10^{-6}$ Torr
Water flow rate	≈ 4 litre/min

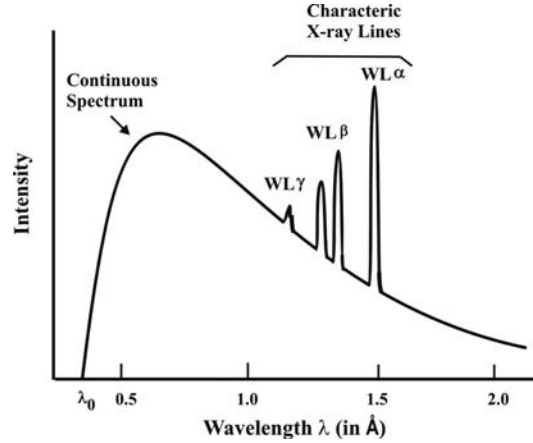


Fig. 1.7. Typical emission spectrum from a $_{74}\text{W}$ target X-ray tube

background. A typical emission spectrum from a $_{74}\text{W}$ target X-ray tube is shown in Fig. 1.7.

The continuum or Bremsstrahlung radiation from high atomic number target elements of the tube, which extends to the highest energy of the electron beam, may also be used for excitation. For example the elements up to curium ($K\alpha \sim 40 \text{ keV}$) may be fluoresced using the Bremsstrahlung spectrum and W-target. Both of these give high background. One can find the shortest wavelength λ_0 (highest energy) photon that can be emitted, which corresponds to the incident electron losing all of its kinetic energy in a single collision. For a 35 kV accelerating voltage, the shortest wavelength X-ray that can be emitted is about 0.035 nm. Thus, the continuous part of the X-ray spectrum spans the range from λ_0 to infinitely long wavelengths. The continuous spectrum is used for X-ray diffraction experiments (where X-rays are diffracted by cubic crystals to determine their orientation in space). By changing the target material of the X-ray tube, the effect caused on the continuous X-ray spectrum can be elaborated with reference to Fig. 1.7. The continuous part of the X-ray spectrum varies in intensity with wavelength (equivalent with photon energy $E = hc/\lambda$). There is a broad intensity peak for wavelength near 0.4 \AA (0.04 nm), which is somewhat smaller than the spacing of atoms in crystalline solids. The photons with longer wavelengths (lower photon energy) are emitted, although the intensity is not as great as that produced at shorter wavelengths.

Characteristic X-rays are usually used in diffraction experiments where the sample has many different crystal orientations, such as in a polycrystalline or powder sample, as well as for single crystal structure determination. The $K\alpha$ characteristic line is preferred for use in such experiments since it has the highest intensity. To filter the output of an X-ray tube with the purpose of selecting the prominent line of the target X-ray of the tube, the filter is

chosen with an absorption edge between the two peaks to cause preferential absorption of the peak with shorter wavelength. For example, one mil (0.001") thick brass foil plus a 1 mil nickel foil can be used over the window of the tungsten X-ray tube. The copper and zinc content in the brass causes high absorption of $L\beta$ and $L\gamma$ tungsten lines, while nickel causes high absorption of the $L\alpha$ tungsten lines.

Wide ranges of X-ray tubes are available with side or end windows. Latest developments in tube technology are the introduction of the dual-anode tubes. In a dual anode tube, a layer of chromium is deposited on a gold substrate or scandium on a molybdenum substrate. At low power the tube behaves like a conventional chromium or scandium tube, but at higher voltages, the radiation from the underlying anode materials is produced to give more excitation of the heavy elements. This enables a single X-ray source to be used over a broad atomic range or in other words excitation can be optimized for general purpose working or for more specialized tasks. The direct optical position sensor (DOPS) goniometer provides remarkable accuracy and reads the θ and 2θ positions from finely etched grating disks which are fitted onto the goniometer axes.

An alternative geometrical set-up known as triaxial geometry (Bandhu et al. 2000) consists of an X-ray tube to fluoresce a selectable secondary target such as Ti, Ag, Ba and to reduce the backscattered radiation is as shown in Fig. 1.8.

The energy of the characteristic X-ray lines produced will be less than the energy of the exciter X-rays. Hence the selection of the target for the X-ray tube is very important. The choice of exciter will depend on the absorption edges of the elements (Table 1.4) present in the sample. Characteristic X-ray production is most efficient when the excitation energy is just above the absorption edge of the particular element of interest. There is a possibility for the variation of voltage (kV) and current (mA) applied to the X-ray tube. The kV and mA settings determine the efficiency with which the X-ray lines are excited in the tube and thus in the sample. The X-ray intensity increases

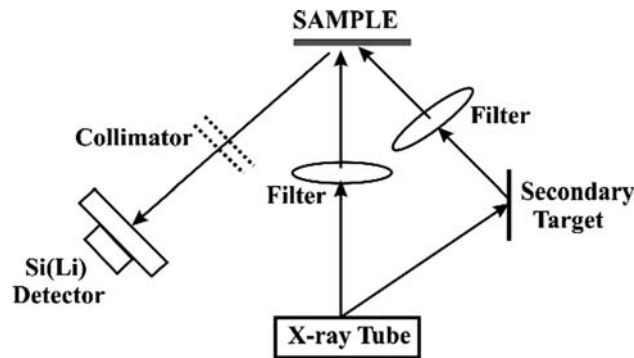


Fig. 1.8. The energy dispersive X-ray fluorescence set-up with triaxial geometry

when either the anode voltage or the emission current is increased. However, the characteristic X-ray lines get broadened as the anode voltage is increased.

If the absorption of characteristic radiation in target material itself is accounted, then the intensity of characteristic radiation depends on the anode voltage as $I \propto (V - V_K)^{1.65}$ where V is the applied high voltage and V_K is the K absorption edge expressed in volts (8.98 kV for Cu). As the anode voltage is increased, the Bremsstrahlung radiation spreads toward high energy side and its intensity follows the quadratic relationship of high voltage so that it goes on increasing as anode voltage increases. Besides this, the intensity of characteristic radiation gets saturated after some value of anode voltage. This behavior is manifestation of self-absorption effect in target material. It is known that for $V > V_K$, the electron penetration depth in the target becomes large compared to the maximum depth from which the characteristic X-rays can come out.

X-ray tubes usually have a power output of 3 kW and may be either a side window or end-window type. The low-power X-ray tube could be used for EDXRF while power of the tube for WDXRF is 3–4 kW. Direct excitation using a high-power X-ray tube and EDXRF allow to reach detection limits in the parts per billion or picogram range.

1.4.2 X-ray Detection and Analysis in XRF

The X-rays detection and analysis is usually carried out in two modes:

- *Wavelength dispersive X-ray spectroscopy (WDS)* uses the reflection of X-rays off of a crystal at a characteristic angle to detect X-rays of specific wavelength.
- *Energy dispersive X-ray spectroscopy (EDS)* works on the principle of separating and detecting X-rays of specific *energy* and displays them as histograms. Imaging of elements is also possible using this capability.

Wavelength Dispersive (WD) X-ray Spectrometry

Wavelength dispersive X-ray fluorescence relies on a diffractive device such as a crystal, to isolate the peak corresponding to an analytical line since the diffracted wavelength is much more intense than other wavelengths that scatter of the device. The excitation in WDXRF is carried by X-ray tube. The detection and measurement of intensity is based on the principle of X-ray diffraction i.e., the characteristic X-rays of each element have a distinct wavelength, and by adjusting the tilt of the crystal (which will select and diffract only a small fraction of the incoming X-rays at each angle θ) in the spectrometer, at a specific angle it will diffract the wavelength of specific element's X-rays. Diffraction obeys the Bragg equation

$$n\lambda = 2d \sin \theta \quad (1.8)$$

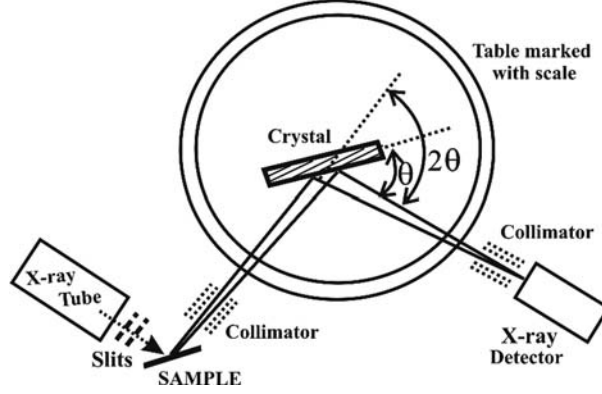


Fig. 1.9. Principle and Schematic of WDXRF spectrometry

where λ is the wavelength of the X-ray line, $2d$ is the lattice spacing, and θ is the angle of diffraction. The wavelength λ may be converted to energy using the formula:

$$E(\text{in keV}) = \frac{12.398}{\lambda}(\text{in } \text{\AA}) \quad (1.9)$$

The system used in conventional wavelength dispersive spectrometry generally consists of an X-ray tube, an analyzing crystal, and detector (scintillation or gas flow proportional counter) as shown in Fig. 1.9.

The diffracted beam will pass through a 0.02° receiving slit and then into a scintillation detector (for medium to high-energy X-rays) or gas flow proportional detector with a specially prepared thin polyester film window (for medium to low-energy X-rays). The gas-flow proportional counting tube has a tin wire running down its middle, at 1–2 kV potential. The X-rays are absorbed by gas molecules (e.g., P10: 90% Ar, 10% CH₄) in the tube, with photoelectrons ejected; which in turn produce a secondary cascade of interactions, yielding an amplification of the signal ($\times 10^3$ – 10^5) so that it can be handled by the electronics. This signal is sent simultaneously to a rate meter and a strip chart recorder. The output on the strip chart is given in “Intensity vs. 2θ ”, where θ is the angle of diffraction. Improvement in the whole electronic counting chain, including the pulse height selector have increased the count rate capability $\sim 10^6$ cps with accuracy and linearity of better than 1%. The angle corresponding to any wavelength can be calculated using the relation $\theta = \sin^{-1}(n\lambda/2d)$ where n is the order of diffraction. Corresponding to the wavelength of X-ray lines, $2d$ value of the crystal and the order of diffraction, the detection range (θ -values) can be calculated. Different diffracting crystals, with $2d$ (lattice spacing) varying from 2.5 to 100 Å, are used to be able to “reach” the different wavelengths of various elements. In recent years, the development of “layered synthetic crystals” of large $2d$ has lead to the ability to analyze the lower Z elements (Be, B, C, N, O), although inherent limitations in the physics of the process (e.g., large loss of signal by absorption

Table 1.6. Common dispersing crystals and their characteristics

Crystal ^a /Plane	$2d$ (Å)	Detection Range/Lowest- Z Detection	
		for K X-rays	for L X-rays
LiF (220)	2.848	^{23}V	^{58}Ce
LiF (200)	4.028	^{19}K	^{49}In
NaCl (200)	5.639		
Calcite (103)	6.071		
Si (111)	6.276	^{15}P	^{40}Zr
Ge (111)	6.533	^{15}P	^{40}Zr
Quartz (1011)	6.686		
ADP (1011)	7.498		
EDDT (020)	8.742	^{13}Al	^{35}Br
PET (022)	8.808	^{13}Al	^{35}Br
ADP (101)	10.648		
Mica (002)	19.949		
TAP (1011)	25.763	^8O	^{23}V
RAP (010)	26.115		
KAP (1010)	26.632		

^aADP \Rightarrow Ammonium di-hydrogen Phosphate, KAP \Rightarrow Potassium Acid Phthalate, TAP \Rightarrow Thallium Acid Phosphate, EDDT \Rightarrow Ethyl di-amide D-Tartrate ($\text{C}_6\text{H}_{14}\text{N}_2\text{O}_6$), PET \Rightarrow Penta Erythritol, RAP \Rightarrow Rubidium Acid Phthalate.

in the sample) limit the applications. Table 1.6 later lists the names of a few analyzing crystals along with their $2d$ values and detection range.

A collimator is positioned at sample changer port between the crystal and detector to restrict the angles that are allowed to strike the diffraction device. Sollar slit and similar types of collimators are thus used to prevent beam divergence. It intercepts divergent secondary radiation from sample so that a parallel beam arrives at crystal and at detector window. The effect of increased collimation improves effective resolution and decreases background. However, it also decreases the line intensity. The path of X-rays could be either through air or vacuum. Air is suitable for K-lines of ^{26}Fe and above and L-lines of ^{72}Hf and above while vacuum can help to detect elements even for low- Z elements like ^{12}Mg .

As an example, let the specimen at the center of the goniometer be a single crystal of LiF with (200) planes parallel to the large face. The crystal is bombarded by all X-rays, continuous and characteristic, which are emitted from the X-ray tube. However, it passes on, or diffracts, only that wavelength which satisfies Bragg's law. Thus, at $2\theta = 40^\circ$ for example (i.e. $\sin\theta = 0.342$) and with $2d = 4.028 \text{ Å} = 0.4028 \text{ nm}$, those X-rays diffracted to the counter have a wavelength $\lambda(2\theta = 40^\circ) = 0.1378 \text{ nm}$.

The wavelength dispersive spectrometry has an overall low efficiency owing to several intensity losses through the restriction on solid angles and the low "reflectivity" of the analyzing crystal. Furthermore, the qualitative method of

unknown materials by WDXRF is often a slow process, implying a series of scans with several analyzing crystals to cover the whole X-ray spectrum and their interpretations.

Soft X-rays ($E < 1 \text{ keV}$) are rapidly absorbed by matter and have escape depths from a solid surface only a few μm corresponding to approximately the top thousand atomic layers of a sample. Therefore changes in peak profile, satellite peaks, etc., which are informative of chemical effects, can be used to infer chemical changes in sample surfaces. Since the air attenuation of X-ray becomes quite significant at low energies, the entire sample chamber is placed in vacuum.

The flat crystal spectrometer consists of a crystal mount located at the center of a turntable on which the detector rides. A precision stepping motor drives gear train, which causes the rotation of the crystal mount through the Bragg angle θ° ($\sim 0.01^\circ/\text{step}$) while at the same time the turntable rotates through angle $2\theta^\circ$. In this way when the crystal reflects at angle θ° , the detector is maintained in the correct position (at angle $2\theta^\circ$) to observe X-ray, which satisfies the Bragg equation (1.7). The energy resolution of the spectrometer can be estimated from the relation

$$\Delta E = (dE/d\theta) \Delta\theta = E \cot \theta \Delta\theta \quad (1.10)$$

where E is the X-ray energy and $\Delta\theta$ is the angular divergence of the X-rays incident on the Bragg crystal. The best energy resolution is obtained with a crystal having a $2d$ -spacing only slightly greater than the wavelength of interest. For a flat crystal spectrometer the angular divergence is primarily determined by a set of entrance parallel plate collimators (sollar slits). Similar set of soller slits in front of the detector can be used to reduce background due to scattered X-rays and electrons.

Detection of the reflected X-rays is accompanied by means of either a gas flow proportional counter or a NaI (Tl) scintillation detector. Since the energy resolution of the crystal spectrometer $\approx 1\text{--}2 \text{ eV}$, it not only distinguishes the $K\alpha_1$, $K\alpha_2$, $K\beta_1$, and $K\beta_2$ diagram lines clearly but is also able to yield information about the nondiagram lines (satellite and hypersatellite lines) in the complex K X-ray spectrum. The $K\alpha$ satellite lines will be represented as $K\alpha(2p)^5$, $K\alpha(2p)^4$, $K\alpha(2p)^3$, ... meaning that 5, 4, 3, ... electrons remain intact in the 2p shell while $K\alpha(2p)^6$ will represent the $K\alpha$ principle line with all the six 2p electrons intact. Similar terminology is also used for $K\beta$ satellite lines. The K hypersatellite lines result from the de-excitation of the double K vacancies. Another category comprises of single-photon two-electron rearrangement transitions, known as the Radiative Auger Effect (RAE) lines.

Figure 1.10 shows the photon-induced K X-ray spectrum of Zn recorded with a crystal spectrometer, which clearly shows the satellite, hypersatellite, and the RAE (Radiative Auger Effect – A broad weak X-ray emission structure with several maxima on the low-energy side of the characteristic X-ray lines which has been interpreted as a radiative $K \rightarrow L^2$ transition resulting in the simultaneous emission of a photon and an L-shell electron. Radiative

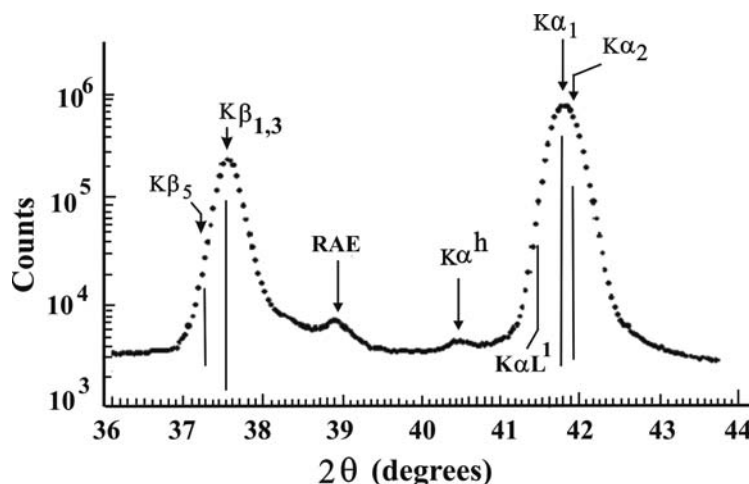


Fig. 1.10. Zn K X-ray spectrum excited by X-ray tube and recorded by a flat crystal spectrometer

Auger process is an intrinsic energy-loss process in an atom when a characteristic X-ray photon is emitted due to an atomic many-body effects) apart from the diagram lines $K\alpha_1$, $K\alpha_2$, $K\beta_1$, and $K\beta_2$ (Verma 2000).

Wavelength dispersive X-ray spectroscopy (WDS) may extend the threshold of detection by at least an order of magnitude as compared to the energy dispersive X-ray spectroscopy. Since the L X-ray spectra produced by heavier ions displays more complicated structure due to multiple vacancy production (Kageyama et al. 1996), WDS is must for analysis of such complex spectra. However, WDS requires optically flat, stable specimens and is limited to bulk analysis modes, limiting spatial resolution to more than $0.5\mu\text{m}$.

Energy Dispersive X-Ray Fluorescence

Figure 1.11 shows a schematic view of an energy dispersive XRF spectrometer. The basic components of an EDXRF spectrometer are X-ray source, sample, and the detector. Several devices such as source filters, secondary targets, collimators, and focussing optics are used to modify the shape or intensity of the source spectrum or the X-ray beam shape. Collimators (usually circular or a slit whose sizes range from approximately 10 microns to several millimeters) are used between the excitation source (X-ray tube or radioactive source) and the sample to restrict the size or shape of the source beam for exciting small areas. Filters (between the X-ray source and the sample or between sample and the detector) perform one of two functions: background reduction and improved fluorescence. The filter absorbs the low-energy X-rays (below the absorption edge energy of the filter element) while higher energy X-rays are transmitted. The advances in instrumentation/geometry for EDXRF has been

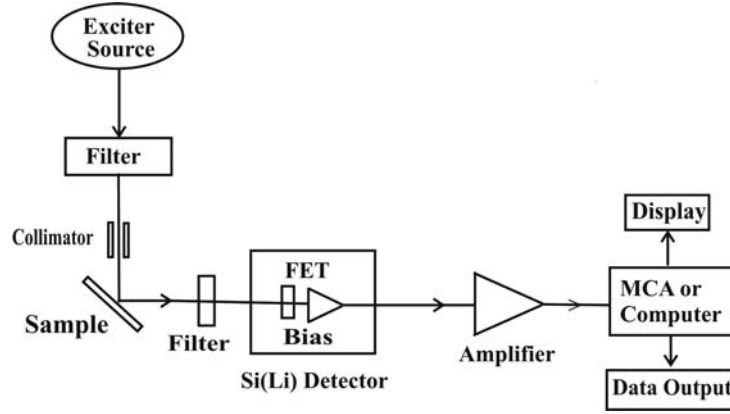


Fig. 1.11. Schematic view of a Si(Li) EDXRF spectrometer

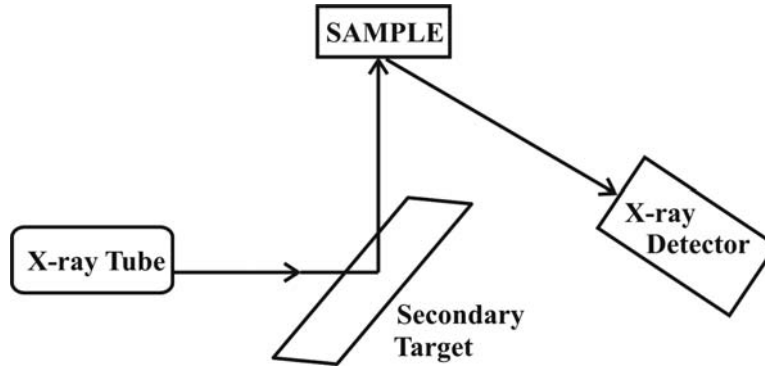


Fig. 1.12. Secondary source for X-ray fluorescence

discussed by a number of workers (Bisgård et al. 1981, Lal et al. 1987, Krishnan 1998, Bandhu et al. 2000, Romano et al. 2005).

To obtain a more monochromatic source peak with lower background than with filters, secondary sources are used. A secondary source can be produced by placing a target element between the X-ray tube and the sample, as shown in Fig. 1.12. The X-ray tube excites the secondary target and the Secondary target fluoresces and excites the sample. The detector as usual detects the X-rays from the sample. Because simple collimation blocks unwanted X-rays, it happens to be a highly inefficient method. Focusing optics like polycapillary devices (used in microbeam XRF) have been developed so that the beam could be redirected and focused on a small spot (less than 100 μm spot size).

The single crystal semiconductor Si(Li) X-ray detector known as semiconductor X-ray detector sorts the X-rays directly on the basis of their energy. X-rays enters the detector and ionize the silicon atoms producing electron-hole pairs in the deep intrinsic layer. An applied voltage (≈ 750 V) across the

crystal collects these electron-hole pairs. Since each ionization takes 3.81 eV of energy from the X-ray, the total (e-h) pair collected is:

$$Q = (E/3.81) \times 1.6 \times 10^{-10} \text{ Coulomb} \quad (1.11)$$

which is linearly proportional to E , the energy of the incident X-rays. This charge is integrated into a current pulse by a field effect transistor (FET) preamplifier and is subsequently amplified and converted to a voltage pulse. The original problem in fabricating semiconductor detectors was the insufficient thickness of the depletion zone. To obtain thickness greater than a few millimeters required very high resistivity, which could only be obtained with intrinsic materials. This problem of fabricating semiconductor detectors with depletion zone greater than a few millimeters was overcome by compensating the semiconductor material. The Si(Li) detector is basically a small crystal of silicon (Si), especially processed by lithium (Li) ions through the lattice to compensate for electrical impurities (p-type silicon is the starting material). When the Li-drifted crystal is provided with evaporated electrodes and cooled to liquid nitrogen temperature, it forms a low-leakage sensitive volume, which can be ionized by incident radiation. The high mobility and the low ionization energy (0.33 eV in Si) of *Li* impurity is primarily responsible for its choice as a compensator for p-type material in the preparation of NIP diode. Since *Li* is ionized at room temperature and has a small ionic radius (0.6 Å) compared to the lattice dimension of Si (5.42 Å), it is easily drifted through the lattice as an interstitial ion by the application of electric field.

The Si(Li) detector is enclosed in its own vacuum, isolated from the specimen chamber with a detector window, and maintained at liquid nitrogen temperatures with a cold finger and liquid nitrogen dewar (in order to decrease the number of electrons in the conduction band produced by thermal agitation, and thereby reduce “electronic noise”; decrease the noise from the FET-preamplifier; and prevent the diffusion of Li^+ which would be rapid at room temperature under the influence of the high potential across the crystal). The crystal itself is quite small – typically a wafer with an area of approximately 10 mm² and a thickness of 1 mm, since the X-rays have to pass through three layers before given the opportunity to generate its pulse within the intrinsic region of the detector. If the X-ray is not absorbed by the specimen, it may be absorbed by the detector window, which is typically 5–10 μm of beryllium or aluminum coated polypropylene. It might also be absorbed by the 200 Å gold conductive layer or the 1,000 Å dead layer on the detector surface. The gold is a component of the HV sandwich, and the *dead layer* is an inactive layer within the crystal, the thickness of which is attributable to the manufacturing procedure used to make the detector intrinsic and, to some degree, also attributable to the given detector and its age.

The overall efficiency of this system is much better than the WDXRF because of less restrictive solid angle losses and the diffraction losses. Although there is only a little absorption of low energy X-rays (since Z is so low for Be), the performance of the Si(Li) detector is limited at the low energy end

by absorption due to Beryllium window. Beryllium (Be) window is used since Be thin windows can be fabricated to be vacuum tight. This imposes a limit to $_{11}\text{Na}$ or $_9\text{F}$ as the lightest analyzable element with Be-window of 1 or 0.3 mil (1 mil = 0.001"). Windowless Si(Li) detector have been used to measure spectral peaks down to carbon but because the detector must be kept free from contamination, the use of windowless detectors can not be allowed under all conditions. The typical energy resolution for Si(Li) detector is ~ 160 eV for 5.9 keV X-rays. When a Si(Li) detector is used to collect X-ray photons with energies below 2 keV, the characteristic peaks in the spectrum show significant spectral distortion i.e., deviation from the ideal Gaussian shape observed for higher energy photons. This effect is due to incomplete collection of the charge deposited by the incident photon in the diode and can be as high as 30% for a line such as $\text{N K}\alpha$ at 400 eV.

The efficiency calibration of a Si(Li) detector at very low X-ray energies (below 3.3 keV) presents serious problems owing to a lack of practical radioactive standards in this energy region and to the discontinuity in the efficiency response caused by the K-absorption edge of silicon (at 1.84 keV). The solution lies in making theoretical efficiency calculations based on the detector parameters or measuring the efficiency by alternate experiment using secondary excitations from low- Z elements (Mg, Al, Si, etc.) taking the primary exciter as proton beam or radioactive source of known activity. While the secondary fluorescence method, for calculation of the efficiency of the detector, requires the precise X-ray production cross-section values for different target elements at the energy of bombardment, the theoretical calculations for efficiency values of the detector, at various energies, can be done according to the relation

$$\varepsilon(E) = \frac{\Omega}{4\pi} T(E) \times A(E) (1 - P_{\text{esc}}(E)) \quad (1.12)$$

where Ω is the solid angle subtended by the source on the detector and can be calculated using A/r^2 , where A is the active surface area of the Si(Li) detector and r is the distance of the detector from the X-ray source. In (1.12), P_{esc} is the escape probability while $T(E)$ and $A(E)$ are transmission factor and absorption factors, respectively, given by:

$$\begin{aligned} T(E) &= \exp(-\mu_{\text{Be}}(E) \times x_{\text{Be}} - \mu_{\text{Au}}(E) \times x_{\text{Au}} - \mu_{\text{Si}}(E) \times x_{\text{Si}}^d) \\ A(E) &= 1 - \exp(-\mu_{\text{Si}}(E) \times x_{\text{Si}}^s) \end{aligned} \quad (1.13)$$

The transmission factor $T(E)$ includes the transmission of photons through the Be-window of thickness x_{Be} , gold contact layer of thickness x_{Au} , Si dead-layer of thickness x_{Si}^d , and Si detector sensitive volume of thickness x_{Si}^s , respectively, while $A(E)$ is the absorption factor in the detector sensitive volume. The absorption coefficients are obtained from XCOM computer code (Berger and Hubbel 1987). The experimental efficiency curve for a Si(Li) detector using different radioactive sources along with one based on the theoretical calculations is shown in Fig. 1.13. Inset in the figure shows the efficiency below 3 keV

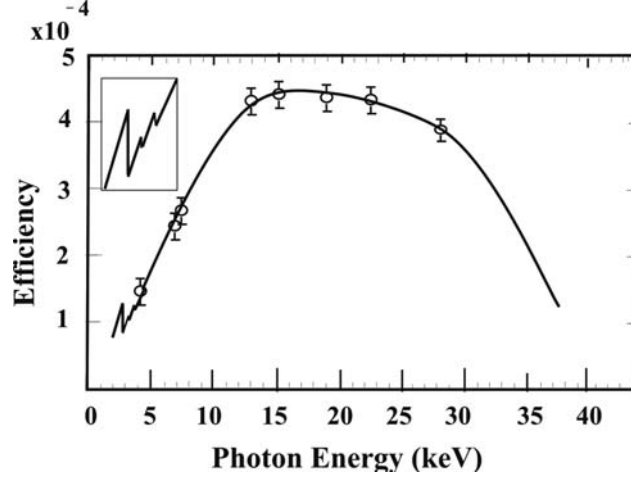


Fig. 1.13. Plot of the experimental (absolute) efficiency curve as a function of photon energy (keV) using ^{55}Fe , ^{57}Co , and ^{241}Am radioactive sources along with one based on the theoretical calculations. Inset shows the efficiency below 3 keV energy (on log energy scale)

energy (on log energy scale for better viewing). A sharp drop at 1.836 keV is due to the K-absorption edge of Si-dead layer and the jumps at the location of the Au M X-ray energies are due to the thin Au contact layer on the front of the diode. The efficiency drops at lower and higher energies are mainly due to the Be-window and Si-sensitive volume of the detector causing absorption of low-energy and high-energy X-rays, respectively, since the absorption and transmission processes are a function of energy due to dependence of absorption coefficient $\mu(E)$ on energy E of the incident X-rays. This relationship determines both how deep a detector needs to be to stop the incident X-rays and the reduction in efficiency due to the window thickness and crystal dead layer thickness.

The efficiency calibration of a Si(Li) detector in the energy range of 5–60 keV using radioactive sources has been reported by Verma (1985). A modified theoretical model for calculating the efficiency of a Si(Li) detector has been presented by Garg et al. (1987) while the comparison of experimental efficiencies for different Si(Li) detectors in the energy range, 4.5–17.5 keV has been made by Yap et al. (1987). Table 1.7 lists the radioactive sources for efficiency calibration of the Si(Li) detector.

The Si(Li) detector has an intrinsic resolution i.e., FWHM (full width at half-maximum) given by the relation

$$\text{FWHM} = 2.35(\varepsilon F E_{\gamma})^{1/2} \quad (1.14)$$

where $\varepsilon = 3.81 \text{ eV/pair}$; F (Fano factor i.e., ratio of statistical variance to the yield) = 0.12, and E_{γ} = photon energy. Thus at 1 keV, the intrinsic resolution is approximately 52 eV and at 10 keV, it is about 162 eV.

Table 1.7. The radioactive sources for energy and efficiency calibration of the Si(Li) detector (Ref. IAEA chart of the Nuclides)

Source	Half-life	Transition Energy (KeV)		Transition Intensity (%)
Mn ⁵⁴	312.1 days	5.406	(K α_2 of Cr)	7.43
		5.415	(K α_1 of Cr)	14.70
		5.95	(K β of Cr)	2.95
Fe ⁵⁵	2.73 yr.	5.888	(K α_2 of Mn)	8.24
		5.899	(K α_1 of Mn)	16.28
		6.49	(K β of Mn)	3.29
Co ⁵⁷	270.5 days	6.391	(K α_2 of Fe)	16.8
		6.404	(K α_1 of Mn)	33.11
		7.06	(K β of Fe)	6.68
		14.4	(γ)	9.16
Zn ⁶⁵	244.3 days	8.028	(K α_2 of Cu)	11.51
		8.048	(K α_1 of Cu)	22.60
		8.91	(K β of Cu)	4.61
Sr ⁸⁵	64.8 days	13.336	(K α_2 of Rb)	17.11
		13.395	(K α_1 of Rb)	33.01
		15.0	(K β of Rb)	8.70
Y ⁸⁸	106.6 days	14.098	(K α_2 of Sr)	17.46
		14.165	(K α_1 of Sr)	33.69
		15.80	(K β of Sr)	9.05
Am ²⁴¹	432.2 yr.	3.35	(Np M)	6.35
		11.89	(Np L1)	0.85
		13.94	(Np L α)	13.0
		17.8	(Np L β)	19.3
		20.8	(Np L γ)	4.93
		26.345	(γ)	2.4
		33.119	(γ)	0.103
		43.463	(γ)	0.057
		59.537	(γ)	35.7

There is a statistical probability that some of the X-rays, generated in the sample and impacting the Si(Li) detector will “inadvertently” knock out Si K-shell electrons in the detector, reducing that X-ray’s energy measured in the detector by the Si absorption edge energy (1.84 keV). Let us consider that we have a sample with lots of Fe (K α of 6.40 keV); the Si-escape peak of FeK α will appear at 4.56 keV. This escape peak is only seen for the major elements present in the sample. The ratio of escape peak and exciting primary radiation (parent + escape) intensity in a Si(Li) detector is given by

$$\begin{aligned}
\eta &= I_{\text{esc}} / (I_{\text{parent}} + I_{\text{esc}}) \\
&= \frac{\omega_k}{2} \times \frac{\tau_K}{2} \frac{\tau_K}{\mu_p} \left[1 - \frac{\mu_s}{\mu_p} \ln \left(1 + \frac{\mu_p}{\mu_s} \right) \right]
\end{aligned} \tag{1.15}$$

where μ_p and μ_s are the mass attenuation coefficients for the primary (p) and secondary (s) radiation. Each primary X-ray line comprises a Lorentzian energy distribution that is convoluted with overall detector response function which comprises a Gaussian line shape, an exponential tail, a flat shelf (including a step at 1.75 keV) and an enhanced shelf region between a peak and its escape peak.

In an energy dispersive spectrometer, the interference from the X-ray lines of the trace element with the analyte element significantly degrades the detection limits particularly when the interfering peak is from an element of major consideration. Even though the intense peak may not overlap the trace element peak, it can increase the background for the small peak if the major peak has a higher energy.

Since Si(Li) detectors require liquid nitrogen cooling to provide acceptable resolution, further refinements in detector technology have led to the introduction of alternative detector (Sokolov et al. 2004) types including Si(PIN) detectors (which do not require cryogenic cooling – the thermoelectric cooler cools both the silicon detector and the input FET transistor to the charge sensitive preamplifier), Si-drift detectors (expensive, but with a very high count rate capability), and various semiconductor materials of higher atomic number (Ge, CdZnTe, HgI₂) that can extend the detector efficiency beyond the 20 keV limit typical of Si(Li) detectors. The use of HgI₂ crystal is advantageous because of the high atomic number of the elemental components and the large band gap (2.1 eV) associated with electronic transitions. However, while the ionization efficiency for the Si(Li) detector is 3.8 eV per electron-hole pair formed, it is 4.2 eV for HgI₂ resulting in a lower charge collection and a poorer energy resolution for the HgI₂ detector. The tentative value of 175 eV (FWHM) for the MnK α photopeak has been obtained with the preamplifier input FET cooled by liquid nitrogen and HgI₂ at room temperature. The difficulties in reliably producing detector crystal, dramatical decrease of the energy resolution with increasing count rate and relatively fast degradation of their performance, are the hampering factors in the commercial availability of these detectors. HPGe, the high-purity Ge-detectors (Low energy photon spectrometers) can be used in the X-ray region and in energy extended to about 1 MeV, but Ge has a more pronounced efficiency change about its K-absorption edge (at ~ 11 keV) than does Si (at 1.75 keV). So Silicon makes a better-behaved detector. Since ^{32}Ge has a higher atomic number than ^{14}Si , therefore the problem with entrance window and dead layers are more severe with Ge-detectors than with Silicon detectors.

The Si(Li) begins to lose efficiency at higher X-ray energies. Practically a millimeter thick detector has only about 15% efficiency at 50 keV, and efficiency falls rapidly above that energy. Thus Si(Li) detector covers energies in the range of ~ 40 keV. The lower energies are limited by the beryllium entrance window (~ 0.5 mil thickness). However, the intrinsic Ge detector with less than 0.1 μm Ge of dead layer and 5 mil of thin Be-window gives good efficiency at higher energies up to 100 keV. In GAMMA-X detectors

manufactured by ORTEC, the $0.3\text{ }\mu\text{m}$ boron ion-implanted contact and thin beryllium front window allows photons of energy down to 3 keV to enter the active volume of the detector. Except for the anomaly at the 11-keV germanium absorption edge, virtually all photons up to 200 keV are detected. Above that energy, the efficiency falls off with the total absorption cross-section of Ge, which is dominated by the fall-off in the photoelectric cross-section.

A gas (usually 90%Ar + 10%CH₄) filled proportional counter is an alternative ED detector (except at short wavelengths where a Xe sealed proportional counter is preferred) particularly in industrial applications. This detector provides resistance to vibrations, mechanical reliability, and minimal temperature dependency. A proper choice of the filling gas of proportional counter is of great importance in minimizing the background caused by the wall effect. Although the resolution of this detector is relatively very poor, the detection limit in the ppm range can be obtained.

Whenever the wavelength of the characteristic X-ray used for analysis (region of interest) is near to or coincides with the characteristic X-ray lines of one or more matrix elements, spectral interferences (also called peak overlaps) occur, which can be a serious source of error in quantitative microanalysis. For example, K-lines of adjacent elements like ¹³Al and ¹⁴Si, ¹⁶S and ¹⁷Cl, ¹⁹K and ²⁰Ca, etc. overlap. Similarly K-line of ¹⁶S overlap with L-line of ⁴²Mo, K line of ¹⁷Cl overlap with L-line of ⁴⁵Rh, K-line of ³³As overlap with L-line of ⁸²Pb. The extent of overlap is determined by the resolution of the detector. To tackle such a problem, Schreiner and Jenkins (1979) have given an off-line nonlinear least squares fitting procedure as part of "RUNFIT" software which supports most of the intensity/correction algorithms currently employed in X-ray fluorescence spectrometry. Donovan et al. (1993) have given an improved algorithm for the quantitative treatment of interference corrections in wavelength-dispersive X-ray spectrometry analysis.

With energy-dispersive X-ray analysis data, *Imaging of different elements* can be done to locate the distribution of elements since the composition varies with position across an image area. In mapping, it would be ideal if the entire EDS spectrum could be saved at every picture element so that the same full spectrum procedures could be followed (Myklebust et al. 1989; Ingram et al. 1998). Mapping control software usually allows placing windows across each characteristic peak of interest and defining two or more background windows. Representative methods of analysis include (1) line scans of relative element concentrations along a scanned line passing through a selected object, (2) presence/absence analysis (dot mapping) at a specific X-ray energy level to detect a specific element, or (3) cumulative computer maps that can image up to 15 low resolution maps of different elements at the same time and can recursively collect data until the required resolution is obtained. The mapping collection software of Newbury and Bright (1999) allows definition of windows for several characteristic peaks of interest and five background windows. The latter are placed above and below each characteristic peak window. First-order background corrections are then made by simple linear interpolation with the

background windows closest in energy to, and to either side of the peak of interest. When minor or trace peaks are to be mapped, background windows are assigned as close as possible to the characteristic peak location. For X-ray imaging simulation in the field of biomedicine, Lazos et al. (2003) has described a software simulation package of the entire X-ray projection radiography process including beam generation, absorber structure and composition, irradiation set-up, radiation transport through the absorbing medium, image formation, and dose calculation.

Some manufacturers of EDXRF spectrometers (e.g., Horiba, Jorden Valley, Rigaku, Shimadzu Scientific Instruments, Oxford Instruments, etc.) have developed X-ray analytical microscopes for imaging which include CCD camera, focused X-Ray system, and a vacuum Fluorescent X-Ray probe. These spectrometers allow measurements on spot sizes as small as 10 microns on samples as small as 512 microns square or up to 100 mm square. These spectrometers are being used in fields as diverse as electronics, medicine, food, cosmetics, life science, plastics and alloy analysis, provide elemental mapping of a number of elements simultaneously in a wide variety of sample types.

Longoni et al. (2004) have designed an X-ray fluorescence spectrometer (for elemental mapping applications) based on a ring-shaped monolithic array of silicon drift detectors (SDDs) with a hole in the center. The coaxial X-ray excitation beam, focused by a polycapillary X-ray lens, reaches the sample after passing through the central hole. This geometry optimizes the useful solid angle for collecting the fluorescence from the sample, while the optics maximizes the photon density in the excitation spot. These features, together with the very high detection rate of SDDs, allow a high scanning rate in elemental mapping to be achieved. Moreover, the spectroscopic resolution of SDDs (cooled by thermoelectric Peltier elements) is comparable to that of the classical Si(Li) liquid nitrogen-cooled detectors. The authors have given several examples of applications of the novel spectrometer in various fields from archeology to biology.

1.4.3 Source of Excitation and X-ray Detection in PIXE Analysis

The PIXE technique is similar to EDXRF (described in “Energy Dispersive X-ray Fluorescence (EDXRF)”) except that the exciter source in this case is beam of proton, α -particles, or heavy ions of $1\text{--}3\text{ MeV amu}^{-1}$. Although the ions of energy less or greater than the range specified earlier can also be used but the yield of X-rays will relatively decrease as the X-ray yield (cross-section) depends on the energy of the projectile. The energy of the proton beam in PIXE is $\approx 3\text{ MeV}$ because the X-ray production has maximum cross-section at $\approx 3\text{ MeV}$. The charged particles obtainable from particle accelerator (Pelletron, cyclotron, Van de Graaff accelerator), lose energy while traversing through sample material. In the energy range under consideration, the energy loss is mainly due to the interaction of those particles with the electrons in the material causing excitation and ionization. Thus the principle of PIXE

technique consists of ionizing the atomic levels using the charged particles. This ionization is followed by a rearrangement of the electronic architecture with emission of characteristic X-rays. The detection of this radiation is realized by Si(Li) or intrinsic Ge semiconductor detectors. The characteristics of the PIXE technique are (1) nondestructiveness (2) rapidity (± 15 min) (3) easy preparation of the sample, and (4) determination of most of elements with $Z > 13$ with a good sensibility (ppm or sub ppm) and with a good confidence.

In the early 1970s, applied nuclear physicists quickly appreciated the beautiful match of particle-induced X-ray emission (PIXE) analysis to air particulate pollution sampling. Because X-rays from elements $Z \leq 13$ are strongly absorbed in typical target and any layers intervening between the target and the depleted region of the detector, it is practically impossible to analyze elements with $Z \leq 13$. For analysis of light elements below $Z = 13$, the other accelerator-based techniques like Rutherford Backscattering (RBS) – discussed in Chap. 2, Elastic Recoil detection Analysis (ERDA) – discussed in Chap. 3, Nuclear Reaction Analysis (NRA) – discussed in Chap. 7, are used as complementary techniques to PIXE analysis.

Significant changes have occurred in the past two decades especially in the use of focused ion beams in PIXE microprobes, milliprobes, and external beam systems. An important advantage of the external beam (i.e., beam brought into the atmosphere through a thin exit foil) is the possibility of analyzing volatile materials. An additional advantage of an external beam is that heat dissipation from the surface of the sample is effective and samples may be cooled easily.

The beam of charged particles can be obtained from single ended Van de Graaff or Tandem accelerator (Pelletron) or cyclotron. Figure 1.14 shows the typical diagram of a 3 MV Van de Graaff Tandem accelerator (Pelletron) to procure the beam of charged particles.

The Pelletron accelerator is basically a charged particle accelerator very similar to the Van de Graaff. In a Pelletron accelerator the charging belt used in a conventional Van de Graaff, has been replaced by a more stable and dependable rugged chain, consisting of metal cylinders, called pellets, joined by links of solid insulating plastic. The gap between the metal cylinders, serve as a spark gap providing excellent protection to the insulating links. Pelletron is essentially a two stage (tandem) electrostatic accelerator, in which the singly charged negative ions of the required projectile element, produced in the ion source, are directed to the low energy “accelerator tube” in which the metal electrodes, uniformly graded in electric potential and electrically insulated from each other, are suitably spaced. The charged particles are then accelerated toward an electrode called “terminal,” maintained at a very high positive DC potential. In the terminal, the accelerated negative ions obtained from the ion source are stripped off by one or more electrons, during the collision of the negative ions with the atoms of the gaseous or solid targets (usually carbon foils are used as strippers). These multiply charged positive

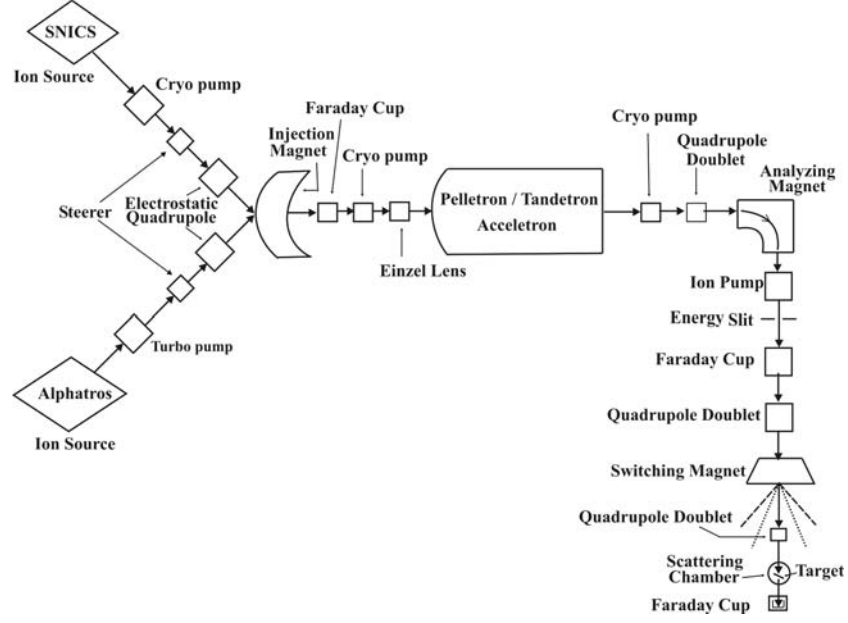


Fig. 1.14. A Pelletron accelerator to procure the beam of charged particles

ions (charge state q^+) are then accelerated again as they pass through the high-energy accelerator tube. The kinetic energy attained by the ions emerging from the tandem pelletron accelerator is thus given by:

$$E = V(1 + q) \text{ MeV} + \text{Injection energy}$$

where V is the terminal voltage in MV.

The high DC voltage on the terminal is produced by transferring to it a steady current of positive ions. The main parts of the accelerator are:

Ion Sources

The negative ion beams from the ion source are injected into the pelletron accelerator at an energy of about 100 keV by the injector system. The two negative ion-sources are as given below:

Duoplasmatron

Duoplasmatron is a two stage gaseous arc discharge source. The first stage is maintained at relatively high pressure (3×10^{-2} Torr) and low voltage (typically 20 V) between a thermionic cathode and an intermediate electrode, acting as primary anode. The plasma produced in the first stage is guided by a strong axial magnetic field through an aperture within the intermediate electrode to the second discharge chamber maintained at lower pressure

(2×10^{-3} Torr) and higher voltage (typically 80 V). The plasma created in the second stage flows out through a small aperture in the anode and expands into the third chamber called “expansion cup.” In a duoplasmatron, the plasma is compressed by a nonuniform magnetic field. The magnetic field confines the electrons so as to limit intense ionization to a small region around the anode aperture. The power in this intense discharge is dissipated as heat by anode structure fabricated from a high melting point and low vapor pressure material like molybdenum. The outer anode and the intermediate electrode are made from magnetic material. The ion beam current density of the order of 10^{-2} – 1 A cm^{-2} can be attained with a duoplasmatron.

SNICS (Source of Negative Ions by Cesium Sputtering)

In this ion source the cesium atoms used to cause sputtering, are ionized in an inert-gas discharge. The cathode containing a small amount of the material whose beam is to be produced, is inserted in the chamber through the air lock. The ionized cesium then sputters the solid cathode material to produce negative ions. This ion-source is used to produce the negative ions of almost all the solid materials.

Injection of Negative Ions in the Main Accelerator

The negative ions from the ion sources are first preaccelerated and then guided to the accelerator entrance by “injector magnet”. The Einzel lens assembly preaccelerates the negative ions from the ion source and focuses the beam on to the image slit through the injector magnet.

The injector magnet is 90° dipole magnet. It separates the particular ion from flux of ions coming from the ion-source. The injector magnet focuses the ion beam on to the slit through the beam profile monitor. A slit and a Faraday cup are provided just behind the injector magnet to separate the unwanted ions and to measure the beam flux to be injected into the accelerator.

A beam profile monitor (BPM) is provided before the slit. It provides the continuous display of the shape and position of the beam in both the X - and Y -coordinates. In BPM, a helical wire on a rotatory drive crosses the beam vertically and then horizontally during each revolution. A cylindrical collector around the grounded wire collects beam-induced secondary electrons from the wire to provide a signal proportional to the intercepted beam at that instant.

Main Accelerator Tube

The main accelerator consists of a number of accelerating columns on each side of the terminal. Each column consist of a pair of hollow circular aluminum casting supported by ceramic insulators.

The central part of the tube is the high-voltage terminal. It is spherical in shape and charged by motor driven chains consisting of metallic pellets

insulated by nylon studs. The charge is induced onto the chain by induction electrodes at the base of the tank. This charge is then deposited on the terminal, thereby raising its potential. The high potential terminal is supported by insulating columns consisting of two insulating plates. Hoops are used along the insulating plates to maintain equipotential planes. The ions passing through the terminal are made to pass through the stripper (gas or a thin carbon foil) which changes the negative ions into positive ions. The positive ions are further accelerated in the accelerator column raising the energy of the beam to $(1 + q)$ V. When the accelerator is to be used to produce low-energy beam, shorting rod system is used. Shorting rod system consists of stainless steel and/or nylon rods provided at either end of the tank to be introduced into the column to electrically short the selected columns as and when required. This system is very useful during tube conditioning, operation at low voltage or trouble shooting in the column.

For the stabilization of beam energy, the terminal voltage is stabilized by a feedback system. The feed back signal taken from the capacitive pickoff plate, on the control slit, after the analyzing switching magnet, is combined with the absolute voltage signal. The signals are used to control the biased corona needles pointing at the high-voltage terminal.

The beam coming out of the stripper foil with different charge states passes through a quadrupole lens to select a particular charge state. The entire accelerator column, including the charging system and accelerator tube, is enclosed within a pressure vessel filled with SF_6 gas at a pressure of ~ 100 psi. The SF_6 is chosen because of its excellent dielectric strength.

Analyzing Magnet

The accelerated beam coming out of the accelerator is focused on to the analyzing magnet. The quadrupole lens, provided at the outlet of the accelerator, focuses the accelerated ion beam on the analyzing magnet through the beam profile monitor, slit, and Faraday cup. The analyzing magnet analyzes the ions of particular mass and energy. In vertical type of accelerators, the analyzing magnet also bends the vertical beam into horizontal plane.

Switching Magnet and Beam Steerers

Since it is not possible to perform all the accelerator related experiments at a single port, a number of ports have to be provided to the accelerated ion-beam obtained from the accelerator. This task is accomplished by the switching magnet which is a quadrupole magnet. It not only directs the beam to different ports maintained at $\pm 15^\circ$, $\pm 30^\circ$, and $\pm 45^\circ$ to the main beam line, but also analyzes the ion-beam for its mass and energy.

Although the switching magnet directs the beam into a particular port, yet it may need minor adjustment in the horizontal and vertical direction.

This minor adjustment of the beam in the horizontal and vertical direction is done with the help of electrostatic beam steerers.

To minimize the transmission losses of the ion beam and its proper focusing, a number of beam steerers, quadrupole lenses, Faraday cups, and beam profile monitors are used throughout the low and high energy beam transportation system. Since in a heavy ion accelerator, charge exchange or scattering collisions can cause energy loss and spread of the ion beam, a number of vacuum pumps are used to provide clean and ultrahigh vacuum conditions for the passage of ion beams.

The beam current on the target ranges from 1 to 100 nA. Smaller beam currents are required due to the consideration of count rate, spectra energy resolution as well as to avoid the target destruction due to excessive heating/burning. The intensity of the proton beam may be measured directly on the target when the electrical conductivity of the sample is sufficient. For insulators (that can not be reduced to a powder in which a conducting ligand is added) regularly rotating index shutting off part of the incident proton beam is used as a monitor.

Scattering Chamber, Target Holder, and Samples

Scattering chamber encloses the evacuated ($<10^{-6}$ Torr) area where the ion beam strikes the target. It is made up of steel provided with windows/ports and is connected to the beam line by means of a gate valve so that the vacuum in the beam line and the scattering chamber could be maintained separately. The base of the chamber is calibrated to measure the angle between the target and the ion beam. The targets are usually placed at 45° to the beam direction. A Faraday cup is housed behind the target at the end of the chamber window. The thin targets are mounted on the target ladder placed at the centre of the chamber. The target ladder can be maneuvered vertically and about its axis externally. The surface barrier detectors, needed to yield information about the scattered charged particles are also arranged inside the chamber in the forward or in the backward direction. The Si(Li) detector is placed at 90° to the beam direction to collect the characteristic X-rays of the target. Since the X-rays are detected by the Si(Li) detector, the chamber is so designed that by using a flange, the neck of the detector can be inserted the flange so that the distance from the target is decreased. Angular positions are provided at the base of the chamber for accurate positioning of the SBD detector, which is used for charged particle detection (for normalization). Figure 1.15 shows the target chamber for PIXE analysis.

Since the target chamber in PIXE analysis is highly evacuated ($\sim 10^{-6}$ Torr), it is preferable to prepare a rotating target holder on which many different samples can be loaded at any time and one must be in a position to place a particular target facing the beam by maneuvering the target holder from outside manually or through remote control. It is necessary so that it may not be required to vent the vacuum chamber after each sample

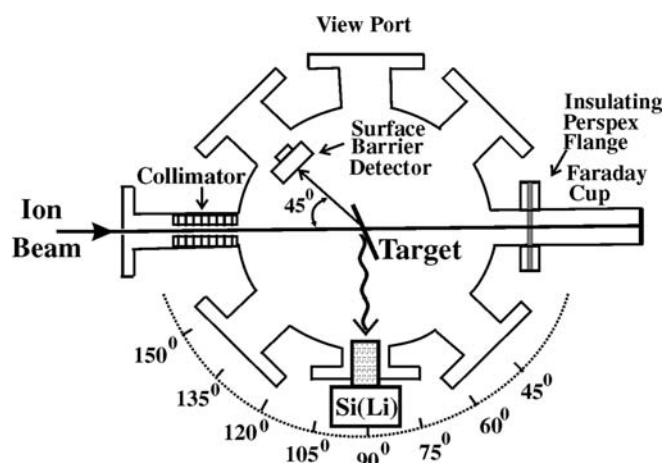


Fig. 1.15. Target chamber for PIXE analysis

run. The target holder assembly usually is a ladder type made of stainless steel with equidistant holes in it. The position of the target can be well determined from the position of a pointer attached to the target holder shaft from outside which slides over a vertically fixed scale. The ladder could also be manually rotated from outside in order to orient the targets at the desired angle with respect to the beam direction.

The samples in PIXE analyses are usually self-supporting or are sputtered or coated on a thin-foil or on a thick backing containing no detectable amount of the element of interest. Most samples are analyzed in their original state; aerosol filter, archaeological samples, soil, biological samples, etc. However, as PIXE technique is probing only top 10–50 μm of the sample (depending on the material, energy of incident beam and most importantly on the energy of characteristic X-rays), it is very important that the area/volume irradiated by the beam (usually a circular area with the diameter of 1–10 mm) is representative of the whole sample. Therefore, if the sample is obviously not homogeneous, like for example some pottery and geological samples, the sample should be grinded to a fine powder (preferably with particle size smaller than 1–2 μm), thoroughly mix it with 20% analytical grade carbon powder and consequently press into pellets.

Detection System

In PIXE analysis, the X-rays are detected by a Si(Li) energy dispersive system that includes a pre-amplifier (to optimize the coupling of the detector output to the amplifier) and an amplifier (to amplify the signal after shaping the pulses). The analog signal from the amplifier is fed into an analog to digital converter (ADC), which is then transferred into the memory of the on-line

computer via a CAMAC interface. The X-ray spectrum can be viewed on multichannel analyzer (MCA) terminal and the analysis can be carried out using the computer.

The $K\alpha$, $K\beta$ (or/and their components) lines of various elements as seen from the spectrum are compared with the standard X-ray fluorescence lines from the table. The net counts in different regions of interests (ROIs) including different peaks are calculated after subtracting the background. In other words, the linear or quadratic background can be fitted to an MCA spectrum which needs to be subtracted to calculate the net area under the peak. The background counts are calculated by averaging the counts on rather flat portion of the peak, taking the same number of channels on both side of the peak.

For analysis of a complex spectrum (containing many overlapping peaks) using multichannel analyzer, the three parameters i.e., energy (E), resolution i.e., full-width at half maximum (FWHM) and the area, have to be adjusted with certain constraints. It may not be possible to adjust all the three adjustable parameters simultaneously during the fit. For example, in spectrum analysis the energy of the known peaks should not be optimized as the peaks may appear at slightly different energy due to multiple ionization (explained in Sect. 1.4.4). However, the overall energy calibration coefficients for the entire spectrum, which relate channel number to energy, might well be optimized during the fit. Similarly, the FWHM of the detected X-ray peaks are not independent, but rather typically follow a predictable detector response function:

$$\text{FWHM} = A + B^* \sqrt{E}$$

Finally, even the amplitude of an XRF peak might not be a free parameter, since, for example one might want to constrain the $K\beta$ peak to be a fixed fraction of the $K\alpha$. Such constraints allow one to fit overlapping $K\alpha/K\beta$ peaks with much better accuracy.

The analysis can also be carried out using the standard computer code. However, the procedure for analysis is the same as described earlier. PIXEF (for PIXE-fit): the Livermore PIXE spectrum analysis package has been developed by Antolak and Bench (1994). This software initially computes an approximation to the background continuum, subtracts from the raw spectral data and the resulting X-ray peaks are then fitted to either Gaussian or Hypermet distributions. The energy dependent ionization cross-sections for each element's K-shell or L-subshell are procured from the analytical functional fit, while the subshell and total photoelectric cross-sections are determined directly from the Dirac-Hartree-Slater calculations of Scofield. Schematic of a typical PIXE spectrum is as shown in Fig. 1.16.

The main trend in PIXE analysis had also been on the development and extensive application of proton microprobe (beam diameter \cong micrometer) as it offers better spatial resolution, generates a far lower background resulting in better detection ability.

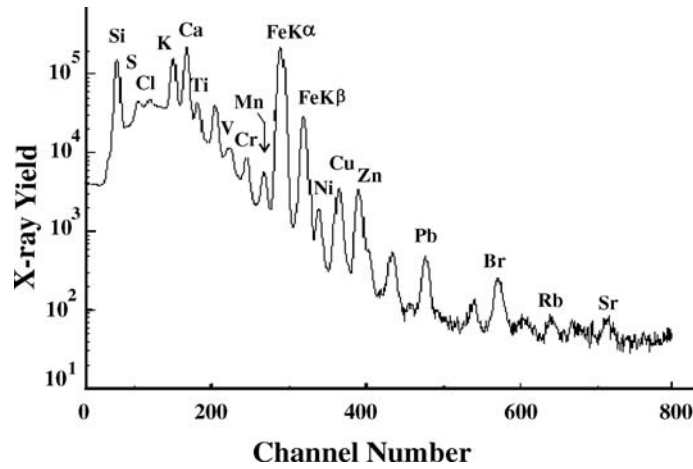


Fig. 1.16. A typical PIXE spectrum. The names of the elements over the peaks in the spectrum refer to the X-ray lines of those elements

1.4.4 Some Other Aspects Connected with PIXE Analysis

Choice of Beam/PIXE Using Heavy Ion Beams

PIXE work is normally carried out with protons of 2–3 MeV. Two aspects are important for consideration i.e., (a) PIXE using low energy protons (<1 MeV) and (b) PIXE using heavy charged particles/ ions like deuterons, α -particles and heavy ions like $^3\text{He}^+$, $^3\text{He}^{2+}$, C^+ , N^+ , O^+ , Ne^+ , etc.

Since the PIXE analysis is based on two fundamental quantities i.e., the interaction of the charged particles with the sample material (stopping) and the X-ray production cross-sections, the electronic stopping cross-sections reach their maximum value and the X-ray production cross-sections are subject to steep variation in the low energy range of the projectile. The energy dependence of the X-ray production cross-section must be accurately known to achieve reliable results during the analysis. A few workers like Paul and Muhr (1986), Paul and Sacher (1989), Paul and Bolik (1993), Orlic (1989), and Cohen (1990) have given the values for K and L X-ray production cross-sections with protons and α -particles.

The advantage of low energy PIXE are as follows (1) the minimum detectable limits are shifted toward lighter elements, (2) the ratio of secondary to primary radiation decreases, and (3) the small ranges and low X-ray yields of protons below 1 MeV restrict the analyzed layer to a few μm (or mg cm^{-2}) on the surface of the target. The limitation of low energy PIXE is the decrease of sensitivity (by one or two orders of magnitude) due to low X-ray production. This is reflected in longer counting times and the possibility of target damage because of higher amount of accumulated charge (Miranda 1996).

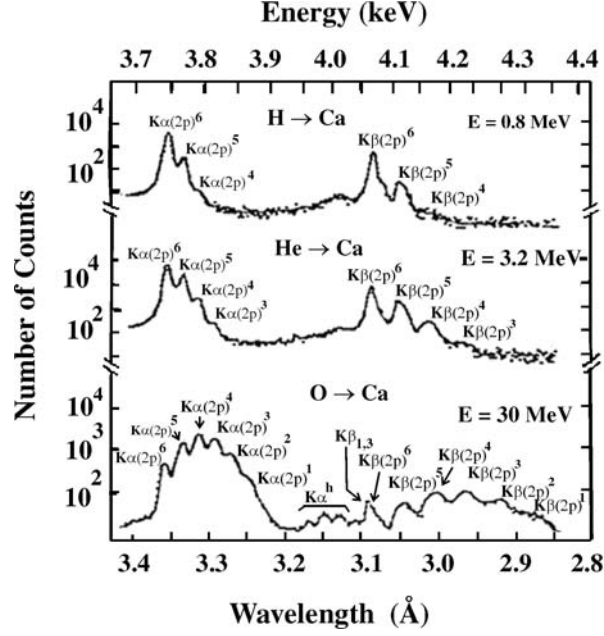


Fig. 1.17. Multiple ionization caused due to the bombardment of heavy ions (spectrum of satellite lines along with the diagram lines)

If heavy ions are used for bombardment in PIXE studies, a more complex spectrum (Fig. 1.17) is caused because of the following two reasons – first, the projectile has a greater mass and charge and would therefore be expected to exert a more disruptive effect on the target atom; and secondly, the projectile has an electronic level structure of its own, causing multiple ionization i.e., that one or more L electrons are ejected simultaneously with a K shell electron or double K ionization takes place. Due to appearance of the new set of lines (satellite and hyper-satellite), the principle X-ray lines get broadened and shifted to the higher energy side when observed by a Si(Li) detector. However, the complexity of the spectrum is very much visible when observed through a crystal spectrometer (energy resolution $\approx 1\text{--}2\text{ eV}$). The K α satellite lines will be represented as K $\alpha(2p)^5$, K $\alpha(2p)^4$, K $\alpha(2p)^3$, ... meaning that 5, 4, 3, ... electrons remain intact in the 2p shell while K $\alpha(2p)^6$ will represent the K α principle line with all the six 2p electrons intact. Similar terminology is also used for K β satellite lines.

The PIXE method using 30 MeV α -particles, has been applied for the elemental analysis of metal targets by Bauer et al. (1978) who have reported the advantage of better accuracy and deep penetration ($\sim 100\text{ }\mu\text{m}$) of α -particles into the sample. The K α X-ray yield of thick targets for alpha particles ranging from 1 to 100 MeV was reported by Castiglioni et al. (1992). The heavy ions such as C^+ , N^+ , O^+ , and Ne^+ are not very suitable for PIXE studies mainly because the cross-sections for X-ray production are too small (not

proportional to Z_1^2) to produce appreciable yields. Moreover, the PIXE work using heavy ions is not yet well established as only a few measurements on the K and L X-ray production cross-sections, in different selected elements, with various selected projectiles, are available (Mokler et al. 1970, Datz et al. 1971, Mukoyama et al. 1980, O'Kelley et al. 1984, Andrews et al. 1985, Tanis et al. 1985, Mehta et al. 1993, Wang et al. 1993, Tribedi et al. 1993, 1994, Goyal et al. 1995, Semaniak et al. 1995, Padhi et al. 1996, Baraich et al. 1997, Bogdanovic et al. 1997). The experimental values for K X-ray cross-sections indicate that the cross-sections increase more than predicted by the ECPSSR theory of Brandt and Lapicki (1979, 1981). Due to variation in the ion-beam energy of heavy-ions, the X-ray lines shift to higher energies (and Auger lines to lower energies) as more energetic projectiles produce more vacancies in the valence shell in addition to the inner-shell vacancy, called the multiple ionization. Since the observation of broad and poorly resolved peaks consisting of many satellite lines with little of the diagram lines (Fig. 1.17) indicates that it has been caused by multiple ionization. Based on the energy shift of the diagram lines and change in the intensity of the transitions, the modified values of the fluorescence yields (ω_K) have been derived. The modified values happen to be as much as 40% larger than the single-vacancy fluorescence yield values. Reasonable agreement with the ECPSSR theory is obtained for $^{17}\text{Cl} + ^{35}\text{Br}$ where $Z_1/Z_2 \sim 0.5$ (regime of MO theory) with the agreement becoming progressively worse, for $Z_1/Z_2 \rightarrow 1$ (Tanis et al. 1985). Thus the precise values for X-ray cross-sections for various projectiles, based on any theoretical approach, are not available.

A few important formulae relating to heavy-ion induced PIXE are given later:

1. The cross-section for ionization of the n th shell

$$\sigma_n = 8\pi a_0^2 \frac{Z_1^2 f_n}{Z_2^4 \eta_n} \quad (1.16)$$

where Z_1 is the incident particle charge, Z_2 the effective target nuclear charge, a_0 is the Bohr radius, η_n depends on the incident energy, and f_n is a quantity related to the electronic wave function.

2. Charged particle Bremsstrahlung is proportional to $(Z_1/M_1)^2$, is small for heavy projectiles.
3. Maximum of the cross-section ($\propto Z_1^2$) occurs at an energy proportional to square of the projectile charge.

Although the X-ray production cross-sections are function of the incident beam energy and increase with increase of energy (σ_x depends only on the projectile velocity and not its mass) yet the beam energy of 2 to 3 MeV u^{-1} is preferred. The limiting value on the higher energy side is important due to the reason that the energy of the beam should be less than the Coulomb barrier so that the nuclear reaction are not caused to produce γ -radiations and increase the background. The target atomic number (Z_2)-value for which

Table 1.8. The Atomic number of the target element for which the Coulomb barrier equals the Centre of Mass (CM) beam energy

Energy (MeV u ⁻¹)	Target Atomic Number (Z_2) – Values For				
	Protons	Deuterons	α	${}^3\text{He}^+$	${}^3\text{He}^{2+}$
2	6	18	18	34	13
3	11	33	33	60	22
4	23	70	70		76

the Coulomb barrier equals the CM beam energy is given in Table 1.8, which has been calculated using (1.5).

This means that for a target material with a Z_2 -value lower than those given in Table 1.8, the projectile is able to penetrate into the nucleus and produce γ -rays through nuclear reactions. Thus with protons of 3 MeV, we cannot detect trace elements having $Z < 11$. Although it is theoretically possible to detect elements with $Z > 6$ using protons of 2 MeV yet we can not detect the elements like C, N, etc. due to the limitation caused by the Si(Li) detector (The low energy X-rays of elements with $Z < 11$ are absorbed in the window of the detector). The choice of protons of 3 MeV energy is thus appropriate.

The choice between protons, deuterons, and α -particles depends on the following factors:

- Variation of cross-sections for these heavy atomic ions vis-à-vis protons

$$\sigma_{Z_1, M_1}(E_1) = Z_1^2 \times \sigma_{1,1} \left(\frac{E_1}{M} \right) \exp \left[\sum_{i=0}^4 a_i Z_1^i \right] \quad (1.17)$$

The cross-sections for K-shell ionization do exhibit some reasonable regularities specifically, for protons and α -particles of the same *velocity*, the cross-sections scale approximately with Z_1^2 , i.e., $\sigma_K({}^4\text{He}) \approx 4 \times \sigma_K({}^1\text{H})$. Roughly speaking, relative to the cross-sections for 2 MeV protons, the energy of deuterons and α -particle beam and the magnitude of cross-section will vary as follows:

$$\sigma_{1,1}(2 \text{ MeV}) = \sigma_{1,2}(4 \text{ MeV}) \text{ and } \sigma_{1,1}(2 \text{ MeV}) = \sigma_{2,4}(8 \text{ MeV})/4$$

This trend is reminiscent of the stopping powers (discussed in Chap. 2). While proton and α -particle-induced X-ray emission have received wide attention (Johansson et al. (1970), Campbell et al. 1975), the high-energy heavy ion bombardment (HEHIX) provides improved prospects for simultaneous multi-element trace analysis over proton or X-ray bombardment. This observation is based on the following expression for predicting K X-ray production cross-sections σ_K which can be derived using the equation

$$\sigma_K = f(Z_1^2(E_1/M_1)^4 Z_2^{-12}) \quad (1.18)$$

Here Z_1 and Z_2 are atomic number of projectile and target, respectively, and E_1/M_1 is the velocity of projectile. Thus with heavy ion beam ($Z_1 > 5$) of velocity from $0.2\text{--}10\text{ MeV u}^{-1}$, σ_K , becomes very large ($10^3\text{--}10^5$ barn) for a broad range of elements and so the analytical capability (detection of trace elements ($10^{-10}\text{--}10^{-1}$ g) in microsamples ($10^{-4}\text{--}10^{-5}$ g) is improved.

Both the plane wave Born approximation (PWBA) (Merzbacher and Lewis 1958) and the binary encounter approximation (BEA) (Garcia (1970)) predict a “universal curve” in the variables σI_K^2 and E_1/I_K to describe the K-shell ionization cross-section of any atomic number target bombarded with a determine ion projectile at any energy. The cross-section being σ , I_K the binding energy of the target electron in the K-shell and E_1 the projectile energy, the fitted fifth order polynomial (Romo-Kröger (2000)) is:

$$\ln(\sigma I_K^2) = \sum_{i=1}^5 b_i \left(\frac{E_1}{I_K} \right)^i, \quad (1.19)$$

where $\{b_i\} = \{11.122, 0.6564, 0.5981, 0.0091, 0.0285, 0.006\}$.

The ionization cross-sections reach a maximum when the velocity of the incident ion matches that of the electron being ejected. A $\log_{10} - \log_{10}$ plot with the abscissa labeled by [dimensionless] and ordinate by $U_K^2 \times \sigma_K / Z_1^2 [\text{keV}^2 \text{ cm}^2]$, (where λ is the ratio M_1/m_e , E is the projectile energy, and U_K is the K-shell binding energy) is called the universal plot. The reasonably reliable values for PIXE cross-sections are available on Website www.exphys.unilinz.ac.at/Frameset/Staff.htm maintained by Prof. H. Paul at the University of Linz, Austria.

Before studying the ionization with heavy ions, we must evaluate the universal curve obtained with protons. This curve indicates that there is a marked difference of direct dependence on Z_2 , the atomic number of the target and the best fit is obtained by changing I_K by $I_K^{0.95}$, in both the abscissa and the ordinate, rather than a fixed effective charge Z_2 by $(Z_2 - 0.3)$. For cases with higher Z_2 or when $Z_1 \sim Z_2$, in which case there are other mechanisms during the ion-atom interaction, a new scaling has been made to get the proton-equivalent cross-sections, consisting in dividing the cross-sections by $Z_1^{0.8}$ rather than Z_1^2 as in the normal scaling. This corresponds to a screened nuclear charge instead of simply the projectile charge Z_1 (Romo-Kröger 2000).

The experiments conducted with protons (1.65 MeV), $^{16}\text{O}^{n+}$ (8 and 16 MeV), $^{40}\text{Ar}^{4+}$ (39 MeV), $^{63}\text{Cu}^{n+}$ (33 and 65 MeV), $^{82}\text{Kr}^{5+}$ (40.5 MeV), $^{82}\text{Kr}^{7+}$ (84 MeV), and ^{129}Xe (56 MeV) using beam current (on target) ranging from 0.03 to 100 nA, indicate that the X-ray yields are maximized when the binding energies of electrons being excited in the collision partners are approximately matched. It has been found that (1) the peak X-ray yields are obtained with a projectile $Z = Z_2 + (1 \text{ to } 5)$ (2) the enhancement effects decrease and hence the yield improves with increasing energy. Further background between the Bremsstrahlung drops off and the projectile K_α X-ray was found to be uniformly low.

For the high- Z elements ($60 < Z < 92$), the PIXE analyses can be done by detecting the L and M X-rays. The yields of K X-rays for low- Z and L X-rays of high- Z , of similar energies, are of the same order of magnitude i.e., the K X-ray cross-sections for high- Z elements decrease while the L X-ray cross-sections increase. Secondly, the K X-ray energies of these high- Z elements (being large) are not detected by the Si(Li) detector as the efficiency of the detector decreases significantly. Clearly, the analytical usefulness of heavy ion beams extends beyond X-ray emitters of atomic number lower than that of the projectile.

Heavy-ion induced X-ray emission applied to thick samples features several advantages, which are related to the small sample size assayed. As an example, with a $1\text{ MeV u}^{-1}\text{ Kr}^{7+}$ beam of $\sim 3\text{ mm}$ diameter, the weight of graphite subjected to analysis would be less than $15\text{ }\mu\text{g}$. Consequently problems associated with their target analysis (absorption of X-rays interference due to the substrate in the case of thin layer analysis) using X-ray methods are avoided.

Limitations of Heavy-Ions for PIXE Analysis

Use of heavy ions like ^{12}C , ^{16}O , ^{28}Si and still more heavy ions have the following limitation for PIXE analysis:

1. The interaction of heavy charged particles tend to destroy target by sputtering
2. The projectile X-rays are also produced, which may interfere/overlap with target (sample) X-rays
3. Molecular Orbital (MO) formation for $Z_1 \sim Z_2$

The interplay between the energy levels of the projectile and the target atoms will move the energy levels to levels appropriate to the “quasimolecule.” At sufficiently close distance of approach, the levels become those of an atom of atomic number $Z_1 + Z_2$. At intermediate separation, new X-rays seen from neither atom individually may appear. In general, the energy levels change adiabatically as the two atoms approach, but some electrons may be promoted to higher levels, leaving vacancies in the inner-shells as the atoms recede. The theory of X-ray production involving quasimolecular orbitals, has been explained in Sect. 1.11.3 under subtitle “Electron Promotion”.

Enhancement Effects

In PIXE analysis, one may come across a situation where the proton-induced characteristic X-rays of major and minor elements cause secondary fluorescence of the X-rays of other elements, enhancing its signal. Secondary fluorescence can be particularly important when the specimen matrix (different base material causing different absorption of X-rays) is composed of elements of similar atomic number; steels and other alloys are example. Neglect of

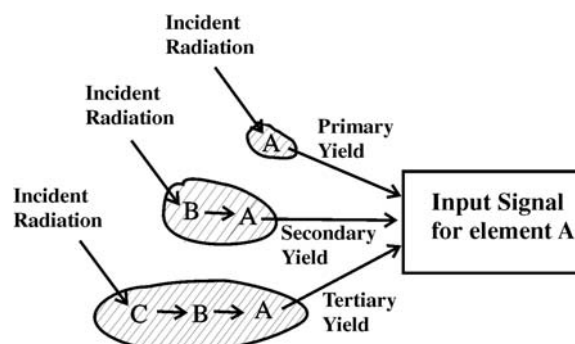


Fig. 1.18. Primary X-ray production, secondary, and tertiary fluorescence

secondary fluorescence in processing the spectral data will lead to erroneous matrix elements concentrations and these in turn will generate errors in concentrations of trace elements (Campbell et al. 1989). Similarly, any element can absorb or scatter the fluorescence of the element of interest. For example if a sample contains ^{26}Fe and ^{20}Ca , the incoming source X-ray fluoresces ^{26}Fe and the ^{26}Fe fluorescence is sufficient in energy to fluoresce ^{20}Ca . During analysis, ^{20}Ca is detected while Fe is not detected.

Figure 1.18 illustrates the situation where the PIXE yield of an element A is enhanced through the fluorescence of A by proton-induced X-rays of an element B. This can occur if the K X-ray energy of B is slightly higher than the K absorption edge of A. The examples are: Iron (B) \rightarrow Chromium (A); Nickel (B) \rightarrow Iron (A).

The lines formed by the overlap of many narrow (discrete) contributions and some continuous ones including one primary intensity plus several enhancement terms produce complicated spectrum. Fernández and Tartari (1995) have suggested the way to overcome the difficulties that such spectral complexity introduces in the process of extracting the primary fluorescence intensity from the experimental spectrum by using a theoretical spectrum.

Charging/Sparking/Heating in PIXE

The main difficulty in PIXE analysis is the collection of beam charges from insulating targets. For this purpose, the targets can be sprayed with electrons from electron gun integrated with the faraday cup. Charging effects might be responsible for local electrical potential producing the acceleration of secondary electrons resulting in intense Bremsstrahlung spectra. This effect can also be reduced by carbon shadowing or by covering the sample with a metal grid. A potential problem in PIXE analysis of thick nonconducting samples is one of the charge build-up and subsequent sparking which can cause large spikes in the spectrum and/or may deflect the proton beam resulting in poor precision. Spikes have the effect of irreproducibly increasing the background

over a large but random portion of the spectrum. Techniques such as spraying the sample with electrons from an electron gun or increasing the pressure in the target chamber can solve the problem.

The X-ray yield is strongly dependent on charge factors such as (a) imperfect charge accumulation (due to sample imperfect or beam sputtering) and (b) charge leakage (by carbon deposits or poor vacuum). Heavy ions tend to cause sputtering leaving behind minute cracks *and craters* on the large surface. This possibly leads to shorter discharge routes and a lower X-ray yield. The carbon build-up due to target burning at the beam spot from traces of oil vapors in the system conduct charge and gives low X-ray yield. With insulating materials, often poor vacuum is used. The gases in the neighborhood of the target surface are ionized by the ion beam creating a conducting path and eliminating charge build-up. Pressure exceeding 3×10^{-4} Torr was found to be adequate to centralize charge build-up and eliminating the charge-induced X-ray effect.

A few papers have discussed the problem of charge build-up on insulating samples in PIXE analysis (Gocłowski et al. 1983, Pillay and Peisach 1994). Pillay and Peisach (1994) and their other works with low energy (600–1500 keV) ions like $^3\text{He}^+$, $^3\text{He}^{2+}$, $^{14}\text{N}^+$, $^{16}\text{O}^+$, and $^{20}\text{Ne}^+$ have shown an abnormal X-ray yields, which originate from a discharge of high potential resulting from a charge build up on the surface of an insulating target with the production of a flux of electrons. These energetic electrons would have sufficient energy to excite X-rays even in situations where PIXE yields are negligible.

The very high-energy ion beam can also cause heat-up of the sample unless the current is kept low. These temperatures can cause damage to the sample and/or loss of volatiles, which may change the sample composition.

In order to reduce the high-energy Bremsstrahlung component due to the target charge-up, the use of electron gun, the foil technique, the poor vacuum, and helium filled chamber can be made. In the electron gun method, an electron gun with a commercial tungsten filament from glow lamps is used. A voltage of 6.0 V and 0.3 A gives a glow current sufficient to neutralize the charge produced by the ion beam on thick samples. Similarly placing a carbon foil (few $\mu\text{g cm}^{-2}$) about 2 cm before the target helps to eliminate the charge accumulation and the weaker X-ray lines, which were completely masked due to charging, become clearly visible.

Charge State Effect

In the description of the ion–atom collision, the electron–electron interactions play a special role due to which the electrons of the colliding partners can be excited or ionized additionally (dynamic screening) or they can undergo elastic scattering among each other (static screening). This indicates that the ionization cross-sections for the direct Coulomb ionization must be governed by the charge state (electron configuration) of the projectile (Hock et al. 1985).

The charge state fractions for heavy ions after passing through a thin foil depend upon the foil thickness. This dependence is due to the K-shell vacancies resulting from the ion–solid interaction. Hence each charge state fraction can contribute to the K-to-K electron transfer process while the ion is moving through the target thus modifying the electron configuration.

Heavy projectiles are in general highly ionized by stripping during the acceleration process before they hit the target atom. Due to the Bohr-Lamb criterion, for the average charge state, projectile electrons with projectile velocity $v_1 \leq$ orbital velocity of the electron v_2 , are ionized during penetration through a stripper foil (i.e., roughly up to $\eta = 1$). Hence the heavy projectile may only have the inner-shell electrons without any outer-shell electrons. Thus only direct excitation process in the projectile may be possible. On the other hand, capture to empty projectile states – which is normally not possible for the “neutral” target atom may also yield X-ray emission.

According to Frey et al. (1996), the effective charge of a swift heavy ion depends on its charge state and the way the charge state is screened. The incomplete screening of the charge of the ion by its remaining electrons increases the effective charge. The second screening effect is caused by target electrons due to long range of Coulomb interaction (becomes important for the energy loss process), reduces the potential of the ion due to a dynamic enhancement of the electron density at the position of the ion and reduces the effective charge compared to the real charge of the ion. According to Hock et al. (1985), the effective charge in the collision should approach the ionic charge of the projectile at high velocity limits.

The experiments relating to equilibrium charge state distribution of ions, passing through C-foils, have been done by Shima et al. (1986, 1992). The effective nuclear charges Z_1^{eff} for charge equilibrated projectiles have been calculated by Banas et al. (1999) by weighting effective charges for a given projectile charge state $Z_1^{\text{eff}}(q)$ by equilibrium charge state fractions $F(q)$ following the procedure described by Toburan et al. (1981). O’Kelley et al. (1987) have given the formulae to calculate the effective charge on the basis of the Bohr stripping criterion, for a Thomas-Fermi atom. Schiewitz and Grande (2001) have presented two fit formulae for mean equilibrium charge state of projectiles ranging from protons to uranium in gas and in solid targets.

Based on the effective charge, the theoretical cross-section values can be calculated using the first-order theories. Theoretically, the PWBA is not accurate to reproduce the experimental inner-shell ionization cross-sections for collision systems with $Z_1/Z_2 > 0.1$ in the v_1 (velocity of projectile) $< v_2$ (orbital velocity of the electron) region. For comparison, velocity v_1 in atomic units can be calculated using $6.35[E(\text{MeV})/M]^{1/2}$ while velocity v_2 in atomic units is calculated using $[\text{BE}(\text{eV})/13.6]^{1/2}$.

In one of our papers (Baraich et al. 1997), we have found a rather nice agreement between experimental and ECPSSR theory for Ni+Pb, Bi collisions using the equilibrium charge state for the projectile. The scaled projectile velocity is in the range of 1.2–1.6 in agreement with Hock et al. (1985) and the

ionic charge is the relevant effective charge in this region. Thus the experimental data can be reproduced with the best perturbative theory ECPSSR effective charge calculations.

No firm theoretical mechanism representing projectile charge structure in effective charge parameterization has yet been discovered.

1.5 Qualitative and Quantitative Analysis

For qualitative analysis, one has to look at the energy of the X-ray peaks and identify the elements from which these characteristic lines have originated. The X-ray energies of interest lie below 20 keV, where the X-rays of element with $Z < 45$ and L X-rays of the heavy elements are observed. Table 1.9 indicates the energies of K and L X-rays of a few elements:

For a sample having many elements, the L X-ray peak of a heavy element may coincide with the K X-ray peak of a light element causing confusion in analysis. Many elements, present in relatively very small quantity cause difficulty in their detection. The presence of two strong L-lines can be used to remove interference, for instance the determination of $_{82}\text{Pb}$ can be made in the presence of $_{33}\text{As}$ by using the $\text{L}\beta$ component.

When a given sample contains many elements, the X-ray lines for different elements are depicted from the energies of various X-ray lines. The energy resolution i.e., full-width at half-maximum (FWHM) is the limiting parameter for many X-ray measurements. This is so because if the energy resolution is poor, there will be overlap of component X-ray lines of one element with that of the other due to the small energy difference between the X-ray lines of

Table 1.9. Energies of K and L X-rays of a few elements

Z	Elements	K α (keV)	K β (keV)	L α (keV)	L β (keV)	L γ (keV)
13	Al	1.49	1.55			
20	Ca	3.69	4.01			
25	Mn	5.90	6.49			
30	Zn	8.63	9.62			
35	Br	11.89	13.37			
40	Zr	15.73	17.83	2.05	2.13	
45	Rh			2.70	2.83	
50	Sn			3.45	3.66	4.15
55	Cs			4.29	4.78	5.28
60	Nd			5.22	5.92	6.59
65	Tb			6.26	7.18	8.10
70	Yb			7.41	8.59	9.78
74	W			8.36	9.82	11.29
79	Au			9.66	11.53	13.99
83	Bi			10.77	13.00	15.25

adjacent elements. In the case of overlap of X-ray peaks of different elements, the elements are recognized from the nonoverlapping lines and the possibility of the existence of the corresponding line in the overlap. The peak overlaps occur because the spectral resolution of EDS (~ 150 eV) is much poor as compared to WDS (~ 5 eV). Since the energy resolution for a Si(Li) detector is of ~ 150 eV for Mn $K\alpha$ X-ray line, the separation of some peaks can therefore be poor and the interference between adjacent lines will make detection limits considerably worse. Examples include the case where small amounts of Fe are being investigated in the presence of large amounts of Mn (Mn $K\beta$ is very close to Fe $K\alpha$), and the case where Cu, Zn, and Na are present together, the L lines of Cu and Zn are close to the K lines of Na. In an energy dispersive spectrometer, even though the intense peak may not overlap the weak peak of trace element, it can increase the background for the weak peak if the intense peak has a higher energy.

When both overlapping peaks are weak and approximately equal in intensity, simple mathematical expressions for peak shapes and background can be used in a least square fitting procedure to extract the individual intensities using the Gaussian peak shapes. When the interfering peak has a very high intensity, then its shape must be known very accurately in the region where the trace element peak occurs. With an incorrect peak shape, the least square fitting method will produce a large error in the trace peak intensity. The best solution to such problem is to record the reference spectra of the two interfering elements using single element standards. This reference spectrum method can be used to subtract the background. A blank standard composed of the matrix with no trace elements is analyzed to establish the background spectrum, which is subtracted from the unknown to yield the trace element peaks without background.

The quantitative analysis with XRF and PIXE techniques generally requires calibration of the system against known reference standards (NBS, IAEA, Micromatter). These reference standards can be thin or thick ones. Yet, an absolute quantitative analytical method without external standards has been developed for thick sample analysis by XRF and PIXE and has been applied to bronze and brass alloys by Gil et al. (1989). For light ion PIXE using protons, the theoretical cross-sections and ion stopping powers are generally accepted to around $\pm 5\%$. Hence if the system is calibrated against thin targets of known composition, thick target yields can be calculated generally with a precision approaching $\pm 5 - \pm 15\%$. For absolute quantification, the knowledge regarding formalism for both thin and thick samples is required and the same is being discussed in Sect. 1.6. The spectrum of a material will contain additional peaks called escape peaks (discussed in “Energy Dispersive X-ray Fluorescence” and sum peaks due to the pitfalls in quantitative analysis using EDXRF and PIXE techniques.

The Sum peaks in the spectrum occur when the count rates are so high that when the two X-rays impinge on the detector virtually instantaneously, the pulse created and measured is the sum of the two X-ray energies. For

example, for a sample with lots of Si ($K\alpha$ of 1.74 keV) and Al ($K\alpha$ of 1.487); a peak at 3.23 keV is the sum peak, not to be assumed to be a K peak ($K\alpha$ of 3.31 keV).

If the X-ray detector in EDXRF analysis is very close to the sample or there is high beam currents in PIXE analysis, there may be “pulse pileup” where the electronics cannot keep up with the X-rays impacting the detector. The electronics/software therefore has to try to adjust for the X-rays not counted, by calculating a “dead time” correction; the larger the correction, the greater the margin of error. Generally the dead time should be kept below 20–30% (usually indicated on the monitor), either by lowering the beam current, inserting apertures in front of the detector nosepiece, or retracting the detector (if adjustable). Excessive dead time can also cause a shift of the peak position.

1.6 Thick vs. Thin Samples

Two terms relating to sample thickness are important in X-ray emission analysis: one is the linear thickness of a specimen, below which the absorption effect vanishes; the other is the critical thickness of a specimen above which the specimen becomes infinitely thick. Thick samples infer that the incident or exciting radiation is either absorbed in the sample or backscattered from it. On the other hand a thin target is a sample that is so thin that the energy loss of the particle beam in the target is very negligibly small and the intensity loss of the lowest energy photon of interest emerging from the sample material is negligible. The thickness of the sample can be related to the range of the charged particle (impinging the sample), which in turn is defined as the linear distance of the matter within which the charged particle is completely absorbed. The range of the charged particle in matter depends upon the substance as well as on the nature and energy of the charged particle. The details about stopping power and ranges is given in Sect. 2.2.3 of Chap. 2. The stopping power and ranges for various projectile-target systems can be evaluated using the computer program TRIM 91 by Ziegler et al. (1985).

The study of complex materials (nonhomogeneous matrices containing medium and/or heavy atoms as major elements) by PIXE requires the tailoring of the experimental set up to take into account the high X-ray intensity produced by these main elements present at the surface, as well as the expected low intensity from other elements “buried” in the substrate. The determination of traces is therefore limited and the minimum detection limit is generally lower by at least two orders of magnitude in comparison with those achievable for low Z matrices ($Z \leq 20$). Additionally, those high Z matrices having a high absorption capability, are not always homogeneous. The nonhomogeneity may be, on the one hand, a layered structure or on the other hand, inclusions which are to be localized. PIXE measurements at various incident energies (and with various projectiles (p, d, He^3 , He^4)) are then an alternative

method to overcome those difficulties. The use of special filters to selectively decrease the intensity of the most intense X-ray lines, the accurate calculation of the characteristic X-ray intensity ratios ($K\alpha/K\beta$, $L\alpha/L\beta$) of individual elements, the computation of the secondary X-ray fluorescence induced in thick targets are amongst the most important parameters to be investigated in order to solve these difficult analytical problems. Examples include Cr, Fe, Ni, Cu, Ag, and Au based alloys with various coatings as encountered in industrial and archaeological materials. RBS (Chap. 2), NRA and PIGE (Chap. 7) are sometimes simultaneously necessary as complementary (or basic) approaches to identify corroded surface layers (Demortier 1999).

In a more general case, the major considerations attributable to the thickness of the sample are self absorption of the characteristic X-rays (absorption by the specimen) and scatter mass thickness (property for scattering of X-rays – product of density and thickness of the specimen since the intensity of scattered X-rays is proportional to the mass thickness of the specimen) that may occur when the excitation energy passes through the material in the specimen chamber. If the photons are incident on the material, the attenuation coefficient can be calculated using XCOM computer software by Berger and Hubbel (1987). The program provides total cross-sections and attenuation coefficients as well as partial cross-sections for the following processes: incoherent scattering, coherent scattering, photoelectric absorption, and pair production in the field of the atomic nucleus and in the field of the atomic electrons. For compounds, the quantities tabulated are partial and total mass interaction coefficients, which are equal to the product of the corresponding cross-sections times the number of target molecules per unit mass of the material. The reciprocals of these interaction coefficients are the mean free paths between scatterings, between photoelectric absorption events, or between pair production events. The sum of the interaction coefficients for the individual processes is equal to the total attenuation coefficient. Total attenuation coefficients without the contribution from coherent scattering are also given, because they are often used in γ -ray transport calculations. For the purpose of interpolation with respect to photon energy, the coherent and incoherent scattering cross-sections and the total attenuation coefficients are approximated by log–log cubic-spline fits as functions of energy.

For a thin target, the atomic abundance of the trace element present is obtained by dividing the yield of X-rays per incident charged particle (in PIXE) or photon (in XRF) and the detection efficiency. However if one uses a target of moderate thickness, as is necessary to achieve a good counting rate, the correction due to self absorption (in XRF) and also the correction for the loss of energy of the charged particle (in PIXE) is to be applied since the charged particle of varying energy produces vacancies in inner atomic shells at various depths of the target, the cross-section for vacancy production goes on varying, normally decreasing at low energies.

In many problems of trace analysis, the scatter mass limits the performance of the X-ray energy spectrometer in thick samples. Since the backscatter

contribution to the spectrum increases with decreasing atomic number matrices, it has been found that the inelastic or Compton contribution to the backscatter dominates the spectrum. At increasing higher excitation energies (using secondary targets) the spread between the Compton peak and the elastic peak becomes increasingly greater. Since the measured X-ray intensity of element is considered as directly proportional to the mass (m_i), the increased thickness gives better sensibility.

The advantage of thin sample analysis is that self absorption of radiation can be neglected and the cross-section being constant, can be used in calculating the concentration. Other advantages of thin foil technique are low background in the measurement and absence of charge effects present in thick insulating sample.

1.6.1 Formalism for Thin-Target XRF

To convert the peak intensities into the elemental mass concentrations, a fundamental parameter approach is used. According to this approach, the intensity N_{ij} of the fluorescent X-ray line i of the j th element, is related to the mass m_j of the element present in the sample

$$N_{ij} = I_0 G \varepsilon_{ij} \beta m_j \sigma_{ij}(E) \quad (1.20)$$

where N_{ij} are the number of counts s^{-1} for the i th X-ray ($K\alpha, K\beta, L\alpha, \dots$) photopeak of the j th element, I_0 is the intensity of the photon emitted by the source, G is the geometry factor. ε_{ij} represents the relative efficiency to excite and detect the fluorescent X-rays from j th element, m_j is the elements concentration ($g\text{ cm}^{-2}$) which is to be determined and $\sigma_{ij}(E)$ is the XRF cross-section.

The absorption correction term β , for intermediate thick sample, is given by

$$\beta = \frac{1 - \exp[-(\mu_i \csc \phi - \mu_f \csc \psi)]M}{(\mu_i \csc \phi - \mu_f \csc \psi)M} \quad (1.21)$$

Here M is the total mass of the sample, $\mu_i(\mu_f)$ is the mass absorption coefficient at incident (fluorescent) energy and $\phi(\psi)$ is the grazing angle of incidence (fluorescence).

The self-absorption effects become negligible if the targets are very thin and of uniform thickness, The elemental concentration $m_j(g\text{ cm}^{-2})$ in various samples can be determined using the expression:

$$m_j = \frac{N_{ij}}{I_0 \times G \times \varepsilon_{ij} \times \sigma_{ij}} \quad (1.22)$$

The XRF cross-section $\sigma_{ij}(E)$ is defined as:

$$\sigma_{ij}(E) = \sigma_{\text{photo}}^i(E) \left(1 - \frac{1}{J_{K,L}}\right) \times \omega_x \times F_{ij} \quad (1.23)$$

where $\sigma_{\text{photo}}^j(E)$ is the photoelectric cross-section of the element j at the excitation energy E and $J_{K,L}$ is the jump ratio, ω_x is the fluorescence yield for subshell “x” from which the i th X-ray originates and F_{ij} is the fractional emission rate. An indirect way to calculate the photoelectric or photoionization cross-section, $\sigma_j(E)$ or $\sigma_{\text{photo}}(E)$ involves the subtraction of $\sigma_{\text{incoherent}}(E)$, $\sigma_{\text{coherent}}(E)$ and $\sigma_{\text{pair prod.}}(E)$ cross-section from the total measured cross-section of the incident photons with the matter. The values of $\sigma_{\text{photo}}(E)$ have been given by Storm and Israel (1970).

The variation of total attenuation cross-section $\sigma_{\text{tot}}(E)$ as a function of incident photon energy, displays the characteristic saw-tooth structure in which sharp discontinuities arise whenever the incident energy coincides with the ionization energy of the electrons in the K, L, M, ... shells as shown in Fig. 1.6. The sharp discontinuities, also known as absorption jumps in cross-sections at photon energies corresponding to the shell binding energies (Table 1.4), are due to the photoelectric interaction becoming energetic in that shell. The K-jump ratio is defined as the ratio of the upper to the lower edge photoionization cross-section at the K-shell binding energy. In other words, the absorption jump factor (J_K) is associated with the photoelectric absorption coefficient τ for different shells/subshells (i.e. $\tau_K, \tau_{L_I}, \tau_{L_{II}}, \dots$) and is defined as the fraction of the total absorption that is associated with a given level for a given interval of energy. For example, the jump factor J_K at energy E_A is:

$$J_K = \frac{\tau_K}{\tau_K + \tau_{L_I} + \tau_{L_{II}} + \tau_{L_{III}} + \dots} \quad (1.24)$$

Veigle (1973) has given an empirical relation between K-jump ratio and the atomic number of the element

$$J_K = \left(\frac{125}{Z} \right) + 3.5 \quad (1.25)$$

From K-jump ratio, one can obtain K-shell to total photoionization cross-section ratio. Again there is an empirical relation, given by Hubbel (1969) between K-shell to total photoionization cross-section ratio and atomic number of the element

$$\sigma_{\text{photo}}(E)/\sigma_K(E) = 1 + 0.01481 (\ln Z)^2 - 0.00078 (\ln Z)^3 \quad (1.26)$$

Further, K-jump ratio and K-shell-to-total photoionization cross-section ratios are connected by the relation:

$$\frac{\sigma_{\text{photo}}(E)}{\sigma_K(E)} = \left(\frac{J_K - 1}{J_K} \right) = \left(1 - \frac{1}{J_K} \right) \quad (1.27)$$

Fluorescence yield (ω_x) of an atomic shell/subshell is defined as the probability that a vacancy in that shell/subshell is filled through radiative transitions. Since the vacancy can also be filled by nonradiative processes (Auger electrons and Coster-Kronig transitions), the fluorescence yield (ω_K or ω_L) = Radiative yield/Total yield. The fluorescence yield values have been given by Bambynek et al. (1972) and Krause (1979).

Since the rate of decay of a vacancy state is the sum of radiative and non-radiative transition rates, the ratios of the intensities of individual X-ray lines are proportional to the ratio of the rates for the corresponding transitions. The fractional emission rates F_{ij} (where i is the number of subshell and j is the transition e.g., For L_α we take $F_{3\alpha}$) is defined as:

$$F_{ij} = \frac{j\text{th X-ray emission rate}}{\text{Total X-ray emission rate for all transition from } i\text{th subshell}} \quad (1.28)$$

Scofield (1974) has calculated atomic X-ray emission rates for the elements $5 \leq Z \leq 104$ while the experimental values of the relative K and L X-ray emission rates have been given by Salem et al. (1974).

The accuracy of numerical calculations of the X-ray production cross-sections depends upon accuracy of various terms which are involved in the expression (1.23) and comes out to be 4–6%.

1.6.2 Formalism for Thick-Target XRF

If the target is appreciably thick, a fraction of the incident photons gets absorbed by the target as they penetrate deep in the target material. Similarly a fraction of fluorescent X-rays emitted by the target are absorbed as they reach the surface of the target. Correction has thus to be applied to take care of these absorption effects.

Figure 1.19 shows the schematic diagram for the arrangement of source, thick target, and detector in reflection geometry.

Let t be the actual thickness of the target (g cm^{-2}). To make correction t is replaced by t_{eff} an effective thickness given by:

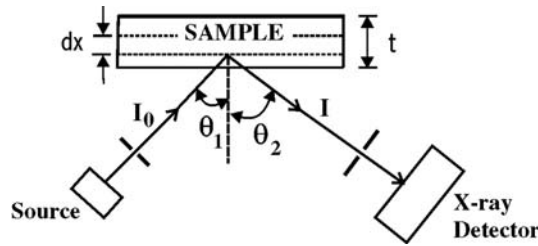


Fig. 1.19. Schematic diagram showing the arrangement of source, thick target, and detector in reflection geometry

$$t_{\text{eff}} = \beta \times t = \frac{1 - \exp(-) \left(\frac{\mu_{\gamma}}{\cos \theta_1} + \frac{\mu_x}{\cos \theta_2} \right) \times t}{\left(\frac{\mu_{\gamma}}{\cos \theta_1} + \frac{\mu_x}{\cos \theta_2} \right)} \quad (1.29)$$

Here μ_{γ} and μ_x (in $\text{cm}^2 \text{g}^{-1}$) are the mass absorption coefficients of the target material for incident photons and characteristic X-rays produced in the target with the impact of incident photons. Thus (1.22) gets modified to:

$$m_j = \frac{N_{ij}}{I_0 \times G \times \varepsilon_{ij} \times \sigma_{ij} \times \beta_{ij}} \quad (1.30)$$

where β_{ij} is the correction factor for the i th X-ray ($K\alpha, K\beta, L\alpha, L\beta, \dots$) photopeak of the j th element.

The mass absorption coefficients listed in the literature are at particular energies, say E_1, E_2, E_3, \dots . The interpolated value at a specified energy E in between E_1 and E_2 is calculated using the following formulae:

$$\mu(E) = \mu(E_2) \times (E/E_2)^{\eta} \quad (1.31)$$

where

$$\eta = \frac{\log(\mu(E_1)) - \log(\mu(E_2))}{\log(E_1) - \log(E_2)} \quad (1.32)$$

Trace analysis permits some simplification of the quantitative models used to calculate concentrations from measured intensities. There are usually two methods for accurate measurement i.e., internal standard method and fundamental parameter method.

In the internal standard method, the sample can be homogenized and split into three or more identical samples. The first sample is analyzed qualitatively and a rough estimate of the concentration of each element is made. The second sample is spiked with known amounts of one or two element to bring the concentration to approximately 10 times the estimated concentration in the unknown. From the known standards, one can draw the calibration curve and from the differences in the intensities one can calculate the concentration of each element in the unknown.

A more ideal situation is the availability of a number of samples having constant composition of the matrix but only trace elemental concentration varying from specimen to specimen. Here the most desirable method for generating the calibration curves is by making up standards of known composition. The set of standards can include the range of concentrations for all the elements, as several standards are required for each element.

In the fundamental parameter calculation, the calculations of different parameters of (1.30) is made especially for low-atomic number specimens containing only trace elements as these considerably simplify the theoretical calculations. Fundamental methods are particularly simple if monochromatic excitation is used.

1.6.3 Formalism for Thin-Target PIXE

The X-ray yield for each energy interval E to $(E - dE)$ of the ion is given by the product of the number of incident particles hitting the target and the number of target atoms in the region corresponding to the energy interval per unit area, the vacancy production cross-section in the atomic shell, the fluorescence yield of the atomic shell, the freedom of X-rays being detected (e.g., $K\alpha, K\beta, \dots$), the attenuation of these X-rays in traversing a distance x (where x is determined from the distance traversed by the ion in the bulk material of the target in getting slowed down from the incident energy to the energy $E - \Delta E$) and the efficiency of detection of the X-rays including the solid angle of the detector.

The solid targets are considered to be thin, if only a fraction of the energy is lost by the projectile while traversing through the target. If the target is thicker than the range of the ion in the target, the thickness traversed by the ion would be the range itself and the final energy of the ion would be zero (see formalism for thick targets in that case). In the case of thin targets, when N_p protons of energy E_0 pass through a thin, uniform and homogenous target of effective thickness t (in cm) of atomic number Z and atomic mass A , the i th ($K\alpha, L\alpha, \dots$) X-ray yield is:

$$Y_{x_i}(Z, E_0) = \sigma_{x_i}(Z, E_0) \times (nt') \times N_p \times \varepsilon_{x_i} \quad (1.33)$$

where $\sigma_{x_i}(Z, E_0)$ is the production cross-section (in cm^2 per atom) of the i th X-ray of element Z at energy E_0 , which can be calculated by incorporating the correction factors as:

$$\sigma_{x_i} = \frac{Y_{x_i}}{(nt') \times \varepsilon_{x_i} \times N_p} \times \frac{\Gamma_x}{\Gamma_R} \times C_i \quad (1.34)$$

Here ε_{x_i} is the detection efficiency of the X-ray detector that accounts for the absorption by the chamber window, solid angle subtended by the Si(Li) detector at the target; nt' is target areal density i.e., number of target atoms per unit area; n is target number density; t is target thickness; C_i is Correction factor due to the energy loss of the charged particle and self-absorption of the X-rays due to finite thickness of the target, and Γ_x and Γ_R are the Dead-time correction for the X-ray and charged particle detectors.

The effective target thickness (t') is calculated from the actual thickness (t) using the relation

$$t' = t \exp \left[- \left(\frac{\mu}{\rho} \right) \times \frac{t \sec \theta_0}{2} \right] \quad (1.35)$$

where μ/ρ is the mass attenuation coefficient (in $\text{cm}^2 \text{g}^{-1}$) and θ_0 is the direction of detected X-rays to the target surface normal.

The particle flux incident on the target N_p is calculated by applying Rutherford scattering formula (see Chap. 2)

$$N_p = \frac{N_{Sc}(E, \theta)}{\left[\frac{d\sigma}{d\Omega}(E, \theta) \right]} \frac{1}{(nt') d\Omega} \quad (1.36)$$

Combining these two equations we get

$$\sigma_{x_i} = \frac{Y_{x_i}}{N_{Sc}} \frac{d\Omega}{\varepsilon_{x_i}} \left[\frac{d\sigma}{d\Omega}(E, \theta) \right] \frac{\Gamma_x}{\Gamma_R} C_i \quad (1.37)$$

From this formula for thin target, we find that the target density factor cancels out and thus the error due to uncertainty in the measurement of target thickness gets eliminated. However, the target thickness is used in the determination of the correction factor C_i . Depending upon the target thickness, the correction factor C_i can be calculated by either of the two methods.

The method of O'Kelley (1984) is applied when the energy loss by the projectile in the target is large (about 20% of the incident projectile) i.e., when the target thickness is of the order of 1 mg cm^{-2} . In this method

$$C_i = C_x \times C_R \quad (1.38)$$

where C_x and C_R are the correction factors due to self absorption of the X-rays by the target and slowing down of the projectile in the target, respectively.

$$C_x = \mu' t' / (1 - \exp(-\mu' t')) \quad (1.39)$$

where $\mu' = \mu \cos \theta / \cos \phi$; μ is the self attenuation mass coefficient for the X-ray energy.

$$C_R = \frac{1}{(1 - \overline{\Delta E_R}/E_1)^2} \quad (1.40)$$

$$\overline{\Delta E_R} = S(E_1) t' / 2$$

where $S(E_1)$ is the stopping power of the target for the incident projectile of energy E_1 .

The energy lost by the projectile in the target is given by:

$$\overline{\Delta E} = \frac{2 \left[1 - (1 + \mu' t') e^{-\mu' t'} \right]}{\mu' t' (1 - e^{-\mu' t'})} \times \overline{\Delta E_R} \quad (1.41)$$

When the target thickness is such that the energy loss of the projectile in target is negligible i.e., target thickness is of the order of $\mu\text{g cm}^{-2}$

$$C_i = \frac{1 + \frac{\beta + 2}{2} \times \frac{\Delta E}{E_1}}{1 - \frac{1}{2} \left[\alpha - \beta + \frac{\mu(E_1)}{S(E_1)} \right] \frac{\Delta E}{E_1}} \quad (1.42)$$

Here α and β are the parameters which are determined from the X-ray production cross-section and stopping power of the target

$$\begin{aligned}\sigma^X &\propto E_1^\alpha \\ S(E_1) &\propto E_1^\beta\end{aligned}\tag{1.43}$$

The ionization cross-sections values ($\sigma_K^I, \sigma_{L_1}^I, \sigma_{L_2}^I, \sigma_{L_3}^I, \dots$), available in the literature (Orlic et al. 1989, Cohen 1990) can be converted to the production cross-sections using the following relations:

$$\begin{aligned}\sigma_{K\alpha}^X &= \sigma_K^I \times \omega_K \times \Gamma_{K\alpha} / (\Gamma_{K\alpha} + \Gamma_{K\beta}) \\ \sigma_{K\beta}^X &= \sigma_K^I \times \omega_K \times \Gamma_{K\beta} / (\Gamma_{K\alpha} + \Gamma_{K\beta}) \\ \sigma_{L\alpha}^X &= (\sigma_{L_1}^I f_{12} f_{23} + \sigma_{L_1}^I f_{23} + \sigma_{L_2}^I f_{23} + \sigma_{L_3}^I) \omega_3 F_{3\alpha} \\ \sigma_{L\beta}^X &= \sigma_{L_1}^I \omega_1 F_{1\beta} + (\sigma_{L_2}^I + \sigma_{L_1}^I f_{12}) \omega_2 F_{2\beta} \\ &\quad + (\sigma_{L_1}^I f_{13} + \sigma_{L_1}^I f_{12} f_{23} + \sigma_{L_2}^I f_{23} + \sigma_{L_2}^I) \omega_3 F_{3\beta} \\ \sigma_{L\gamma}^X &= \sigma_{L_1}^I \omega_1 F_{1\gamma} + (\sigma_{L_2}^I + \sigma_{L_1}^I f_{12}) \omega_2 F_{2\gamma}\end{aligned}\tag{1.44}$$

The fluorescence yield values (ω_i) of the L-subshell and the Coster-Kronig transition probabilities (f_{ij}) are listed by Krause (1979). The relative radiative transition probabilities (F_{ij}) of the i th subshell contributing to the j th peak can be taken from Cohen (1990). The ionization cross-sections can be theoretically calculated using the ECPSSR theory (see Sect. 1.11.3 for different theories on ion-atom collision).

For $Z_1/Z_2 > 0.3$ and for projectiles having either one vacancy or bare-projectiles, the electron capture contribution to the inner-shell target vacancy production rates become significant and must be added to direct ionization contribution.

If the experiment is conducted with heavy ions like deuteron and α -particles, the value of ionization cross-section σ_K, σ_{L_i} can be calculated from the corresponding proton values using the Z_1^2 scaling law e.g.,

$$\sigma_D(E) = \sigma_P(E/2) \text{ and } \sigma_{He}(E) = 4\sigma_P(E/4)$$

The scaling law is extended for still heavier ions like ${}_6C^{n+}, {}_8O^{n+}, \dots$, using term R which takes care of the effective charge due to charge exchange between the projectile and the target. Thus

$$\sigma_{L_i}^{ion}(E) = Z_1^2 R \sigma_{L_i}^{proton}(E_1/M_1)\tag{1.45}$$

1.6.4 Formalism for Thick-Target PIXE

The solid targets are considered to be thick if the projectile lose whole of its energy while passing through the target. In PIXE analysis of thick samples, the following points have to be considered: the slowing down of protons (or

other charged particles) and the decrease of ionization cross-section $\sigma_{x_i}(E)$ in deeper layers, the attenuation of characteristic X-rays in deeper layers by the photoelectric effect and scattering and the enhancement of X-rays with those elements with absorption edges just below the emission energies of dominant elements. Neglecting the enhancement effect, the number of X-rays of an element $Y(Z)$ is proportional to the mass concentration $W(Z)$ of this element in the homogenous sample i.e.

$$Y(Z) = N_p \times \left(\frac{N_{av}}{M} \right) \times \varepsilon_{x_i} \times W(Z) \int_{E_0}^0 \frac{\sigma_{x_i}(E) \times T(E)}{S(E)} dE \quad (1.46)$$

where E_0 is the incident proton energy (MeV), N_{av} is the Avogadro number, M is the atomic weight of the trace element of atomic number Z , and σ_{x_i} is the X-ray production cross-section (cm^2 per atom). The X-ray production cross-sections of an X-ray transition at projectile energy E_1 are related to the measured values by the Merzbacher–Lewis (ML) formula

$$\sigma_{x_i}(E_1) = \frac{1}{n\varepsilon_{x_i}} \left[S(E_1) \left(\frac{dY_{x_i}}{dE_1} \right)_{E_1} + \mu_{x_i} \frac{\cos \theta}{\cos \phi} (Y_{x_i})_{E_1} \right] \quad (1.47)$$

where n is the target number density; ε_{x_i} is efficiency of the Si(Li) detector corrected for solid angle at X-ray peak energy; $S(E_1)$ is Stopping power of the projectile in the target element (use TRIM); $(dY/dE_1)_E$ is Slope of the curve between X-ray yield per particle at the incident particle energy, μ_{x_i} is mass absorption coefficient of the target element at the energy of i th X-ray peak (use XCOM); $(N_{Lx_i})_{E_1}$ is Yield of the i th X-ray peak per incident particle at the projectile energy E_1 ; and θ and ϕ are the angles which the normal to the target makes with the beam direction and Si(Li) detector.

In the thick target analysis the main error is caused due to the determination of dY/dE_1 and uncertainty in the stopping power. The particle flux N_p incident on the target is calculated from the yield of scattered particles (N_{sc}), using the Rutherford scattering formula (1.36).

In (1.47), the efficiency of the detector (ε_{x_i}) also includes the effect of solid angle subtended by the detector on the target and the attenuation of the X-rays between the target and the front face of the detector; The stopping power $S(E_1)$ values at different energies for different elements of the given compound can be calculated from analytical relationship, for finding the interpolated values, by using the multiple parameter least square fitting to the available data (Andersen and Ziegler 1977). The total value of the stopping power for the compound $X_n Y_m$ at a particular energy can be calculated by using Bragg's additivity rule (Bragg and Kleeman 1905)

$$S(X_n Y_m) = n S(X) + m S(Y) \quad (1.48)$$

where $S(X)$ and $S(Y)$ are the stopping powers ($\text{MeV cm}^2 \text{g}^{-1}$) of the elements X and Y , respectively. Bragg's rule does not take into account effects of chemical bonding, physical state, or lattice structure.

As the thickness of the target becomes appreciable, the fraction of fluorescent X-rays emitted by the target gets attenuated as they reach the surface of the target. Thus correction to the values of absorption coefficient has to be applied to take care of this absorption effect. The values for self absorption coefficient can be calculated from the values given by Hubbel (1982) who has presented the absorption coefficients for photon energies 1 keV–20 MeV for elements with atomic number $Z = 1$ –92. The values for self absorption coefficient can be calculated using the X-COM program of Berger and Hubbel (1987). In practice it is not possible to obtain the absorption coefficients from the tabulated values since the absorption coefficients are often needed at photon energies other than those included in the tables. Photon cross-sections for compounds can of course be obtained rather accurately (except at energies close to absorption edges) as weighted sums of the cross-sections for the atomic constituents. However, the required numerical work is tedious, and the task is further complicated by the fact that photoabsorption cross-sections and total attenuation coefficients are discontinuous at absorption edges. The presence of these discontinuities makes it desirable that cross-section tables for compounds include photon energies immediately above and below all the absorption edges for all the atomic constituents, and this requires much additional interpolation. Since the cross-sections in the vicinity of absorption edges have simple sawtooth shapes, the values at the edge can be obtained by extrapolation of the near-edge subshell cross-sections to the threshold edge energies according to the procedure employed by Berger and Hubbel (1987) using XCOM program.

The photon attenuation $T(E_1)$ is expressed by the relation

$$T(E_1) = \exp \left[-\mu \int_{E_0}^{E_1} \frac{dE_1}{S(E_1)} \times \frac{\cos \theta_i}{\cos \theta_0} \right] \quad (1.49)$$

where $\mu = \sum \mu_j \times C_j$ is the composite mass attenuation coefficient of the matrix ($\text{cm}^2 \text{g}^{-1}$); μ_j is the coefficient of the j th matrix element; C_j is the relative concentration of the j th matrix element; θ_i is the angle of the incident beam with respect to the matrix normal, and θ_0 is the angle of the detector with respect to the matrix normal. To calculate the matrix corrections, the integration is replaced by a summation of sample slices of equal proton energy loss and some approximations are introduced. The absorption coefficients $\mu(E_x)$ at X-ray energy E_x is calculated using (1.31). A critical survey of the mathematical matrix correction procedures for X-ray fluorescence analysis has been made by Tertian (1986).

If the sample is reduced to a fine powder, the analysis of the nonmajor elements (less than a few percent) may be obtained by the internal standard

technique. The Internal Standard method rests on the principle of adding a known concentration of a reference element. Introducing one percent of the element to be analyzed in the powdered sample gives rise to a very slight difference in the attenuation factors. The use of selective absorbers is often necessary for the separation of peaks of neighboring elements with vast difference in the intensities.

If we compare the X-ray yield of the sample with a standard in the same geometrical conditions, the weight (W_Z) of an element of atomic number Z can be estimated using the relation

$$W_Z = \frac{M_Z}{M_{st}} \times \frac{\sigma_{st}^x}{\sigma_Z^x} \times \frac{\varepsilon_{st}}{\varepsilon_Z} \times \frac{Y_Z}{Y_{st}} \times W_{st} \quad (1.50)$$

where M is the atomic mass, σ^x is the X-ray production cross-section, ε is the detector efficiency of the Si(Li) detector, and Y is the number of counts for X-ray peaks corrected for the absorption in the target, the vacuum chamber window and the air path. The suffices “st” and Z refer to the standard element and element of atomic number Z . For the analysis of trace element in a known matrix is the derivation of $f(\alpha, E_1, \theta, \phi)$ values from measurements on thin single element standards. This permits determination of the concentration $W(Z)$ from the measured X-ray yields $Y(Z)$.

For specimen such as alloys there is no distinction between trace and matrix elements and we simply have a specimen of unknown elemental composition. In this case (1.50) transforms to

$$W(Z) = \frac{I_{st}(Z)}{I(Z)} \frac{Y(Z)}{Y_{st}(Z)} \quad (1.51)$$

where $I(Z)$ and $I_{st}(Z)$ are the integrals of the (1.46) for the specimen and the standard, respectively. Since the parameters $S(E_1)$, $T(E_1)$ of integral are not known, an iterative solution of the set of equations (1.51) is found. This starts with a “guessed” set of concentration values from which $S(E_1)$, $T(E_1)$ and the integral may be evaluated and a new set of $W(Z)$ values obtained by comparing calculated and measured values $Y(Z)$; the new $W(Z)$ values used to recalculate $S(E_1)$, $T(E_1)$ and the integral for another round and so on. The iteration is terminated when self-consistency is achieved for either the $W(Z)$ values or the calculated X-ray yields $Y(Z)$.

The computing treatment of a PIXE spectrum can give the elementary concentration of more than 20 elements with a detection limit near the ppm. The reality or the confidence in these absolute values given by the PIXE method depends on many factors such as the counting statistics, the background under the particular peak and the spectrum interpretation (refer to Fig. 1.20 for spectrum background).

When analyzing a spectrum, various factors such as the secondary fluorescence, autoabsorption of X-rays by the target and filters, escape peaks, and electronic pile-up have to be taken into account. With all these possible errors, the confidence in the results is near 5% in the case of thick targets for which

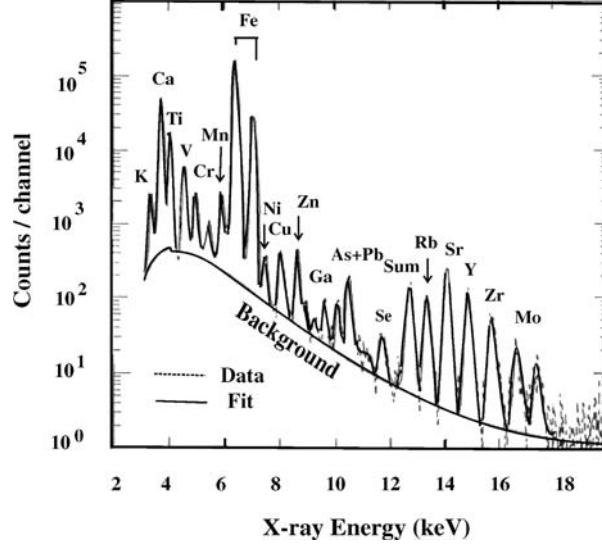


Fig. 1.20. The background and the elements in a PIXE spectrum of Perspex

the slowdown of incident particles, when they penetrate the target, is another source of error. Indeed, the probability of X-ray production depends on the incident particle energy and it is not always evident to precisely know the energy lost per unit of charged particle penetration in the analyzed matter.

1.7 Counting Statistics and Minimum Detection Limit

The measurement of peak intensity from an X-ray peak is illustrated through Fig. 1.21, where the counts/channel are plotted on log-scale. The peak is generally described by the Gaussian distribution, which is represented as:

$$P(x) = \frac{1}{\sigma\sqrt{2\pi}} \exp\left(-\frac{(x - \mu)^2}{2\sigma^2}\right) \quad (1.52)$$

The two parameters μ and σ^2 correspond to the mean and variance (square of the standard deviation) of the distribution. The resolution (FWHM) is interpreted in terms of σ as:

$$\text{FWHM} = 2\sigma\sqrt{2 \ln 2} = 2.35\sigma \quad (1.53)$$

The error in the measurement of the area (counts under the peak) depends on the limits. For example area lying between $(\mu - 0.68\sigma)$ and $(\mu + 0.68\sigma)$ has 50% probability or measured with 50% confidence, area lying between $(\mu - \sigma)$ and $(\mu + \sigma)$ has 68% probability or measured with 68.3% confidence, area lying between $(\mu - 1.65\sigma)$ and $(\mu + 1.65\sigma)$ has 90% probability or measured with 90% confidence while area lying between $(\mu - 2\sigma)$ and $(\mu + 2\sigma)$ has 95.5% probability and area lying between $(\mu - 3\sigma)$ and $(\mu + 3\sigma)$ has 99.7% probability.

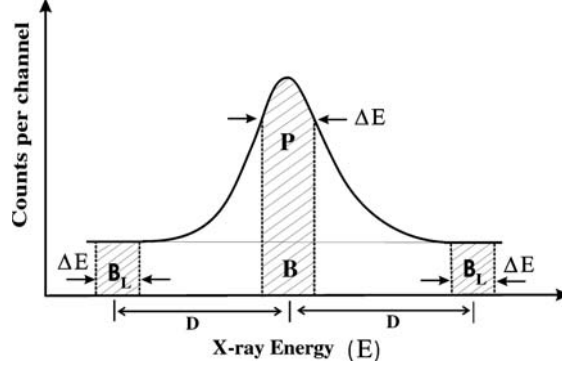


Fig. 1.21. Peak and background measurements from the spectrum of a typical X-ray line

The integral of the counts under the peak (say for n_p channels)

$$N_t = p + B$$

where p is the net area of the peak above the background and B is the contribution due to background. Therefore,

$$p = N_t - B$$

The expected standard deviation for p is,

$$\sigma_p = \sqrt{(\sigma_{N_t}^2 + \sigma_B^2)} \quad (1.54)$$

The background (under the peak) is estimated by integrating $n_B/2$ channels symmetrically on either side of the peak. If N_B are the background counts ($= B \cdot n_B/n_p$);

$$\sigma_p = (N_t + N_B)^{1/2}$$

The figure of merit $F_m = (\sigma_p/p)^{-1}$. A high value of F_m corresponds to a small statistical error.

The line to background intensity ratio (L/B) is the ratio of the net peak height above background to the background height. The plot of figure of merit as a function the integration limits show that ΔE should be set at 1.2 times the FWHM of the characteristic peak, when the minimum detection limit is reached. At high L/B ratio, the width of the peak integration region should be approximately twice the FWHM.

If the data is accumulated for the present livetime t_l , the intensities or number of counts per sec. under the peak are given by,

$$I_{p-b} = p/t_l = (N_t - B)/t_l$$

and the percent standard deviation is I_{p-b}

$$\sigma = (\sigma_p/p) \times 100\% \quad (1.55)$$

To detect the presence of the peak, the difference $\delta = (N_t - B)$ is examined. If δ is larger than the detection threshold δ_{MDL} , the element is claimed to be present. If a 95% confidence threshold is desired, then;

$$\begin{aligned}\delta_{\text{MDL}} &= 1.645\sigma_\delta \\ (I_{\text{p-b}})_{\text{MDL}} &= 1.645(I_b/t_l)^{1/2}\end{aligned}$$

If m is the sensitivity, the concentration is related to intensity by:

$$I_p = mC + I_b$$

or

$$mC = I_{\text{p-b}} = I_p - I_b$$

then

$$C_{\text{MDL}} = (1.645/m) \sqrt{(I_b/t_l)} \quad (1.56)$$

The minimum detection limit is based on the criterion that peak-to-background ratio be equal to or larger than 1 and defines the concentration level above which it is possible to say with confidence that the element is present. For the simple standard method, earlier equation can be written as:

$$C_{\text{MDL}} = \frac{1.645 C_{\text{std}}}{\left[\left(\frac{I_{\text{p-b}}}{I_b} \right) \times (I_{\text{p-b}}) \times t_l \right]^{1/2}} = \frac{1.645 C_{\text{std}}}{\left[\left(\frac{P}{B} \right) \times \left(\frac{P}{t_l} \right) \times t_l \right]^{1/2}} \quad (1.57)$$

where the intensities or counts are measured on the standard of concentration C_{std} .

Based on the analysis made for thousands of thick obsidian and pottery samples analyzed over a six-year period, the accuracy and precision of PIXE measurements for thin and thick sample analyses have been found to be as low as $\pm 1.6\%$ for major elements with precision ranging from $\pm 5\%$ to $\pm 10\%$ depending on the elemental concentration (Cohen 2002).

1.8 Sources of Background

Figure 1.22 shows a typical background intensity distribution curves for XRFS and PIXE in the energy range of 0–30 keV. The background intensity distribution follows those of the excitation cross-section. In PIXE, the ionization cross-section of the elements decrease with increasing atomic number, while in X-ray photoexcitation the cross-section increase with increasing atomic number; thus the background curves are opposed.

In PIXE, the background level at higher energy is mainly due to the Compton scattering of X-rays from the decay of excited nuclear states e.g., 3 MeV protons on Al produce γ -transitions of 170, 843, and 1,013 keV due to ^{27}Al . Protons of 5 MeV bombarded on V produce γ -transitions 320 keV due to ^{51}V , 48 MeV ^{16}O on C produce γ -transitions of 440 keV due to ^{23}Na ; the 440 keV level in ^{23}Na is populated through the $^{12}\text{C}(^{16}\text{O}, \alpha p)^{23}\text{Na}$ reaction.

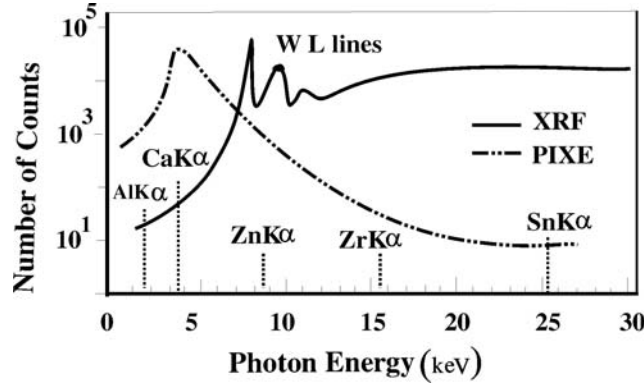


Fig. 1.22. Typical background intensity distribution curves for XRF and PIXE analyses in the 0–30 keV energy range

The γ -peaks are transitions from states in the target nucleus populated by inelastic scattering. The Compton scattering of these γ -rays is responsible for the observed background level. As this is very critical for the sensitivity, it is worthwhile to consider the nuclear reaction cross-sections. Since the Compton scattering of the γ -rays is much more important than the projectile Bremsstrahlung for the 3 and 5 MeV/u bombardment energies, from the point of view of $1/Z_1^2$ scaled background, it appears that it is not advantageous to employ projectile heavier than protons. At lower bombarding energies however the X-rays will be of less importance and it will be left to the projectile Bremsstrahlung to determine background at high radiation energies.

The $(1/Z_1^2)(d\sigma/dE_r)$ (in barns/keV) plot against E_r (radiation energy in keV) by Folkmann et al. (1974) gives the background radiation energies upto 100 keV for 3–5 MeV/amu projectiles of protons, α -particles and ^{16}O bombarded on plastic foil. For radiation energy up to ~ 20 keV, the secondary electron Bremsstrahlung falls very steeply roughly as E_r^{-10} to E_r^{-12} . At about 20 keV, the curves become flat and in case of the proton, they come down to the vicinity of the projectile Bremsstrahlung. For lower proton energies 0.5–3 MeV, it gives a quantitative description of the high-energy proton background because of the $(Z_1/M_1 - Z_2/M_2)^2$ term in the cross-section formula for electric dipole radiation. The projectile Bremsstrahlung becomes negligible for α and ^{16}O bombardment on light nuclei.

One reason that the observed background is higher than the proton Bremsstrahlung (and for α and ^{16}O it is even much higher) lies in the high energy of these projectiles and their consistently higher probability of producing X-rays by nuclear reactions.

Since the minimum detection limit is controlled by the sensitivity for the element and the background contribution, it is important to understand the sources of background in order to reduce their contribution for the trace element analysis. The sources of background are described in the following sections.

1.8.1 Contribution of Exciter Source to Signal Background

When X-ray tube is used as a source *in the XRF analysis*, the most significant contribution to background is due to the X-ray tube spectrum scattered by the specimen especially when an unfiltered, or broadband, excitation spectrum is used on thick, low atomic-number specimens. Scattering of the Bremsstrahlung continuum (due to electron beam hitting the anode in the X-ray tube) leads to a high background level at all energies. Scattering of the characteristic anode lines from the specimen is also an important source of interference.

Since both coherent and incoherent scattering are involved, there is broadening of the characteristic lines, depending on the line energies and the spectrometer resolution. Frequently the X-ray tube spectrum contains unwanted characteristic lines from materials used in the anode and window construction. These lines become interfering peaks as they scatter from the specimen just like the major characteristic anode lines.

In the PIXE analysis, secondary electron bremsstrahlung (SEB) is the main cause of background. SEB is produced by the secondary electrons ejected from the target atoms due to the inelastic collision of the charged particle with the target nuclei and give rise to the continuous X-rays. The Bremsstrahlung produced is a continuous spectrum with intensity upward toward a high energy limit. The lower end of the spectrum is dominated by a Bremsstrahlung process giving rise to much greater intensities and results from electrons which are knocked on by the protons as they slow down in the target material. However the continuous spectrum produced by the inner-shell electrons is the dominant feature of the continuous nature of photon Bremsstrahlung energies of a few keV which is normally inseparable from the characteristic radiation.

The maximum energy of free electrons knocked on in this way is given by $T_{\max} = 4m M_1 E_1 / (m + M_1)^2$ where m is the mass of the electron; E_1, M_1 are the projectile energy and mass, respectively.

For $m \ll M_1, T_{\max}(\text{keV}) \cong 2E_1(\text{MeV})/M_1(\text{amu})$

The intensity of secondary Bremsstrahlung is proportional to Z_1^2 (projectile atomic number) and that it extends up to photon energies well above T_{\max} . To calculate SEB effect some knowledge of the energy distribution of knocked on electrons is needed. The number of secondary electrons with energies in excess of T_m falls off very rapidly with increasing electron energy. Above a few keV, the Bremsstrahlung produced by these secondary electrons is undetectable and only the projectile bremsstrahlung remains.

The cause of projectile Bremsstrahlung is the radiation of energy due to accelerated charged particles and the intensity of Bremsstrahlung is proportional to $(Z_1/M_1)^2$ which is considerably weaker than electron Bremsstrahlung. The background in the projectile target collision spectra due to Bremsstrahlung is classified into four categories:

1. *Secondary Electron Bremsstrahlung* (SEB) – cause of low energy background and is produced by the secondary electrons ejected from the target atoms during irradiations.
2. *Projectile Bremsstrahlung* (PB) of the bombarding particles slowed down in close collisions with the matrix nuclei.
The SEB is often six orders of magnitude larger than other sources of background while the PB is orders of magnitude less intense than electron Bremsstrahlung for X-ray energies below T_{\max} .
3. *Compton scattering*: In case of higher bombarding energies, the Compton scattering of X-rays from nuclear reactions between projectiles and matrix nuclei contributes to the background radiation. As an example, F and Na have very high cross-sections for (projectile, γ) reactions and the γ -rays produced by these reactions Compton (incoherently) scatter in the X-ray detector leaving only a small fraction of their energy with the recoiling Compton electron in the detector producing large high energy X-ray background, usually much stronger than the projectile Bremsstrahlung background. The energy at which the Compton edge (the maximum energy imparted to the recoil electron due to Compton interaction) occurs, is given by $E_c = 2\alpha E_0(1 + 2\alpha)^{-1}$, where E_0 is the energy of the X/ γ -rays incident on the detector and $\alpha = E_0/2m_0c^2$ where m_0c^2 ($= 511$ keV) is the energy equivalent to the rest mass of the electron.
4. *Background due to the insulating targets*: Insulating targets pose special difficulties because localized high voltages on the target surface accelerate free electrons, producing high background up to tens of keV X-ray energy.

1.8.2 Contribution of Scattering Geometry to Signal Background

1. In specimen having a high degree of crystal structure, interfering diffraction peaks become possible.
2. Background and contaminant lines can also be produced by the specimen chamber and the specimen holder, especially when very thin specimens are analyzed. This is because of the fact that the intensity contribution from the specimen itself will be very low.
3. Fluorescence of the chamber walls can provide contaminant lines which pass back through the thin specimen to the X-ray spectrometer. Radiation scattered from the chamber walls and the specimen holder can also increase the level of background.

The X-ray spectrometer itself contributes to the background. With the wavelength spectrometer, the most important contribution is due to the second and higher order diffraction.

1.8.3 Contribution of Detection System to Signal Background

With energy dispersive spectrometers, the detector system provides the limiting background contribution when monochromatic excitation is used for trace

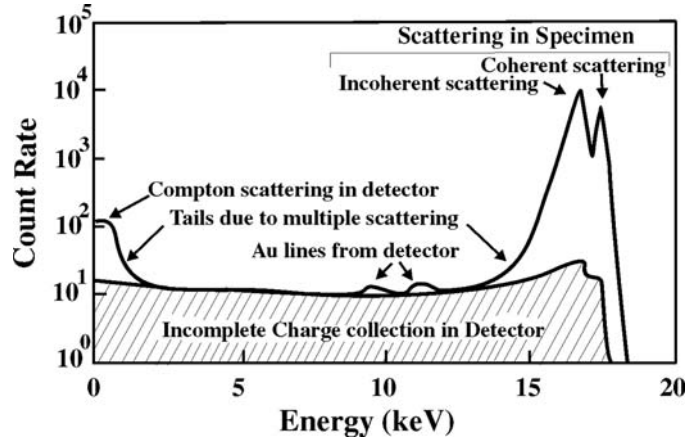


Fig. 1.23. Background contribution in the EDXRF spectrometer with monochromatic excitation at 17.4 keV

analysis. Figure 1.23 illustrates the effect on a pure-water specimen excited by monochromatic excitation i.e., 17.4 keV Molybdenum $K\alpha$ line from a graphite monochromator on a Molybdenum anode X-ray tube. The excitation X-rays are coherently and incoherently scattered from the water specimen to produce the intense peaks at 17.4 and 16.8 keV, respectively. The incoherent peak is much broader due to the range of scattering angles included about the nominal 90° scattering angle. The low-energy tail on the incoherent peak extending down to about 10 keV is primarily due to multiple Compton scattering in the specimen. The major background is due to incomplete charge collection in the Si(Li) detector which occurs because the holes and electrons produced in the detector by 16.8 and 17.4 keV X-rays combine before these are collected. The result is a pulse of abnormally low-amplitude recorded at a lower than normal energy. Some improvements can be gained by collimating the detector and using only the central 50% of its sensitive area.

Since the gold contact layer in front of the Si(Li) detector are fluoresced by the incoming X-rays, these cause the Au L and Au M X-rays lines in the EDXRF spectrum. The intensity of these lines is a function of the thickness of the gold contact layer and it may vary significantly from detector to detector. The gold L lines are often broadened on the high-energy side due to the ejected photoelectrons recoiling from the gold layer into the detectors' sensitive volume. The silicon escape peaks and the presence of sum peaks also cause hindrance to the analysis of X-rays spectra.

1.9 Methods for Improving Detection Limits

The minimum detectable amount is that concentration of the element that gives a net intensity (I_L) equal to three times the square root of the

background intensity $(I_B)^{1/2}$. In the case of X-ray tube exciter, the sensitivity can be greater if constant potential generator is used, kV and mA are as high as possible (but not to decrease I_L/I_B), target lines lie close to short-side of the absorption edge of its analytical line (usually a target just higher in Z number) and thin X-ray tube window is used.

Since the major background source limiting trace element analysis is the scattered X-ray tube continuum in XRF, a simple and effective means of removing this limitation is the use of a primary beam filter. If a thin aluminum filter is employed, the filtered X-ray tube spectrum of the chromium K-lines will strongly attenuate the chromium lines and all longer wavelengths allow the short-wavelength radiations. Thus a low background region is created for trace elements with longer wavelength. These elements will be excited by the shorter wavelength continuum passing through the filter. It is important to note that the sensitivity (m) for the trace elements will be reduced unless the tube current can be reduced to compensate. However the detection limit will be improved if the ratio $\sqrt{I_B}/m$ is reduced, which is possible depending on the choice of filter thickness.

In XRF, monochromatic excitation provides good trace sensitivity only over a restricted range of elements close to the selected excitation energy. This occurs because the cross-section for ionizing the appropriate shell in the atom decreases rapidly as the excitation energy is increased above the absorption energy of the analyte element.

Figure 1.24 illustrates the sensitive range for simultaneous trace element analysis as a function of monochromatic excitation energy. The bands are defined, one for the analysis of the $K\alpha$ line and the other for analysis of the $L\alpha$ line. The high atomic number boundary on each band is controlled by interferences with the incoherent scattered peak. The starting point is to assume that the highest energy line, which can be analyzed, is of the excitation energy and the absorption edge for this line must also be below the excitation

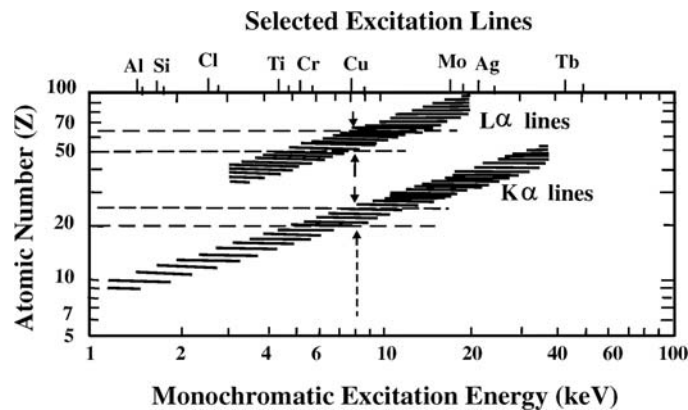


Fig. 1.24. Sensitive range for trace analysis with monochromatic excitation

energy. Thus the analysis of a wide range of elements will require several analyses with different excitation energies.

The thickness of the specimen is another important parameter. Although the detected intensity of the scattered excitation radiation is high with thick specimens yet it causes two problems. First, the maximum excitation intensity, which can be used, is limited by the counting rate of the scattered (coherent/incoherent) radiation rather than the analyte line, which limits the achievable sensitivity for the analyte line. Second, the intense high-energy scattered radiation produces a significant background under the analyte line due to incomplete charge collection in the Si(Li) detector, which increase the background. Both these effects combine to degrade the minimum detection limits. The thickness effect can be understood by maximizing the ratio of fluoresced intensity (I_i) to the scattered intensity (I_{sc}). An ideal situation is achieved by keeping the thickness (t) = 10% of infinite thickness t_∞ (t_∞ means $I_i = 99\%$); where an increase of tube current by only a factor of 7.3 over the thick-specimen case causes an improvement in detection limit by a factor of 3.4.

1.10 Computer Analysis of X-Ray Spectra

The X-ray full energy peaks from semiconductor detectors are generally described by Gaussian distribution, modified to allow for tailing. The peak fit to an element J is given by:

$$\text{PEAK}_j(x, H_j, \sigma, \mu) = H_j \exp[-1/2\{(x - \mu)/\sigma\}^2] \quad (1.58)$$

Here, x is the channel location at which the function is evaluated. H_j is the amplitude computed for the reference line of the element j . The symbols μ and σ represent the centroid and width, calculated at the X-ray energy of the line being fitted. The background points are chosen in selected channel regions by determining the local minimum for each region. The background fit at channel x is calculated (by second or third-order polynomial) as:

$$\text{BKGD}(x, P_y) = \exp(P_0 + P_1 \times x + P_2 \times x^2 + P_3 \times x^3) \quad (1.59)$$

The peak centroid (μ) and peak width (σ) are calculated according to the following linear calibration

$$\text{Peak centroid} = P_4 + P_5 \times E$$

and

$$\text{Peak width} = (P_6 + P_7 \times E)^{1/2} \quad (1.60)$$

Here E represents the appropriate energy corresponding to channel x , and P 's are the fitting parameters. The second of the equation gives the dependence

of resolution on noise and on the statistical nature of the charge formation. P_7 is related to P_5 by:

$$P_7 = P_5 \times F \times \varepsilon$$

where F is the Fano factor and ε is the energy to create one electron-hole pair in silicon.

The background fit BKGD (x, P_y) and the collection of peak fits $\sum_j \text{PEAK}_j(x, H_j, \sigma, \mu)$ are summed at each channel x to yield the total fitting function FIT (x, P, H_j), as:

$$\text{FIT}(x, P, H_j) = \text{BKGD}(x, P_y) + \sum_j \text{PEAK}_j(x, H_j, \sigma, \mu) \quad (1.61)$$

The least square fitting can be performed by the method of Marquardt which combines a gradient-type search for minimum χ^2 with linearization of the fitting function.

The exit from the iterative fitting loop is made automatic or manual when “ χ ” is less than 10^{-4} . For those elements which are not detected, the program can also provide the limit of detection (ppm) calculated as $3\sqrt{B/S}$, where B is the integrated background (i.e., nonpeak) count in a region centered at the computed centroid and having a width of one FWHM while S is the number of counts of elemental X-rays in the line.

From the estimates of the amplitudes H_j and width “ σ ” of the fitted peaks, the peak areas are computed as:

$$\text{AREA}_j = \sqrt{2\pi} \times \sigma \times H_j \quad (1.62)$$

which are converted to elemental abundances.

1.11 Some Other Topics Related to PIXE Analysis

1.11.1 Depth Profiling of Materials by PIXE

The most commonly used accelerator-based techniques for depth profiling are Rutherford Backscattering (RBS) which will be discussed in Chap. 2, Elastic Recoil Detection (ERD) which will be discussed in Chap. 3, and Nuclear Reaction Analysis (NRA) which will be discussed in Chap. 7. PIXE analysis has the advantage of a very good sensitivity and possible simultaneous detection of all heavier elements.

The X-ray yield from an infinitesimal volume at depth x , of the elements with $n(x)$ atoms per unit volume is given by:

$$dY = \frac{Q}{e} \times n(x) \times \sigma \left[E \left(E_1, \frac{x}{\cos \theta} \right) \right] dx \quad (1.63)$$

where E_1 is the energy of protons of energy E , bombarded under an angle θ , Q/e represents the proton flux and $\sigma[E(E_1, x/\cos\theta)]$ is the cross-section for proton energy $E(E_1, x/\cos\theta)$ at the depth $x/\cos\theta$. The fraction of X-rays emitted into the angle ϕ at which the detector with efficiency (ε) and solid angle (Ω) is positioned, is then given by:

$$dY = \frac{Q\varepsilon\Omega}{4\pi e} \times n(x) \times \sigma\left[E\left(E_1, \frac{x}{\cos\theta}\right)\right] \exp\left(-\frac{\mu x}{\cos\phi}\right) dx \quad (1.64)$$

where μ is the absorption coefficient of the considered X-rays. If we integrate (1.64) over the whole proton range, R , the expression for the total yield is obtained:

$$Y = K \int_0^{R\cos\theta} C(x) \times \sigma\left[E\left(E_1, \frac{x}{\cos\theta}\right)\right] \exp\left(-\frac{\mu x}{\cos\phi}\right) dx \quad (1.65)$$

where $C(x) = n(x)W/N_0$, W is the atomic weight of the element. N_0 is the Avogadro number and $K = Q\varepsilon\Omega N_0/4\pi\varepsilon\Omega$. For $C(x) = 1$, (1.65) presents the efficiency (α) of the PIXE for the thick-target measurements. From this equation, it can be seen that $C(x)$ profile can be obtained by varying the absorption or cross-section term. This can be done, for example by varying the proton energy or tilting the target.

For deconvolution of an unknown profile, we consider $C(x)$ as

$$C(x) = \Sigma C_j f_j(x) \quad (1.66)$$

where C_j are the components of the f -basis (step-like functions with edges determined by the proton ranges used).

If A_{ij} is the contribution of the X-ray yield of each slab with unit concentration of the element of interest and i corresponds to the i th energy used, then

$$i = \Sigma A_{ij} C_j \quad (1.67)$$

where

$$A_{ij} = K \int_{x_{j-1}}^{x_j} \sigma\left[E\left(E_1, \frac{x}{\cos\theta}\right)\right] \exp\left(-\frac{\mu x}{\cos\phi}\right) dx \quad (1.68)$$

For imaging of different elements in PIXE analysis (which is needed to locate the distribution of elements since the composition varies with position across an image area), there will be variation in the X-ray yields i.e., counts ppm⁻¹. This effect can be corrected using a method based on combining the yields calculated for end-member components in order to make dynamic analysis for quantitative PIXE (Ryan 2001).

1.11.2 Proton Microprobes

Proton microprobes represent a natural evolution of the PIXE analysis work which seek smaller area beams for lowered minimum detectable mass levels and allows an expansion of such analyses to encompass even the spatial

distribution of elements in specimens. Beams of MeV ions, with diameters below $100\text{ }\mu\text{m}$, can be prepared by either collimation or ion focusing. Using quadrupole lens with cylindrical form of pole tips, the beam size of $2 \times 2\text{ }\mu\text{m}^2$ and stability of better than $1\text{ }\mu\text{m}$ has been attained. The focusing arrangement (four magnetic quadruples) allows equal magnification in both places from an object slit. The current density ranges from $5\text{--}20\text{ pA }\mu\text{m}^{-2}$ at initial beam currents between 1 and $3\text{ }\mu\text{A}$. It has been used for surface analysis of lunar samples, monazite crystals, mica foils and meteorites. In general the proton microbeam arrangement can be used to study distribution of elements in surfaces in one of the following ways:

- Charged particles activation analysis for light elements e.g., oxygen, carbon, nitrogen, and fluorine.
- Proton-induced X-ray technique (PIXE) for elements heavier than ^{11}Na .
- Rutherford – scattering from heavy elements in light matrices.
- Determination of foil thickness through activation methods.

The sensitivity of 10–100 ppm has been obtained for a current of 1–100 nA by using the microbeam.

1.11.3 Theories of X-Ray Emission by Charged Particles

The ionization mechanism of X-rays induced by charged particles is of three kinds (1) Coulomb ionization (2) electron capture, and (3) electron Promotion.

Coulomb Ionization

According to direct Coulomb ionization models (valid for $Z_1 \ll Z_2$ and $v_1 \geq v_2$), the ionization cross-section for a certain shell becomes maximum when the reduced energy $E/(\lambda U)$ is equal to unity. Here λ is the mass of projectile in electron mass unit and U is the average binding energy of the shell. The direct Coulomb ionization phenomenon is described by the following approximations:

Binary Encounter Approximation (BEA)

This theory (Garcia 1970) is based on the classical energy transfer process wherein a projectile interacts with an inner-shell electron having a velocity distribution representative of its binding energy.

Semiclassical Approximation (SCA)

Bang and Hansteen (1959) and later Hansteen and Mosebekk (1973) treated the ion–atom collision process in a semiclassical approximation, considering the projectile motion classically and the transition of the inner-shell electron to the continuum quantum mechanically.

Plane Wave Born Approximation (PWBA)

In this approximation, the incident charged particles are treated as plane waves whereas the target electrons are described by hydrogenic wave function. The interaction between the projectile and the electron is treated to first order (Merzbacher and Lewis 1958).

Perturbed Stationary State Theory with Energy loss, Coulomb deflection, and relativistic effects (ECPSSR)

The PWBA theory has the validity for highly asymmetric collisions ($Z_1 \ll Z_2$). For nearly symmetric collisions, where PWBA theory is no longer valid, the perturbation of the target electronic states by the presence of the projectiles, disturbances to the projectile motion by the Coulomb deflection caused by the target nucleus and the relativistic motion of the target electrons are some of the corrections which have been introduced (Brandt and Lapicki 1979, 1981).

Electron Capture

The ionization of a target atom by a moving ion proceeds not only through direct ionization to the continuum but also through the electron capture by the projectile. Electron capture is the process in which one or more nonradiative electrons are captured while a fast highly stripped projectile passes through the electron cloud of the target. It is dominant for the systems with $Z_1 = Z_2$ and $v_1 \approx v_{2s}$. The Theory for electron capture is known as Oppenheimer, Brinkman and Kramer formalism followed by modification by Nikolaev (OBKN approximation).

Electron Promotion

In electron promotion, the electron is ejected through the quasimolecular orbital formed during ion-atom collision (Fano & Lichten 1965). This mechanism becomes dominant when $Z_1 \approx Z_2$ and $v_1 \ll v_2$, where v_1 and v_2 are velocities of the projectile and the bound electron in the target atom, the observed cross-sections for inner-shell ionization become many order of magnitude larger than predicted by any theory. The reason ascribed is the electron promotion via crossing molecular orbitals (MO). In this MO model (Fano and Lichten 1965, Kessel (1971), Saris (1971), Taulberg et al. 1975, Mokler and Folkmann 1978, Anholt 1979), as the nuclei approach, all shells of both atoms are involved and the energy levels move over to levels appropriate to the “quasimolecule” formed by the two atoms. In other words, the colliding atoms are treated as diatomic molecule whose interatomic separation varies during the collision. At sufficiently close distances of approach, the levels become those of an atomic number $Z_1 + Z_2$. At intermediate separation

new X-rays seen from neither atom individually, may appear. The molecular quantum numbers, having little importance for the widely separated atoms, become dominating factors as the collision brings the nuclei close together. In general, the energy levels change adiabatically as the two atoms approach, but some electrons from lower orbitals may be promoted to higher levels (electron promotion), leaving vacancies in the inner-shells as the atoms recede. This will happen only if there is a matching of an inner-shell energy level of the projectile with any inner-shell of the target atom.

Earlier the MO model was applied to the symmetric systems like Ar–Ar, Ne–Ne, etc. which was latter extended to the asymmetric systems like Cu–Ar, Al–Ar, etc. with the condition that an MO must have the same values of the $(n-l)$ in both the united atom (UA) and separated atoms (SA) limits. This is due to the reason that swapping takes place when two SA energy levels with the same values of m and $n-l$ change their relative order on an energy level diagram (Barat and Lichten 1972). To substantiate the theoretical model, the experimental measurements relating to molecular orbital formation in different asymmetric systems have been done by Mokler (1972), Anholt (1979), Montenegro and Sigaud (1985), Anholt et al. (1986).

Introducing two general parameters, the asymmetry parameter $\alpha = Z_1/Z_2$ and the adiabaticity parameter $\eta = (v_1/v_2)^2$ (where v_1 is the collision velocity and v_2 is the orbital velocity of the electron in the inner-shell of concern), the inner-shell vacancy production mechanism has been divided into two general categories by Madison and Merzbacher (1975) – the region for “direct coulomb ionization” $\alpha \ll 1$ and the regime for “quasimolecular excitation” $\alpha \approx 1$ and $\eta \ll 1$ as shown in Fig. 1.25. The third region with $\alpha \gg 1$ is the region for the production of multiply charged target recoil ions, a direct Coulomb ionization mechanism. This is due to the fact that the projectile

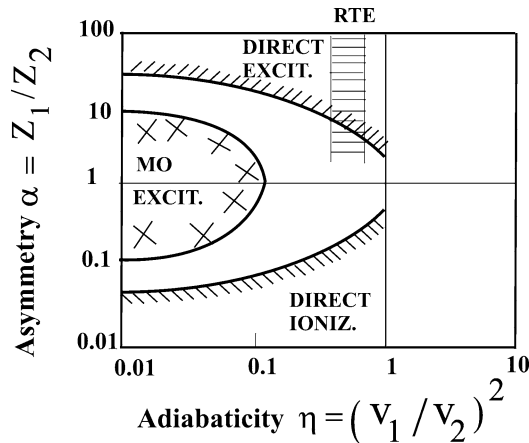


Fig. 1.25. Schematic representation of the main inner-shell processes for heavy ion-atom collisions and their applicability regions

ions will be having only the inner-shell electrons (and no outer-shell electrons as the heavy projectiles are highly ionized up to $\eta = 1$ due to stripping during the acceleration process) and one may detect excitation processes in the projectile and not an ionization or loss process. On the other hand, capture to empty projectile states – which is normally not possible for the neutral target atom – may also yield X-ray emission. Among these, the important capture processes are the (1) collision electron capture (CEC) to excited projectile states which can decay to by X-ray emission to the ground state; (2) radiative electron capture (REC) into ground or excited projectile states; the excited states decay additionally by X-ray emission; and (3) resonant electron capture (transfer) and excitation (RTE).

1.12 Applications of XRF and PIXE Techniques

Energy dispersive X-ray fluorescence (EDXRF) and particle-induced X-ray emission (PIXE) systems are particular appropriate for the analysis of geological, environmental, metallurgical, ceramic, and a wide range of other inorganic materials. Both techniques offer rapid, nondestructive analysis of test materials presented as solids, powders, particular collected on filter substrates and liquids. Since the X-ray fluorescence yield and detector efficiency are lower for light elements, EDXRF and PIXE are most often used for the analysis of elements in the range $11 < Z < 92$. PIXE is a very sensitive analytical technique (for the most of elements and samples limits of detection are of the order of 1 ppm) because of very high X-ray yields. PIXE method has been used in collaboration with scientist working in biology, and archaeology and other disciplines to obtain concentrations of micro and macroelements of the given sample. Several artifacts have been measured using PIXE method with different instruments. If a small part of the sample had to be investigated, the nuclear microprobe (with which the ion beam can be focused down to $1 \times 1 \mu\text{m}$) is applied. In case of large objects which can not be placed into vacuum chambers, the ion beam are extracted out through a thin foil and the samples are studied in helium atmosphere.

A survey of PIXE programs-1991 by Cahill et al. (1991) indicate that PIXE has been used in three major types of programs biological-medical (23%), material (21%) and aerosols (17%). Archaeological, mineralogy and others including Forensic sum to 22% of all programs.

1.12.1 In Biological Sciences

Both XRF and PIXE techniques are extensively used in biological and medical sciences for elemental analysis because of their ability in ultratrace analysis of K, Ca, Mn, Fe, Cu, Zn, Se, etc. in organic material. The bulk of living matter consists of the 11 major elements H, C, N, O, Na, Mg, P, S, Cl, K, and Ca.

Trace elements are heavy atoms linked to organic compounds by coordination or covalent bonds; these are Fe, I, Cu, Mn, Zn, Co, Mo, Se, Cr, Sn, V, F, and Si. Except for F, all these elements can be detected by XRF/PIXE. Trace elements in living matrices are not often coincidental contaminants but fulfill important functions. The presence of heavy metals in lumps, cryptogram, mosses, and lichens has been recognized and they are used as bio-indicators. Many of these elements can be detected by atomic absorption (AA) or by specific electrodes but using XRF/PIXE, no chemical separation is necessary. Using PIXE techniques, it may not be possible to identify light elements like C, N, O, F, Na but it is certainly possible by the other accelerator-based techniques like nuclear reactions.

The biological samples are either solid (bones, finger nails, teeth, hair, etc.). In such cases, no preceding preparation is required. In case of soft tissues and liquids (blood, urine, etc.), preceding preparation like freeze-drying or wet-ashing (with addition of internal standards) is required before doing the analysis. A restriction in the analysis of biological samples is sometimes the dimensions where the investigations are performed at the cellular level (size of the cell $\sim 10\ \mu\text{m}$). In this case microbeams $\sim 5\ \mu\text{m}$ in diameter or less can be used. Due to the biodiversity of organic samples, high number of samples is required to make statistical analysis. Walter et al. (1974) has described the analysis of biological, clinical, and environmental samples using proton-induced X-ray emission. Hall and Navon (1986) used 4.1 MeV external proton beam to simultaneously induce X-ray emission (PIXE) and γ -ray emission (PIGE) in biological samples that included human colostrum, spermatozoa, teeth, tree-rings, and follicular fluids. The analytical method was developed to simultaneously determine the elements lithium ($Z = 3$) through uranium ($Z = 92$) in the samples.

The use of PIXE for the analysis of botanical samples, determination of proteins and amino acids, Hair analysis, detection of trace elements in liquids (blood, serum, etc.) and in tissues (muscles, fibers, bones, teeth, etc.) has been described by Deconninck (1981). Hair is either individually analyzed by placing it on aluminum frame or a given mass of quantity of strontium nitrate can be added to it as internal standard. From this solution, the sample on nucleopore filter is prepared using a micropipette. The frozen samples of liver and spleen of about $\sim 10\ \mu\text{m}$ thickness, deposited on a thin Formvar film of less than $\sim 10\ \mu\text{g cm}^{-2}$ covering the glass plate, have also been studied. A typical PIXE spectrum of human teeth is as shown in Fig. 1.26. Among other biological samples, fish, mice, leaves and algae have been studied. Lowe et al. (1993) used PIXE for tissue analysis in a toxicity-disposition study of renal slices exposed to HgCl_2 , CdCl_2 , $\text{K}_2\text{Cr}_2\text{O}_7$, or NaAsO_2 alone or in a mixture. Characterization of Fe, Cu, and Zn has been reported in a recent study by Zhang et al. (2006) in organs of PDAPP transgenic mice, which express the familial Alzheimer's disease (AD) gene using XRF spectrometry.

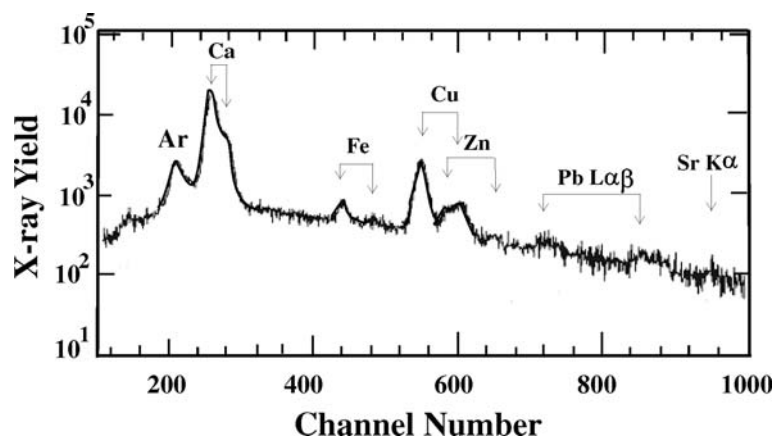


Fig. 1.26. Typical PIXE spectrum of human teeth

1.12.2 In Criminology

PIXE has been successfully applied to the problem of residues from gun firing. Certain elements including S, Ba, Fe, and Pb have been detected in significantly larger amounts on firing hands, than on nonfiring hands. Other elements such as K, Ca, Sb, Cr, Mn, Ni, and Cu have also been detected in the residue from firing arms. The technique used is to rinse hands with dilute nitric acid, to concentrate by evaporation and to place drops of liquid on a piece of Kapton foil which is bombarded with proton beam. Rožic et al. (2005) have determined the concentrations of the elements Pb, Rb, Sr, Y, Zr, K, Ca, Ti, V, Cr, Mn, Fe, Ni, Cu, Zn, and Co in the ash-samples of writing, copying and computer printing papers by EDXRF. Ashes of copying papers printed with black toner and black ink by laser and ink-jet printers were also analyzed. Most of the elements measured in papers showed the lowest concentrations in the ashes of Copier papers contains significantly higher amount of lead, strontium and zirconium compared to the papers of other manufactures. The concentrations of the elements Co, Mn, Fe, Cr, and Ti in the paper printed by laser printers are significantly higher compared to the nonprinted papers.

1.12.3 In Material Science

PIXE analysis method has been applied primarily for the nondestructive elemental analysis of ancient copper coins. However, the high yields of the copper X-rays and the high background which is created, cause serious difficulties in the accurate determination of zinc, nickel, iron, and in general for the elements with medium and low atomic numbers (Katsanos et al. 1986). For this reason, the complementary methods of proton-induced prompt γ -ray emission and proton activation methods have been explored. PIXE has been used in

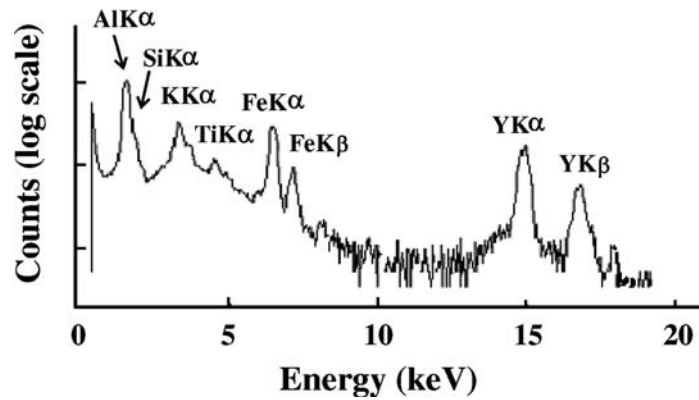


Fig. 1.27. A typical PIXE spectrum of Sialon, a type of ceramic containing Si, Al, O, and N

some of the key areas like study of corrosion and erosion and the study of high-temperature semiconductors based on ceramics with oxides of rare earth elements. Figure 1.27 shows the typical PIXE spectrum of Sialon (general sample composition: Si, Al, O, and N – Sialon is a type of ceramic used for high temperature applications) indicating the presence of the major as well as the minor elements.

The use of nondispersive X-ray fluorescence spectroscopy has been well established as an analytical technique for many problems in alloy analysis and coating thickness measurements in basic metal industry, but the highest excitation efficiency is achieved when the entry of the exciting radiation is restricted to an energy, which is just above the absorption edge of the “wanted” elements. A characteristic line of the substrate material is chosen and its attenuation by the overlaying material helps to determine the thickness. For example, in a tin plated steel, it is possible to measure the ratio of FeKα from a coated and uncoated specimen in order to determine the thickness of tin.

The problem of interelement effects in complex materials (ferrous and non-ferrous metals) is particularly significant. Several hundred alloy compositions exist and the most important alloying elements include Ti, V, Cr, Mn, Fe, Ni, Cu, and Zn which are virtually adjacent in atomic number and several of these elements may occur together in a single alloy. The greatest advantage is obtained when measuring the concentration of a single element at low concentration in a matrix of higher atomic number e.g., Cr in steel. The analyses of steels (Mn, Cr, and V in carbon and low alloy steels), brasses (Mn, Ni, and Fe in brasses) and aluminium alloys (Si, Cr, Mn, Fe, Ni, Cu, Zn) have been successfully carried out and reported by Clayton et al. (1973). Figure 1.28 shows the EDXRF analysis of a sample containing ^{26}Fe , ^{27}Co , ^{28}Ni , and ^{29}Cu (transition elements) from their Kα X-ray peaks.

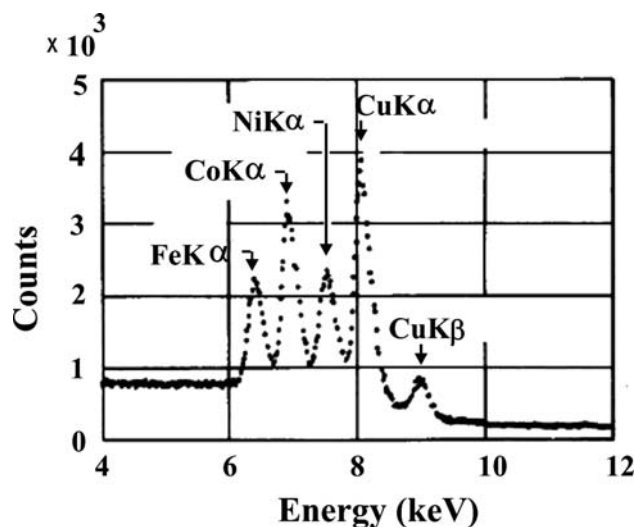


Fig. 1.28. EDXRF analysis of a sample containing Fe, Co, Ni, and Cu K α X-ray peaks

The comparison of results obtained from measurements on nickel-base alloys using the laboratory-based WD-XRF vs. portable ED-XRF spectrometer has been made by Zwicky and Lienemann (2004). Their comparison shows that the semiquantitative analyses using the WD-XRF spectrometer can be accepted as quantitative determinations. Although the portable EDXRF spectrometers are good enough for field investigations, the results obtained using these do not meet the quality requirements of laboratory analysis. For determining the composition of two- and three-component alloys of some technological materials, Mukhamedshina and Mirsagatova (2005) employed various X-ray fluorescence techniques. It has been found experimentally and confirmed theoretically that in some alloys, the composition can be determined without taking into account the absorption and secondary excitation of analytical characteristic lines, indicating that the contributions of these effects are opposite.

1.12.4 Pollution Analysis

The energy dispersive X-ray fluorescence (EDXRF) and particle-induced X-ray emission (PIXE) are the most widely used techniques for quantification of various elements present in aerosol samples. The population living in proximity to the industries and increased vehicular traffic are exposed to relatively high levels of air and water pollution. Numerous workers have studied the air and water samples by XRF and PIXE techniques for pollution monitoring, since the assessment of pollutant elemental levels and identification of their sources is prerequisite for understanding their effect on human health.

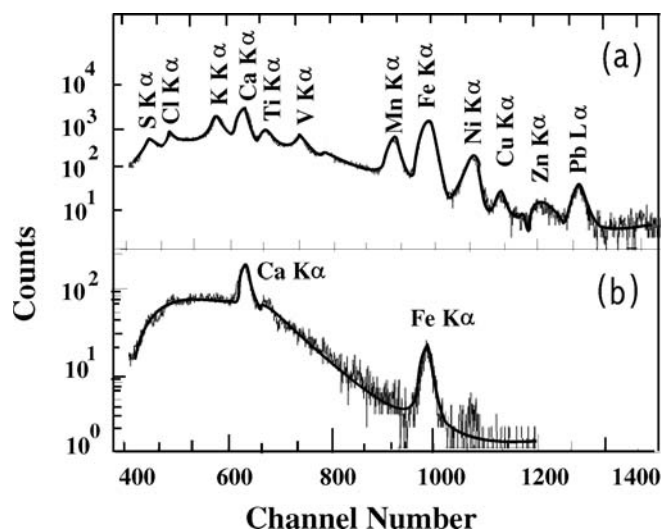


Fig. 1.29. (a) A typical PIXE spectrum of an aerosol sample and (b) the background spectrum from blank filter

In a study conducted at Chandigarh by Bandhu et al. (2000), Aerosol samples were collected on 0.8 μm pore size using cellulose nitrate filter, were mounted on Millipore aerosol standard filter holder. The air through the filter paper sucked with the help of Millipore diaphragmatic vacuum pump. Sixteen elements namely S, Cl, K, Ca, Ti, V, Cr, Mn, Fe, Ni, Cu, Zn, Br, Rb, Sr, and Pb have been detected. The air around Chandigarh is found to contain relatively more concentration of Fe, Ca, and Ti and very small amount of Ni and Cu. The typical spectra from aerosol sample along with the spectrum from blank filter measured by the PIXE and EDXRF are as shown in Figs. 1.29 and 1.30.

For PIXE analysis, carbon foil of $\sim 10 \mu\text{g cm}^{-2}$ can be chosen as a matrix to make a self supporting target for water samples. The floating of the carbon foils is done in the water sample (which is to be analyzed) to assure the homogeneity in distribution of the trace elements. The water samples can also be prepared by depositing a few microliters on aluminized mylar or by filtering a pre-concentrated sample on nucleopore filter. Pre-concentration is performed by taking 50 ml of each sample and adding 100 μl of Pd ($1000 \mu\text{g ml}^{-1}$) for internal standard. The solution is kept at pH 9 by adding NH_4OH . The metals are then precipitated as carbonates adding 1 ml diethyldithio carbonate (NaDDTC) solution. Pd diethyldithio carbonate is also formed in this reaction which is a stable complex and acts as a good co-precipitating agent. The precipitates thus obtained are collected by filtering on Nucleopore polycarbonate filter (pore size 0.4 μm , thickness 10 μm).

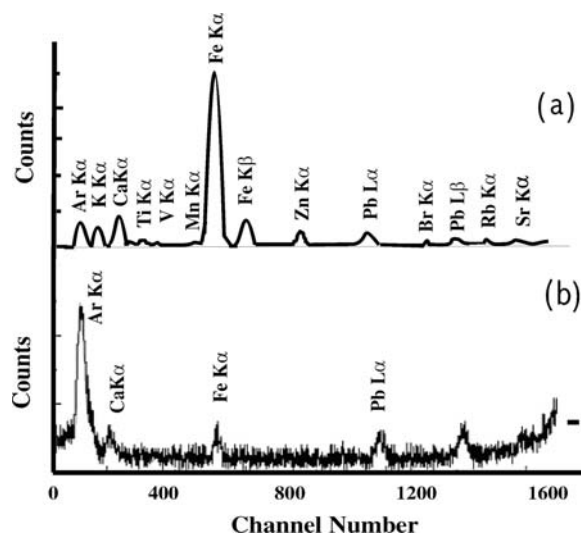


Fig. 1.30. (a) A typical EDXRF spectrum of aerosol sample and (b) the background spectrum from blank filter

Energy dispersive X-ray fluorescence (EDXRF) technique has been employed by Joshi et al. (2006) to determine the concentrations of different elements in water samples collected from different locations of famous Nainital Lake including tap water and spring water sample from Nainital (Uttaranchal). Lake Nainital is a constant source of drinking water for local people as well as tourists. A chelating agent (NaDDTC) was used for the preconcentration of the trace elements. Seventeen elements were detected. The concentrations of Na, Si, K, V, Cr, Mn, Fe, Co, Ni, Cu, Zn, As, Ag, Pb, and Bi were found to be within BIS/WHO limits.

1.12.5 For Archaeological Samples

A reliable knowledge of the composition of archaeological objects for major and trace elements is of primary interest for the archaeologists. The composition of the metal artifacts gives information on the ancient technological knowledge and helps to distinguish between prehistoric cultural traditions. Analytical work on gold jewellery of archaeological interest has been performed by Demortier (1996) with an emphasis to solders on the artifacts and to gold plating or copper depletion gilding using PIXE along with other ion-beam analytical techniques like RBS, NRA, and PIGE. On the basis of elemental analysis, these authors have identified typical workmanship of ancient goldsmiths in various regions of the world: finely decorated Mesopotamian items, Hellenistic and Byzantine craftsmanship, cloisonne of the Merovingian period, depletion gilding on Pre-Colombian tumbaga. Pieces of bronzes from two preroman sites in Spain with different cultural traits have been analyzed

by PIXE along with other ion beam analytical techniques like PIGE and RBS) and Auger electron Spectroscopy (AES) by Clement-Font et al. (1998) to extract complementary information on elemental composition and chemical state.

Motivated by the spread of Italian glass-working technology into central Europe, Šmit et al. (2000) conducted systematic investigation of the 16th century glasses of Ljubljana by using EDXRF and external beam PIXE methods due to their nondestructiveness. The manufacturing procedures were indicated by the Rb/Sr content in the glass i.e., the investigated glasses were mainly produced with the ash (not potash) of halophytic plants. PIXE analysis has been carried out by Río et al. (2006) on several mural paintings containing Maya blue from different Prehispanic archaeological sites (Cacaxtla, El Tajín, Tamuin, Santa Cecilia Acatitlán) and from several colonial convents in the Mexican plateau (Jiutepec, Totimehuacán, Tezontepec and Cuauhtinchán). The analysis of the concentration of several elements permitted to extract valuable information on the technique used for painting the mural, usually fresco. The trace element and Sr isotopic compositions of stoneware bodies made in Yaozhou and Jizhou were measured by Li et al. (2005) to characterize the Chinese archaeological ceramics and examine the potential of Sr isotopes in provenance studies. In contrast, $^{87}\text{Sr}/^{86}\text{Sr}$ ratios in Yaozhou samples have a very small variation and are all significantly lower than those of Jizhou samples, which show a large variation and cannot be well characterized with Sr isotopes. Geochemical interpretation reveals that $^{87}\text{Sr}/^{86}\text{Sr}$ ratios will have greater potential to characterize ceramics made of low Rb/Sr materials such as kaolin clay, yet will show larger variations in ceramics made of high Rb/Sr materials such as porcelain stone.

From the analysis of several archaeological samples by micro-PIXE, Neff and Dillmann (2001) have shown that ores containing important amount of phosphorus were used in ancient Europe to obtain iron by two different processes called the direct one and the indirect one. Phosphorus content was quantified as the heterogeneous phosphorus distribution was observed in the samples. The results confirm the fact that refining of phosphorus pig iron was possible with ancient refining processes. Moreover it seems that the phosphorus distribution ratio could be a discriminating factor to identify the iron making process.

Kumar (2002) has analyzed the pottery samples of Harrapan period collected from Sanghol (Dist. Ludhiana, Punjab, India). The absolute elemental concentration measurements were made by EDXRF measurements using Montanosoil and Brick clay as standards. The typical spectrum of pottery samples is shown in Fig. 1.31.

On the other hand, a typical PIXE spectrum of 13th century Iranian bowl taken in air using external beam is presented in Fig. 1.32. The two peaks each corresponding to Fe and Cu are their $K\alpha$ and $K\beta$ peaks, while the three peaks corresponding to Pb are its $L\alpha$, $L\beta$, and $L\gamma$ peaks. The presence of Argon peak in the spectrum is noteworthy.

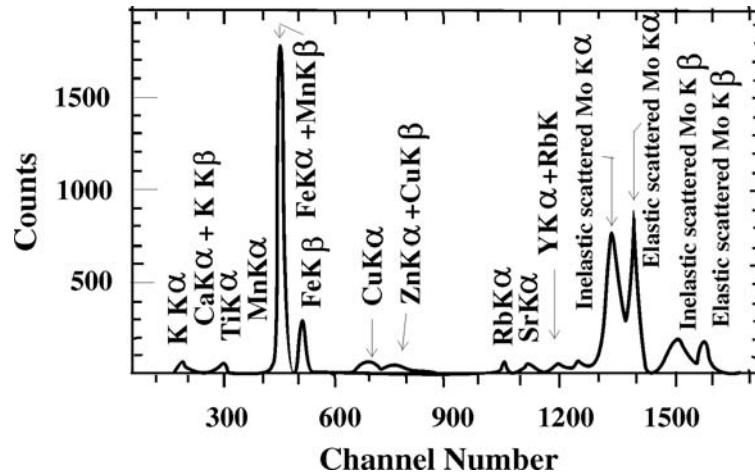


Fig. 1.31. Typical spectrum of pottery samples of Harrapan period collected from Sanghol (Kumar 2002)

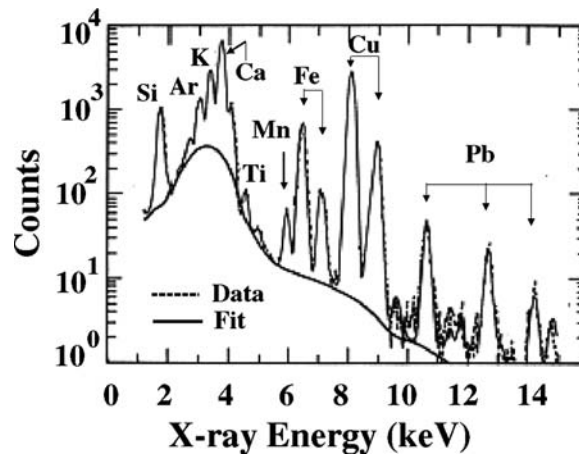


Fig. 1.32. A typical external beam PIXE spectrum of 13th century Iranian bowl taken in air. Note the presence of Argon (Ar) peak

Using a portable beam stability-controlled XRF spectrometer, Romano et al. (2005) have determined the concentrations of Rb, Sr, Y, Zr, and Nb in 50 fine potsherds from the votive deposit of San Francesco in Catania (Italy) by using a multilinear regression method in their bid for quantitative nondestructive determination of trace elements in archaeological pottery. A small portion of a few potsherds was even powdered in order to test the homogeneity of the material composing the fine pottery samples and the XRF data were compared with those obtained by chemical analysis of the powdered samples.

1.12.6 For Chemical Analysis of Samples

The X-rays emitted from valence band exhibit intensity, wavelength and line-shape changes as a function of the chemical composition. Thus XRF is a probe to examine the chemical state of the atoms (hence the electronic structure) on the surface. For example, XRF can help to determine the coordination number of Si-atoms in complex silicates by measuring the wavelength shift of the SiK α . X-ray fluorescence has been used to find the chemical composition of pigments and to analyze corrosion layers in-situ. Kawatsura et al. (2001) have used a wavelength-dispersive X-ray spectrometer system for particle-induced X-ray emission for chemical state analysis for various compound materials. High-resolution CuL $\alpha_{1,2}$ and L β_1 X-ray spectra from Cu, Cu₂O, and CuO targets are measured using this spectrometer system. The incident microbeam is focused 2.0 MeV protons with a beam size of $100 \times 30 \mu\text{m}^2$. The Cu L X-ray spectrum shows two main peaks and their satellites clearly. The main peaks are the L $\alpha_{1,2}$ and the L β_1 diagram lines, respectively. Due to a high detection efficiency of this spectrometer equipped with a position sensitive detector for soft X-rays, the intensity ratio L β_1 /L $\alpha_{1,2}$ is observable, which is the lowest for pure Cu metal, and the largest for CuO. Moreover, the L $\alpha_{1,2}$ X-ray spectrum for CuO shows a large shoulder at the high energy side of the main peak, which is considered to be due to the chemical bonding between Cu and O atoms.

Maeda et al. (2002) have developed a crystal spectrometer system for rapid chemical state analysis by external beam particle-induced X-ray emission. The system consists of a flat single crystal and a five-stacked position sensitive proportional counter assembly. Chemical state analysis in atmospheric air within several seconds to several minutes is possible. A mechanism for time-resolved measurements is installed in the system. Performance of the system is demonstrated by measuring the time-dependence of chemical shifts of sulfur K $\alpha_{1,2}$ line from marine sediment and aerosol samples. Earlier, Maeda et al. (1999) used a flat analyzing crystal and a position sensitive proportional counter to measure line shifts (with the precision of 0.1 eV) of Si K α and P K α X-rays from various samples for chemical state analysis of minor elements.

1.12.7 For Analysis of Mineral Samples

Proton-induced X-ray emission (PIXE) technique has been used to determine the distribution of minor and trace elements in magmatic Ni–Cu ores, volcanogenic massive sulphide Cu–Pb–Zn–(Ag–Au) ores and lode Au–(Ag) deposits. Minor elements of importance include possible by-products or co-products of metal refining, as well as deleterious impurities in mill-feed, e.g., Cd, In, Sn, As, Se, Te, Tl, and Hg. Weathering products of primary sulphide mineralization, including tropical laterites and other oxidized assemblages, were analyzed by Wilson et al. (2002) and found to contain a wide range of minor elements which reflect the bedrock style of mineralization. The iron

oxyhydroxide goethite, α -FeO(OH), contains trace levels of many elements, and in some cases 1 wt.% or more of base metals and arsenic, elements which are invisible in reflected-light microscopy. Other metals such as Ag are of sporadic occurrence in oxidized ores: they may be found as discrete mineral species, not incorporated into the dominant oxyhydroxides. The analysis of rare-earth bearing minerals has been done by Choi et al. (1996) using PIXE technique.

1.13 Comparison Between EDXRF and WDXRF Techniques

1.13.1 Resolution

Resolution is a very important parameter which describes the width (FWHM) of a spectral peak. The lower the resolution, the more easily an elemental line is distinguished from other nearby X-ray line. The resolution of the WDXRF system, which is dependant on the crystal and optics design, particularly collimation, spacing and positional reproducibility, varies from 2 to 10 eV at 5.9 keV. While the resolution in WDXRF depends on the diffracting crystal, the resolution of the EDX system is dependent on the resolution of the detector. This can vary from 150–200 eV for Si(Li) and HpGe and about 600 eV or more for gas filled proportional counter at 5.9 keV.

1.13.2 Simultaneity

EDXRF has the capability to detect a group of elements all at once while it is not possible with the WDXRF system.

1.13.3 Spectral Overlaps

Since the resolution of a WDXRF spectrometer is relatively high, spectral overlap corrections are not required. However, with the EDXRF analyzer, some type of deconvolution method must be used to correct for spectral overlaps as it has poor resolution. The spectral deconvolution routines however, introduce error due to counting statistics for every overlap correction onto every other element being corrected for. This can double or triple the error.

1.13.4 Background

The background radiation is one limiting factor for determining detection limits, repeatability, and reproducibility. Since a WDXRF system usually uses direct radiation flux, the background in the region of interest is directly

related to the amount of continuum radiation. However, the EDXRF system uses filters and/or targets to reduce the amount of continuum radiation in the region of interest, which is also resolution dependant, while producing a higher intensity X-ray peak to excite the element of interest. Thus although the WDXRF has an advantage due to resolution yet it suffers due to large background i.e., if a peak is one tenth as wide, it has one tenth the background. However, EDXRF counters with filters and targets can reduce the background intensities by a factor of ten or more.

1.13.5 Excitation Efficiency

Excitation efficiency is the main factor for determining detection limits, repeatability, and reproducibility. The relative excitation efficiency is improved by having more source X-rays closer to but above the absorption edge energy for the element of interest. WDXRF generally uses direct unaltered X-ray excitation, which contains a continuum of energies with most of them not optimal for exciting the element of interest. However, EDXRF analyzers may use filter to reduce the continuum energies at the elemental lines, and effectively increase the percentage of X-rays above the element absorption edge.

1.14 Comparison Between XRF and PIXE Techniques

Penetration Depths and Analytical Volume

The penetration depths and irradiation areas are totally different in PIXE and XRF. In XRF penetration depths are relatively large, of the order of a few millimeters while in PIXE analysis, the analytical depths are $\approx 10\text{--}50\ \mu\text{m}$ because of the limited penetration of particles into the sample. Therefore PIXE analysis is essentially a surface technique even when applied to “thick” samples.

Excitation and Background Intensity

The background intensity distribution in XRF and PIXE spectra are opposite to each other (see Fig. 1.22) due to its dependence on the excitation cross-section. The PIXE excitation and ionization cross-sections of various elements decrease with increasing atomic number, while in X-ray photon excitation, the cross-section increase with increase atomic number. Since detection limits are largely controlled by the background intensity, EDXRF is a better technique for the determination of elements with low energy X-ray lines which fall especially in the range of 1–4 keV (Na through Ca), while PIXE is better for elements with relatively higher characteristic X-ray energies. For elements with atomic number greater than ≈ 50 , both techniques are forced to use L X-ray lines in place of K X-ray lines.

Energy Resolution

At energies lower than 20 keV, better energy resolution (FWHM) is achieved with wavelength dispersive X-ray fluorescence (WDXRF) as compared to proton-induced X-ray emission (PIXE) and energy dispersive X-ray fluorescence (EDXRF). While the FWHM using Si(Li) detector is ~ 160 eV, it is < 10 eV for WDXRF at 5.9 keV. Depending on the collimator (fine/extra-fine) and order of diffraction (first/second), the FWHM varies from 10 eV to 50 eV for LiF(220) crystal and from 10 eV to 70 eV for LiF(200) crystal at about 12 keV. However, the energy resolution with LiF(200) crystal is approximately equal to that of a Si(Li) detector system at energies around 20 keV.

Lower Limits of Detection

Since XRF and PIXE spectra have their low background regions at opposite parts of the spectrum, this condition raises the minimum detectable concentration for the lower- Z regions of each excitation group in XRF, whereas in PIXE the limits are raised for the heavier elements within each group detected by the various proton energies. These trends make XRF more favorable for elements having their absorption edges close to the exciting energies. They provide a great advantage, e.g., in the analysis of Ba and Ti, employing a fluoresce plate of rare-earth element heavier than Ce would yield a rather high sensitivity for $K\alpha$ (Ba).

In PIXE analysis, using proton beam of 1-3 MeV for most favored elements in low- Z matrices and thin targets, the best sensitivities down to 0.1 ppm have been obtained. These levels are achieved for elements near $Z = 40$ using K lines and $Z = 80$ using L lines. For elements with Z values different from 40 and 80 the LLDs increase rapidly to ~ 100 ppm and are > 100 ppm for $Z < 20$. For thick targets and $Z < 20$ most matrices yield LLDs that are generally lower than 100 ppm and can be as low as 1 ppm under favorable conditions (absolute detection limits down to 10^{-12} g and relative detection limit down to $0.1 \mu\text{g g}^{-1}$). Compared to XRF, the detection limit offered by PIXE is better by one order of magnitude.

Similar LLDs are found in XRFs although LLDs for $Z < 20$ are very much lower than those attainable by PIXE. Using WDXRF it is now possible to obtain LLDs in the range of 50–200 ppm for elements F through B.

Flexibility

Since the equipment used in XRF technique including radioisotope source is portable, the energy dispersive XRF spectrometers are used in various divergent fields like that in the metal industry, in gold mines, in oilfields for oil analysis (to determine sulfur in petroleum products and residual catalysts, monitor additives in lubricating oils, analyze regular wear metal in lubricants

and analyze wear debris) and for field testing for Lead and heavy metals in soil, etc. Although they have the potential to detect the full spectrum of XRF energies, the analytical performance is optimized by modifying the excitation efficiency so that specific group of elements in particular energy range of the fluorescence spectrum, can be preferentially excited and detected. These modifications include the use of primary beam metal foil filters (which modify the source spectrum reach in the sample to optimize the detection characteristics) and a number of developments in excitation geometry. Furthermore, it is possible to use the selective excitation method i.e., choosing the excitation energy less than the undesired X-rays of the particular element but more than the desired X-ray line energies. This helps to avoid the unnecessary X-ray lines in the spectrum thus simplifying the analysis. Thus, the person working with the analysis of samples by X-ray fluorescence (XRF) technique, has to adopt considerable flexibility of instrumental variables such as excitation voltage, X-ray tubes, collimators, crystals and detectors, pulse height selection but he has no flexibility as regards geometry of the spectrometer.

The PIXE analyst has less flexibility as regards detectors and excitation source but there is flexibility in choice of ion type, beam energy, sample support, and considerable flexibility in changing the geometry of the system. The sample is normally placed in a chamber inside the accelerator vacuum for direct excitation. However, the proton beam may be allowed to pass out of the beam tube through a thin window with negligible energy loss to produce a so-called external beam. (Beam have been extracted into air through Ni-foils, Be-foils, Al-foils, Kapton-foils, and through W-foils). The sample can then be placed directly in the external beam under normal pressure which although having certain disadvantages provided a very useful method for analyzing large, unusually shaped sample for which normal sample preparation techniques are unacceptable. The external beam PIXE method has been employed by Räsänen (1986) for typically thick organic, biomedical, bone and geological samples. The external beam PIXE makes it a very flexible technique for experimentation.

Applications

XRFs has been applied in a wide variety of fields for both qualitative and quantitative analysis e.g., exploration, mining and processing of minerals and materials, forensic and metallurgical fields. Most PIXE applications have been in the analysis of thin samples in which matrix effects are minimal or non-existent e.g., in the fields of biology, mineralogy, medicine, geochemistry, materials science, archaeological, environment, and geology.

Some specific problems undertaken include location of heavy metals in soil specimens due to application of sewage sludge, trace element profiling in electrical insulators, analysis of air particulate collected at urban locations, multilayer thin film analysis of solar cells.

1.15 Conclusion

Both XRF and PIXE techniques are capable of providing accurate and precise data when correctly applied to a suitable type of sample. Because X-rays are more penetrating than protons, the XRF technique samples a greater depth in a thick sample. However, the greater sampling depth requires more extensive corrections for interelement and matrix effects. One of the major problems facing PIXE analysis of thick samples is the extremely small analytical volume. Although PIXE is superior to XRF because the entire range of elements in a sample can be excited by high-energy protons without contributing a high background to the spectrum yet both have limitation of analyzing elements with $Z < 11$ due to Si(Li) detector. WDXRF can, however, be employed for the detection of ^9F . In XRF, the X-ray source must be filtered to remove bremsstrahlung in the region of the spectrum where the analytical X-ray lines occur. Therefore, the use of several excitation conditions is required for the XRF analysis of elements in different ranges of atomic number. Also, the high background found in XRF spectra raises the detection limit. The best obtainable detection limits vary between 10 and 100 ppm for solid samples. The WDXRF, however, is the better technique for the detection of elements with low energy lines, especially in the range 1–4 keV (Na through Ca) and when bulk or thick samples must be analyzed. WDXRF with its superior spectral resolution at medium to low energies can provide information on the chemical state in a sample of a number of elements e.g., Br, Se, As, Cr, S, and Al. PIXE is best applied to the analysis of thin samples when limited amounts of sample are available and/or when the analytic elements are present in very low concentration (less than 1–10 ppm), when analysis of only the surface layers is required and when low detection limits are necessary for elements with atomic numbers close to 40 and 80. Portable EDXRF systems provide the ability to take the spectrometer to the sample, thereby providing a powerful tool for field survey investigations.

<http://www.springer.com/978-3-540-30277-3>

Atomic and Nuclear Analytical Methods

XRF, Mössbauer, XPS, NAA and Ion-Beam Spectroscopic
Techniques

Verma, H.R.

2007, XIV, 376 p. 128 illus., Hardcover

ISBN: 978-3-540-30277-3